UNIVERSITÀ DEGLI STUDI DI BOLOGNA

FACOLTÀ DI SCIENZE MATEMATICHE FISICHE E NATURALI
DOTTORATO DI RICERCA IN FISICA, XVIII CICLO

PhD Thesis

Development and performances of the SFEC card for the TOF apparatus

VERONICA BINDI

Advisor:
Chiar.mo Prof.
FEDERICO PALMONARI

PhD Coordinator:
Chiar.mo Prof.
ROBERTO SOLDATI

Bologna, Italy, March 15, 2006

UNIVERSITÀ DEGLI STUDI DI BOLOGNA

FACOLTÀ DI SCIENZE MATEMATICHE FISICHE E NATURALI
DOTTORATO DI RICERCA IN FISICA, XVIII CICLO

PhD Thesis

Development and performances of the SFEC card for the TOF apparatus

VERONICA BINDI

Advisor:
Chiar.mo Prof.
FEDERICO PALMONARI

PhD Coordinator:
Chiar.mo Prof.
ROBERTO SOLDATI

Key words: Cosmic rays, Charge measurement, Analog and Digital electronics, VHDL code programming

Bologna, Italy, March 15, 2006

Introduction

The Scintillator Front-End Board (SFEC) has been developed with the purpose to improve with the respect to AMS-01, the measure of the charge released by cosmic rays crossing the Time Of Flight (TOF) scintillators of the Alpha Magnetic Spectrometer (AMS-02).

The Alpha Magnetic Spectrometer (AMS-02) is a cosmic rays physics experiment to be installed on the International Space Station (ISS) in 2008 for at least three years of operation. It is a large acceptance super-conducting magnetic spectrometer able to investigate the composition of cosmic rays with high statistics up to the TeV region to provide the most sensitive search for the existence of antimatter nuclei and the indirect evidence of dark matter. It will also measure high energy photons up to a few hundred GeV.

The University of Bologna and the INFN have collaborated to develop the TOF sub-detector of the AMS-02. The TOF system is composed of 4 planes of plastic organic scintillator paddles, two above and two below the magnet. It has the following essential tasks. First of all to generate the fast trigger signal of AMS-02. This signal is also used by the TOF electronics as the common reference time for all the counters. Second task is to measure the velocity $\beta = v/c$ between the upper and the lower TOF of the particles. Third the TOF is able to distinguish between upward and downward going particles with a rejection power in order to separate the $\overline{He}$ signal at level of 10^{-9} from the up going nuclei. Fourth the energy loss measurement is used by the TOF system to generate a special trigger flag for high Z charge events.

This thesis presents the work of my PhD studies. During the first year I deepened my knowledge of the cosmic rays astrophysics. First of all I focused on primary cosmic rays electrons; the results of this work were published in *The Astrophysical Journal*. Then, investigating the power of AMS-02 in the study of the composition of cosmic rays, I engaged to the test beam organized for the TOF scintillators.

In the last two years of my PhD as principal task, I was responsible for the development of the SFEC board and of the Charge Measurement Blocks (CMB) inside all the front-end cards of the TOF. I tested all the prototypes in order to define the flight version of the SFEC and the final version of the CMBs, using the data acquisition system and the laboratory set-up built up for this purpose. Lastly, I performed the tests on the flight model of the SFEC for space qualification.

This thesis is organized as follows. The first chapter presents the features of the cosmic ray flux reaching the Earth, the interstellar abundances of cosmic rays, the propagation models in the galaxy and some experimental results. At the end of this chapter, the AMS-02 detector is presented and its astroparticle physics topics are discussed.

The second chapter reviews the physical processes that describe the passage of the particles through matter, and reviews the scintillation mechanisms. At the end of this chapter the TOF sub-detector of the AMS-02 experiment and the beam test results regarding the charge measurement and resolution are described.

The third chapter presents the front-end electronics used to measure the charge collected by the photomultipliers, when a crossing particle releases part of its energy in the TOF scintillators, focusing on the SFEC board. The final version of the SFEC, installed on the TOF detector, was obtained after several tests on preliminary prototypes.

The forth chapter presents the prototypes used to obtain the flight version of the SFEC, and the DAQ system and the laboratory set-up utilized to test it.

Finally the fifth chapter describes the most significant tests done on the SFEC that were delivered to the flight model, for example: tests on components, test of characterization, of temporization, of dynamic range, and thermal, thermal-vacuum and vibration tests.

Contents

Chapter 1

The cosmic rays abundances in our galaxy

Research in astrophysics of cosmic rays (CRs) provides a fertile ground for studies and discoveries in many areas of particle physics and cosmology. Examples are: the search for dark matter (DM), antimatter, new particles, and exotic physics; studies of the nucleosynthesis, acceleration of nuclei and their transport through the galaxy, CR spectra and composition analysis; the effects of heliospheric modulation [1].

The astrophysics of CRs depend very much on the quality of the data and their proper interpretation. The accuracy of data from current CR experiments on interplanetary spacecrafts, such as Ulysses, Advanced Composition Explorer (ACE), and the two Voyager, specialized balloon-borne experiments such as Super-TIGER, BESS-Polar, CREAM, and the new space-based missions such as Pamela and the Alpha Magnetic Spectrometer (AMS) will improve the accuracy of the current propagation models. This presents a great opportunity for new discoveries.

On the other hand, the whole of our knowledge is based on measurements done only at one point on the outskirts of the Galaxy, the solar system, and on the assumption that particle spectra and composition are (almost) the same at every point of the Galaxy.

This chapter describes: the features of the cosmic rays flux reaching the Earth, the interstellar cosmic rays abundances, the propagations model on the galaxy and some experimental results. The AMS-02 detector and its astroparticle physics are discussed in the conclusion.

1.1 Cosmic rays

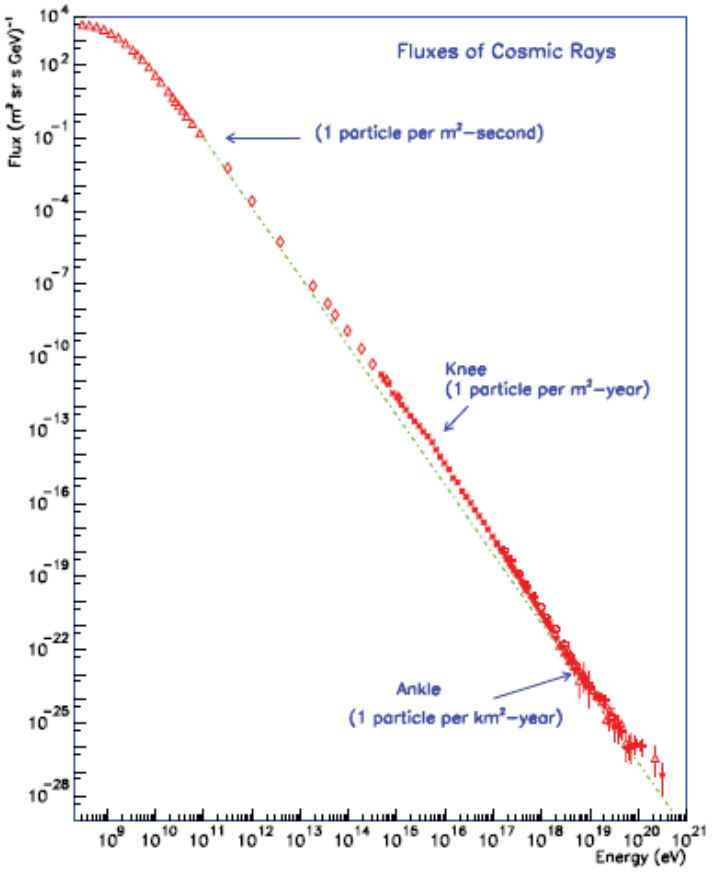

Figure 1.1: All-particle cosmic ray spectrum, adapted from [2] and [3].

CRs are energetic particles which come to earth from outer space and are measured by satellites, balloon-, and ground-based instruments. The energy density of CR particles is about 1 eV cm^{-3} and is comparable to the energy density of an interstellar radiation field (ISRF), magnetic field, and turbulent motions of interstellar gas. This makes CR one of the essential factors determining the dynamics and processes in the ISM. The spectrum of CRs can be approximately described by a single power law with index ~ 3 from 10 GeV to the highest energies ever

observed $\sim 10^{21}$ eV (figure 1.1) [1]:

$$\Phi_i(E < E_0) = \int_0^{E_0} N(E)dE = \int_0^{E_0} k_i E^{-\gamma_i} dE, \tag{1.1}$$

where $\Phi_i(E < E_0)$ is the integral flux of CR particles of species i (usually expressed in particles $m^{-2}sr^{-1}s^{-1}$), γ_i is the spectral index of the power law, and k_i is the normalization constant.

As is better seen in figure 1.2, which shows the differential flux of the most important CRs nuclei through a compilation of several measurements done before 1998, the first evident deviation from a power law is at the low energy corner: here the spectrum flattens and the flux reaches its maximum (some thousand particles per square meter per steradian per second). In fact the flux of particles with lower energies is dumped by the solar wind, and the maximum oscillates following the 11 year solar half-cycles i.e. is influenced by the solar activity. This process is known as *solar modulation*. The Pioneer, the two Voyager, and Ulysses missions contributed significantly to understanding the global aspects of modulation, limiting the number of modulation models free parameters. However the relative importance of various terms in the Parker equation is still not well established. The most widely used are the spherically symmetric force-field and Fisk approximations [1].

The feature confirmed by observations of many groups is a *knee* at $\sim 3 \times 10^{15}$ eV (see figure 1.3), where the spectrum has a smooth shape. The spectral indices are around 2.7 for all nuclei below the spectrum *knee*, when the spectrum abruptly steepens the spectral index becomes equal to 3.

At the highest energies ever detected (few 10^{20} eV) the measured flux is limited by the very low statistics of such rare events: only a total of a few tens of events have been discovered by the various experiments in the last 30 years. Such particles have a curvature radius larger than the Galaxy disk thickness, hence they follow a practically straight line between the acceleration site and the Earth. At present, the measured ultra-high energy cosmic rays (UHECR) incoming direction distribution is nearly uniform (with the exception of an ambiguous possible clustering along the line of sight of the Galaxy center [5], [6]), indicating an extragalactic origin.

The various changes in the spectral index of the CR spectrum reflect the different origins and the propagation histories of CRs with different energy: below the knee their curvature radius is smaller than the galactic disk thickness, hence their sources must belong to our Galaxy, where CRs propagate by diffusion.

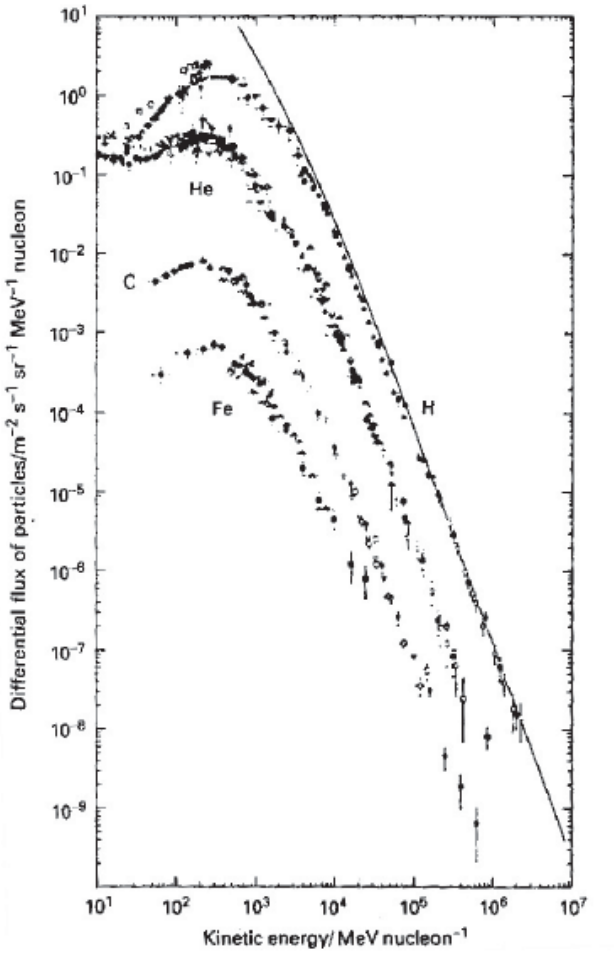

Figure 1.2: Compilation of several experimental measurements of the differential cosmic ray flux of hydrogen, helium, carbon, and iron nuclei [4].

The curvature radius of a particle with charge ze in a uniform magnetic field is:

$$r = \frac{p}{zeB} \approx \frac{10E_{(PeV)}}{zeB_{(\mu G)}}\, pc, \tag{1.2}$$

where $E(PeV)$ is the particle energy in PeV and $B(\mu G)$ is the field intensity in μG. Above the knee, the curvature radius becomes greater than the disk thickness, and CRs may escape into the galactic halo, where the density is very low and the

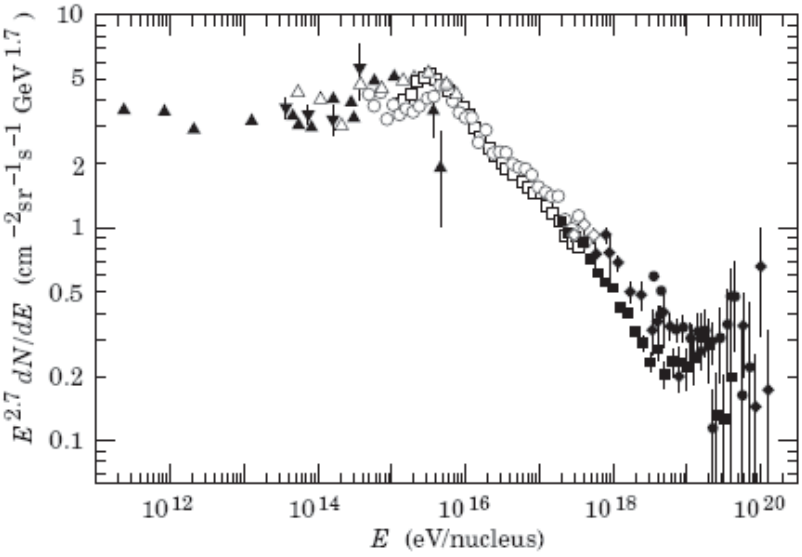

Figure 1.3: All cosmic ray particles energy spectrum [4], multiplied by $E^{2.7}$ in order to better show the spectral index changes.

magnetic field is weaker than in the disk. Only a fraction of the particles that are diffusing through the halo can re-enter the disk, going into a zone with stronger magnetic field. This *leakage* of CR induces an increase of the spectral index because the escape probability is greater for higher energy particles.

The sources of CR are believed to be supernovae (SNe) and supernova remnants (SNRs), pulsars, compact objects in close binary systems, and stellar winds. Observations of X-ray and γ-ray emission from these objects reveal the presence of energetic particles thus testifying to efficient acceleration processes in their neighborhood [1]. Particles have accelerated near the sources propagate tens of millions of years in the ISM before escaping into intergalactic space. During CR propagation, secondary particles and γ-rays are produced, and the initial spectra of CR species and composition change. The destruction of primary nuclei via spallation gives rise to secondary nuclei and isotopes which are rare in nature, antiprotons, and pions ($\pi^{\pm}$, π^{0}) that decay producing secondary $e^{\pm}$s and γ-rays.

The power required to maintain the observed CR energy density $w_{CR} \approx 1$ eV cm^{-3} [7] can be provided by supernova explosions, whose rate in our Galaxy is about $(30y)^{-1}$, if a mechanism with typical efficiency of an order of 10% is found.

The preferred theory is diffusive acceleration applied to the strong shock waves originated by supernova explosions.

This mechanism is based on the repeated crossing of the shock front by the ambient particles of charge *ze*, that on the average gain energy on each encounter with the supersonic wave (the so called *first order Fermi mechanism*), and it is effective up to energies of $z \times 10^{15}$ eV. Hence different species will show different cut-off limits, when their spectra must change slope [3]. Actually, the results from KASKADE [8] show that the knee can be explained as the effect of this cut-off energy for protons and helium, which are the most abundant species in cosmic rays.

During a supernova explosion, the expanding shock wave is able to accelerate charged particles up to the knee range, hence the existence of measurable CR fluxes at higher energies which requires a new kind of engine in our Galaxy. The spectrum above the knee is smoothly connected to the flux below the cut-off energies, and the most natural way to obtain this effect is to imagine that the second acceleration process acts on the particles accelerated by supernovae. This reacceleration mechanism can take place in the vicinity of pulsars [9], where the rapidly rotating magnetic field is a powerful astrophysical dynamo, that is able to accelerate charged particles up to ultra high energies.

At the ankle ($\sim 10^{18}$ eV) even the most heavy elements have energies beyond the supernovae (and may be also the pulsar) acceleration limit, hence a new component is required to explain the observed flux [3]. In addition, above the ankle the cosmic ray energy is so big that their trajectory is not bent very much even by the disk interstellar magnetic field, and can be considered a straight line. Because of the quite uniform distribution of the incident directions over the whole sky, it is probable that such particles have originated outside our Galaxy.

In the following paragraph, we will focus on charged cosmic rays in the energy range above few hundred MeV and below few TeV, that are the target of the AMS experiment. Such particles originate from galactic sources and their spectra gives us information about the sources, the interstellar medium, the galactic magnetic field, and the heliosphere. Thus, the study of the cosmic ray flux of protons, electrons, helium and all other nuclei, when combined with information about their reaction cross sections, energy loss and interactions with magnetic fields, is a fundamental probe for the knowledge of our Galaxy.

1.2 Interstellar abundances of cosmic rays

The relative abundances of the different elements are related to the composition at the source and the propagation history of cosmic rays. The isotopic spectra of few elements are especially important because they are of pure secondary origin (like B, for example) or radioactive (like ^{10}Be and ^{26}Al), thus allowing for an estimation of the matter thickness traversed by CRs and of the propagation time between sources and detection. Electrons (and positrons) have very rapid energy losses through electromagnetic processes, while heavy particles mainly degrade their energy by ionizing the interstellar medium. Hence e^- and e^+ diffuse in smaller volumes than ions and their measured spectra are mostly determined by the most recent and nearest supernovae. Positrons are thought to be produced during the CRs propagation in the ISM. For this reason they are also very useful for the tuning of the parameters of propagation models. Protons and antiprotons, and electrons and positrons, are also important for two reasons. First, particles and antiparticles are practically equivalent for propagation models, they differ only by the sign of the electric charge. This difference can be used to study the charge-dependent effects of the solar modulation. Second, the antiparticle spectra may show distinctive features that could be interpreted as signatures of the annihilation of the exotic particles that constitute the dark matter in our Galaxy (as in the rest of the universe) [1].

Primordial nucleosynthesis produced the protons and the bulk of the helium nuclei, but only a negligible part of heavier elements (^7Li is the only detectable fraction) [10]. The rest of the baryonic matter was (and is being) produced by stellar nucleosynthesis (up to Fe) and SN explosions.

1.2.1 Model of cosmic ray propagation

The relative abundances of the different species of cosmic rays give us important information on the propagation details and on the source composition. The analytical methods include the so-called leaky-box model and diffusion models (e.g., disk-halo diffusion model, the dynamical halo wind model, the turbulent diffusion model, reacceleration model) [1]. The leaky-box model treats a galaxy as a box with reflecting boundaries and a little leakage, so that a particle travels across it many times before escaping. In this model the principal parameter is an effective escape length and particles, gas, and sources are distributed homogeneously. The leaky-box model has no predictive power and can be incorrect in cases when the

distribution of gas or/and radiation field is important, such as: radioactive isotopes, diffused Galactic γ-rays, electrons, or/and positrons (because of their large energy losses) etc. It also can not account for the spatial variations of CR intensity. Diffusion models [1] are more realistic, distinguishing between the thin Galactic disk and extensive halo, often with different diffusion coefficients. The alternative solution is the direct numerical solution of the diffusion transport equations for the entire Galaxy and for all CR species.

The model of CR diffusion in the Galaxy includes the solution of the transport equation with a given source distribution and boundary conditions for all CR species. The transport equation describes diffusion and energy losses and may also include the convection by a hypothetical Galactic wind, distributed acceleration in the ISM due to the Fermi second-order mechanism, and non-linear wave-particle interactions (for more details see [1]). The boundary conditions assume free particle escape into intergalactic space.

The study of stable secondary nuclei (Li, Be, B, Sc, Ti, V) allows one to determine the ratio (halo size)/(diffusion coefficient) and the incorporation of radioactive secondaries ($^{10}_{4}Be$, $^{26}_{13}Al$, $^{36}_{17}Cl$, $^{54}_{25}Mn$) and is used to find the diffusion coefficient and the halo size [1]. The derived source abundances of CR may provide some clues to the mechanisms and sites of CR acceleration. However, the interpretation of CR data, for example, the sharp peak in the secondary/ primary nuclei ratio (e.g., B/C), depends on the adapted physical model. The leaky-box model fits the secondary/primary ratio by allowing the path-length distribution vs. rigidity to vary. The diffusion models are more physical and explain the shape of the secondary/primary ratio in terms of diffusive reacceleration in the ISM, convection by the Galactic wind, or by the damping of the interstellar turbulence by CR on a small scale.

The study of transport of the CR nuclear component requires the inclusion of nuclear spallation, radioactive decay, and ionization energy losses. The calculation of isotopic abundances involves hundreds of stable and radioactive isotopes produced in the course of CR interactions with interstellar gas. A thorough data base of isotopic production and fragmentation cross sections and particle data is thus a critical element in models of particle propagation that are constrained by the abundant measurements of isotopes, antiprotons, and positrons in CR.

Increasingly accurate balloon-borne and spacecraft experiments justify the development of sophisticated and detailed propagation models with improved predictive capability.

Modern computer codes, incorporating recent developments in astrophysics

and nuclear physics, exist. One example is GALPROP[1] [1], a numerical model and a computer code (written in C++) of CR propagation in the Galaxy; this is the most advanced 3-dimensional model to date. The model is designed to perform CR propagation calculations for nuclei (H to Ni), antiprotons, electrons, positrons, and computes γ-rays and synchrotron emission in the same framework; it includes all relevant processes and reactions. The GALPROP model has been proven to be a useful and powerful tool to study CR propagation and related phenomena. Its results (and the code) are widely used as a basis for many studies, such as the search for: DM signatures, origin of the elements, the spectrum and origin of Galactic and extragalactic diffuse γ-ray emission, heliospheric modulation etc.

1.3 Measurement of CR ions spectra

Direct measurements of the cosmic ray spectra in the solar system have been done by balloon and satellite experiments. The most important are HEAO-3 [11], ACE [12], Voyager 1 and 2 [13] and Ulysses [14]. These measurements can be used to constrain the parameter space of propagation models, as it was done by several groups. Recently, [15] and independently Moskalenko et al. [16] emphasized that, in order to have a good fit at the same time for the B/C and sub-Fe/Fe ratios, it is necessary to consider the effect of the local bubble (LB) where the Sun is collocated.

In particular, the study of the radioactive nuclei (the most important are ^{10}Be, ^{14}C, ^{26}Al, ^{36}Cl, ^{60}Fe) shows that in first approximation the Sun is within a shell of radius ~ 50 pc with density $\sim 0.1\ cm^{-3}$, surrounded by a shell with almost null density extending up to radii ~ 200 pc. Beyond this second shell, the average density is $1 cm^{-3}$ [15].

This is consistent with the picture of the local interstellar medium consisting of an asymmetric bubble with radius of 65-250 pc filled by hot ($T \sim 10^5 - 10^6$ K) and low-density ($n \leq 0.005 cm^{-3}$) gas, surrounded by a dense neutral gas boundary (*hydrogen wall*), as derived from spectroscopic measurements [17, 18, 15, 19, 20, 21]. The presence of this low density zone around the solar system does not affect the diffusion of stable ions, but the secondary nuclei abundances, produced by spallation, which are perturbed. For radioactive species the effect is very important, because they sample relatively small fraction of volume in which stable nuclei propagate: the effect is well represented by an exponential attenuation

[1] http://lheawww.gsfc.nasa.gov/users/imos/galprop.html

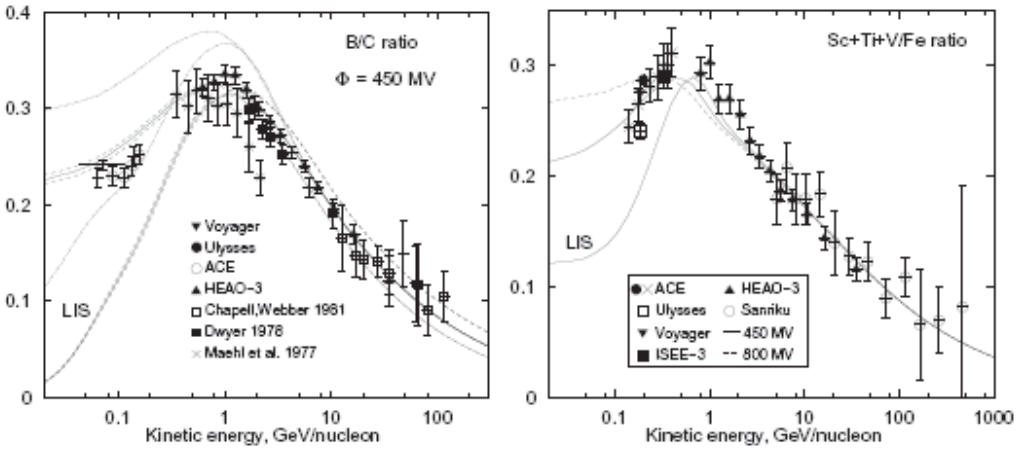

Figure 1.4: Boron to carbon (left panel) and sub-Fe to iron (right panel) ratios: measurement can be at at the same time by a diffusive propagation model that takes into account CR reacceleration and convection, and a *fresh* contribution of C and O nuclei in the local bubble. The computed local interstellar spectrum is shown for comparison. Details about different parameters can be found in Moskalenko et al. [16].

$\exp(-r_{hole}/l_{rad})$, where r_{hole} is the radius of the underdense region around the Sun, and $l_{rad} = \sqrt{K(E)\gamma\tau_0}$ is the radial distance from the source that a particle that is following a random walk reaches on the average. $K(E)$ is the diffusion coefficient and γ is the Lorenz factor of the nucleus with lifetime τ_0 at rest [15].

Values $60pc \leq rhole \leq 80pc$ are suggested by $^{10}Be/^{9}Be$ and $^{36}Cl/Cl$ ratios which are measured by ACE, while the $^{26}Al/^{27}Al$ ratio seems not to be compatible. By enlarging the r_{hole} range to 100 pc it is possible to fit in at minimum the Ulysses and Voyager $^{26}Al/^{27}Al$ data [15].

The need for a local structure is motivated by Moskalenko et al. [16] in a different way. They pointed out the fact that the conventional propagation models fail to reproduce simultaneously B/C and sub-Fe/Fe ratios, and the antiproton flux, even in presence of re-acceleration. However, their numerical simulation (GALPROP) can be consistent with the data if one includes a *"fresh unprocessed"* component at low energy, perhaps associated with the Local Bubble (LB)(figures 1.4 and 1.5). The presence of ^{12}C and ^{16}O component would lower the local B/C ratio, because B is produced by spallation, that is not an important effect in the

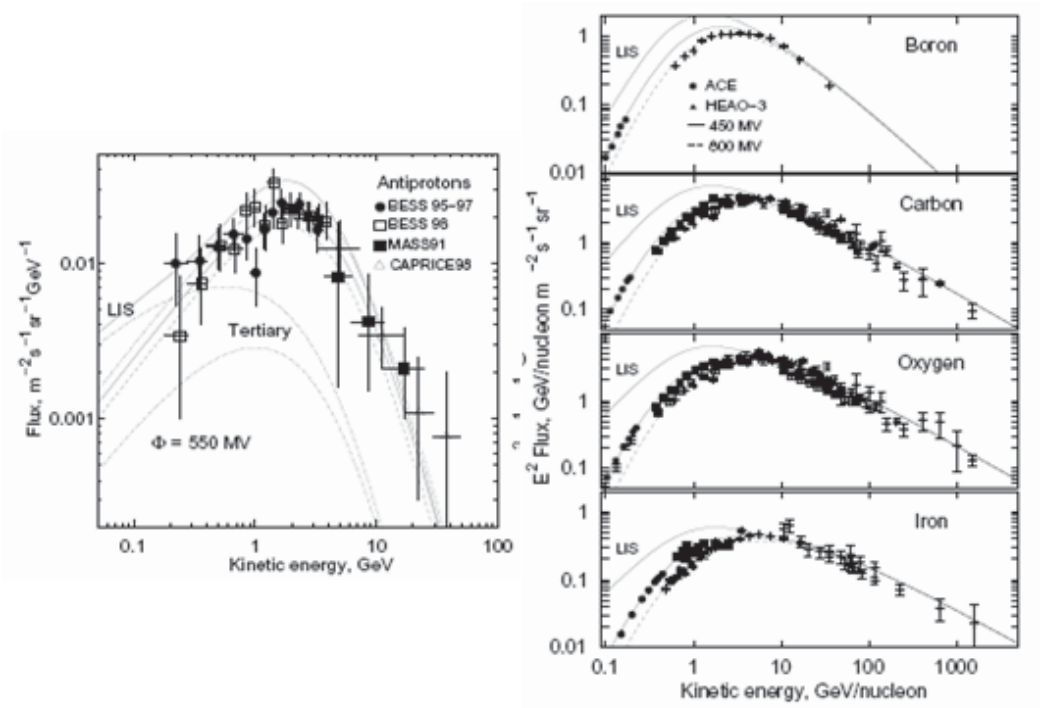

Figure 1.5: Cosmic ray antiproton (left panel) and ions spectra (right panel) measured by different experiments are compatible with a diffusion/reacceleration propagation model with contribution from the local bubble [16]. The measured spectra are sensibly different from the local interstellar spectra below 10 GeV per nucleon.

neighborhood of the Sun.

This is consistent with the idea that the local bubble [18] was probably produced in a series of supernova explosions whose progenitor was an O-B star association[2]. The LB age is $\sim$ 10 My and it was produced by 10-20 SN explosions, with the last SN 1-2 My ago or 3 SN in the last 5 My [18]. There is also evidence in favor of a nearby recent SN (at about 30 pc from the Sun) [16]. Thus it is very probable that particles coming directly from SN remnants still influence the local

[2]An O-B association is a large, very loose form of an open star cluster consisting of young spectral type *O* and *B* stars. They cover large volumes of space, are loosely held together by gravity and have short lifetimes (a few million years) as a distinct object.

spectra and abundances of cosmic rays.

In conclusion Strong and Moskalenko demonstrated that, by combining the measurements of the antiproton flux and B/C ratio to fix the diffusion coefficient, one is able to construct a model consistent with measurements of important nuclei ratios in CR and derive elemental abundances in the LB. Calculated distribution of isotopic abundances of Be and B are in perfect agreement with CR data. The abundances of three radioactive isotopes in CR, which are often used as "radioactive clocks" to determine the Galactic halo size, ^{10}Be, ^{26}Al, ^{36}Cl are all consistent and indicate a halo size $z \sim 4$ kpc based on the most accurate data by ACE spacecraft, even if the ^{54}Mn indicated a smaller halo, but this may be related to its half-life uncertainty and/or cross section errors. The derived fraction of the LB component in CR seems to be small compared to Galactic CR and has a steep spectrum with a cutoff above several hundred MeV/nucleon. All of this consideration may be confirmed by new experimental measurements that will impose better precision.

1.4 Cosmic ray electrons

Cosmic ray electrons are probably accelerated by the same engines that accelerate CR protons and nuclei (supernova explosions), but they differ significantly from hadrons because of the energy lost during the propagation through the interstellar medium [22].

Because of their small mass and lack of strong interactions, electrons suffer large energy losses due to electromagnetic processes such as synchrotron radiation, inverse Compton scattering, and bremsstrahlung. These losses effectively limit the volume that can be pervaded by the electrons that were emitted by a given source: the measured spectrum must carry information on smaller scales than the stable elements.

Even though there are conceivable sources of primary positrons, like pulsars, primordial black holes or super-symmetric particles annihilation, the measured fluxes are compatible with the simple hypothesis of complete secondary origin. In fact, the secondary production of e^+ and e^- by pion decay (the pions are produced in the CR proton interactions with the interstellar medium) yields almost the same amount of electrons and positrons, whereas the measured fraction e^+/e^- is about 10%. Thus electrons are mostly of primary origin, while the positrons have secondary origin and can be used to set constraints on the parameters of CR propagation.

1.4.1 Energy losses

Bremsstrahlung is significant when electrons propagate through H_{II} regions (radio emission) or near X binaries (X-rays). The emission power due to bremsstrahlung is proportional to the product of the ion and electron densities of the plasma, and to the square of the average ion charge:

$$-\left(\frac{dE}{dt}\right)_{brem} = 4N_e N_{ion} Z(Z+1.3) r_e \alpha c \bar{g} E \tag{1.3}$$

where r_e is the classical electron radius, $\bar{g}$ is the Gaunt factor, and $E = mc^2$ is the total energy. In the cases of interest:

$$-\left(\frac{dE}{dt}\right)_{brem} = \gamma ln\gamma \tag{1.4}$$

for fully ionized H, and

$$-\left(\frac{dE}{dt}\right)_{brem} = \gamma \tag{1.5}$$

for neutral H. If the electrons have a power law distribution in momentum with spectral index $-\eta$, the bremsstrahlung radiation has a power law spectrum with the same spectral index $-\eta$ [7].

Synchrotron radiation is the dominant process when CR electrons propagate through regions where a magnetic field of intensity H exists, the emission power being proportional to $U_{mag} \propto H^2$:

$$-\left(\frac{dE}{dt}\right)_{sync} = \frac{4}{3}\sigma_T c U_{mag} \gamma^2 \tag{1.6}$$

where $\sigma_T = r_e^2 8\pi/3$ is the Thomson cross-section ($r_e = e^2/(4\pi\varepsilon_0 m_e c^2) = 2:818 \times 10^{-15}$ m is the classical electron radius) and U_{mag} is the magnetic field energy density. For an electron power law distribution in momentum with spectral index $-\eta$, the synchrotron radiation has a spectrum that depends on the average magnetic field intensity and a spectral index equal to $-(\eta-1)/2$ (same of synchrotron) [7].

Inverse Compton scattering is the dominant process in photon rich environments, like the jets emitted by active galactic nuclei, and in the case of low matter density, when the electrons have to interact with at least the cosmic microwave background photons. If the energy density of the photon field is U_{rad}:

$$-\left(\frac{dE}{dt}\right)_{i.C.} = \frac{4}{3}\sigma_T c U_{rad} \gamma^2 \tag{1.7}$$

DIRECT MEASUREMENTS OF COSMIC RAY ELECTRONS AND POSITRONS

MEASUREMENT	YEAR	ϕ (MV)	SUN POLARITY	e^-/e^+ SEPARATION	E_{min} (GeV)	E_{max} (GeV)	REFERENCES e^-	e^+	p^+	NOTES
Fanselow et al. (1969)	1965, 1966	570(50)	−	Y	0.07	11.0	1	1	...	a
Nishimura et al. (1980)	1968–1975	700(200)	−, +	N	30.0	1500	2	...	...	a
Meegan & Earl (1975)	1969, 1973	650(100)	+	N	6.4	114	3	...	...	a
Buffington et al. (1975)	1972, 1973	650(50)	+	Y	5.1	63.0	4	4	...	a
Prince (1979)	1975	550(50)	+	N	10.2	202	5	...	...	a
Golden et al. (1984, 1987)	1976	500(50)	+	Y	3.45	91.7	6	7	...	a
Tang (1984)	1980	900(200)	+	N	4.89	200	8	...	...	a
MASS 89	1989	1400(50)	−	Y	1.6	16.1	9	9	10	b
MASS 91	1991	2000(200)	+	Y	7.5	46.9	11	11	12	b
CAPRICE 94	1994	664(5)	+	Y	0.54	34.3	13	13	14	b
HEAT 94	1994	650(50)	+	Y	5.45	66.4	15	15	...	c
HEAT 95	1995	550(50)	+	Y	1.20	66.4	15	15	...	a
Nishimura et al. (2001)	1996, 1998	600(100)	+	N	30.0	3000	16	...	...	a, c
BETS 97+98	1997, 1998	600(100)	+	N	13.9	112.6	17	...	...	a, c
AMS 98	1998	632(13)	+	Y	0.15	35.7	18	18	19	b

NOTES.—The value of the solar modulation parameter ϕ was estimated using: (a) neutron rates; (b) the proton spectrum measured by the same detector; and (c) the proton spectrum measured by a different detector in the same period. Positive and negative solar polarities refer to epochs when the magnetic field emerging from the north pole of the Sun points outward and inward, respectively (Bieber et al. 1999). The energy range is reported for electrons only.

REFERENCES.—(1) Fanselow et al. 1969; (2) Nishimura et al. 1980; (3) Meegan & Earl 1975; (4) Buffington et al. 1975; (5) Prince 1979; (6) Golden et al. 1984; (7) Golden et al. 1987; (8) Tang 1984; (9) Golden et al. 1994; (10) Webber et al. 1991; (11) Grimani et al. 2002; (12) Bellotti et al. 1999; (13) Boezio et al. 2000; (14) Boezio et al. 1999; (15) Du Vernois et al. 2001; (16) Nishimura et al. 2001; (17) Torii et al. 2001; (18) Alcaraz et al. 2000a; (19) Alcaraz et al. 2000b.

Table 1.1: Cosmic ray electrons measurements ([25] and references therein).

A power law spectrum with spectral index $-\eta$ for the electrons produces a power spectrum in frequency due to inverse Compton scattering with spectral index equal to $-(\eta-1)/2$ [7].

In conclusion, electrons suffer a total energy loss

$$-\left(\frac{dE}{dt}\right)_{tot} = aE^2 + bE + clnE \tag{1.8}$$

while electromagnetic losses different by ionization, are usually not important for CR protons and nuclei. In leaky box jargon, this can be translated into the effective lifetime $\tau_{loss} \approx 300$ (E/1 GeV)$^{-1}$ My. This corresponds to a mean diffusive radial distance $r_{loss} \approx 1$ kpc (E/1 GeV)$^{-1/2}$ $(K/0.03 kpc^2 My^{-1})^{1/2}$ from the source [23].

Hence the measured CR electron spectrum gives information only about a rather small volume of Space around the Solar System. For example, electrons with $E > 10$ GeV are thought to be very sensitive to the local bubble, while protons are travelling throughout a large part of the galactic disc (up to the Galaxy core [24]) and halo.

On the other hand, electrons can be mapped through the Galaxy thanks to their electromagnetic emission, and their interstellar density can be inferred from the measurements of the synchrotron emission in the radio band. In this way we can infer the average electron density in our and in other galaxies.

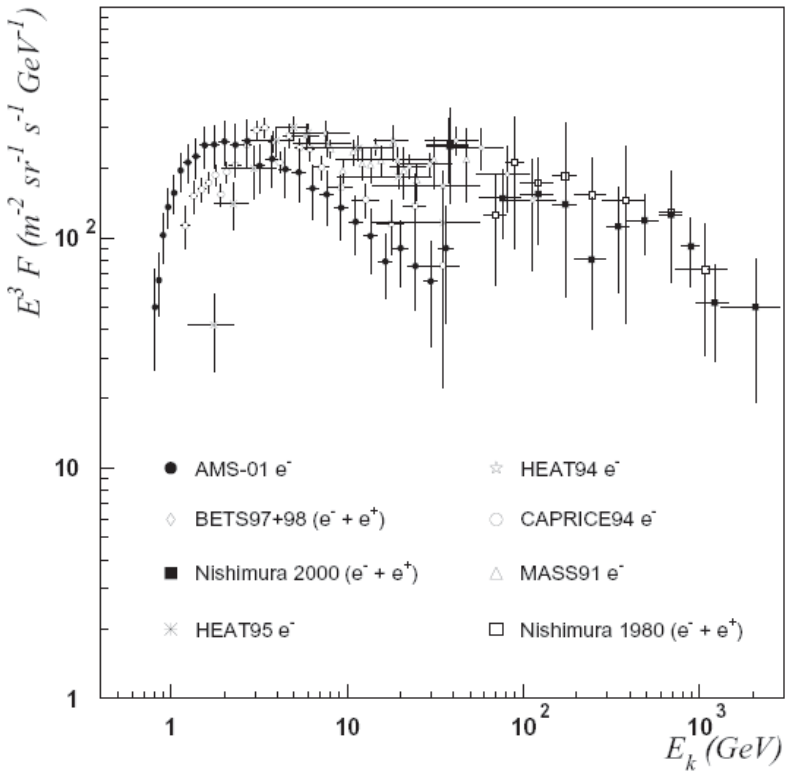

Figure 1.6: Local interstellar spectrum of cosmic ray electrons measured by recent experiments between about 1 GeV and 2 TeV [25].

Figure 1.6 shows the inferred local interstellar spectrum (LIS) of the cosmic ray electrons, obtained by demodulating the spectra measured by recent experiments [25] (table 1.1). The spread of the data points could be due to systematic uncertainties arising from correction of the residual atmosphere or of the detector response. If these effects are not strongly energy dependent, it is possible to renormalize the spectra to the same value at fixed energy, in order to minimize the spread.

Figure 1.7 shows that it is possible to fit the renormalized data set with a single power law in kinetic energy, obtaining a spectral index of 3.4 between 3 GeV and 2 TeV. Whereas several authors (see for example [26]) emphasize the idea that the electron LIS should have slope changes due to the interplay between propagation

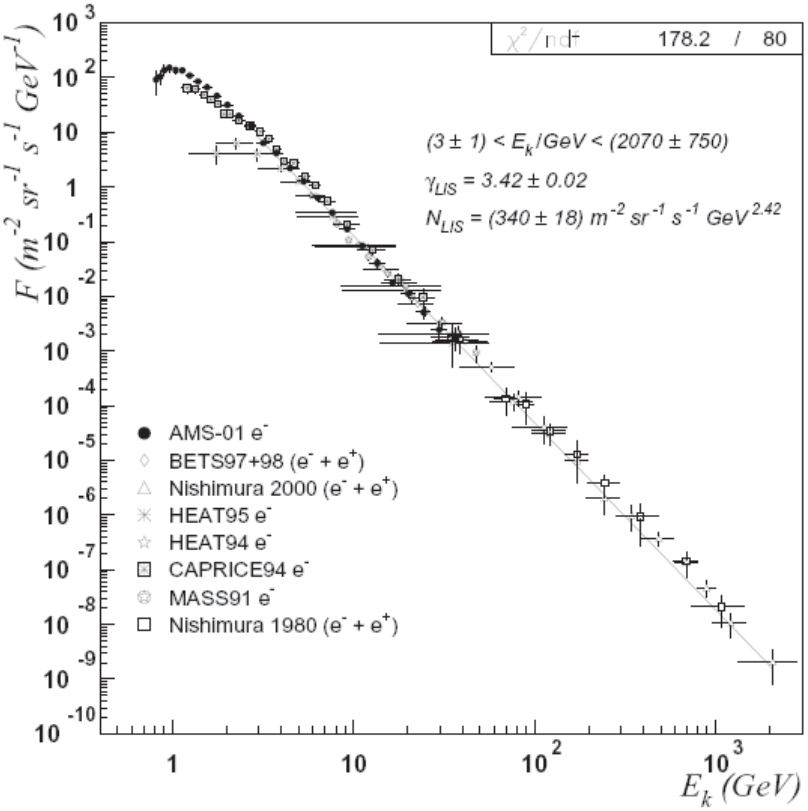

Figure 1.7: Local interstellar spectrum of cosmic ray electrons. Data taken by different experiments were renormalized to the AMS-01 flux at 20 GeV, with the exception of CAPRICE94 [25].

by diffusion, energy losses and source distribution. Figure 1.7 shows that the overall data set does not strongly suggest any spectral index change.

In addition, the overall LIS has the same slope as the electron LIS inferred from AMS-01 alone, that extends down to 1.5 GeV. Also the low energy flattening of different experiments may be explained by a charge dependent on solar modulation effect [25]. Thus, the spectral change at 10 GeV foreseen by Moskalenko and Strong [27] is not compatible with the inferred electron LIS obtained by the most recent experiments. Instead, the electron LIS may suggest that the measured cosmic ray spectra are due to a recent and nearby supernova (or perhaps a few SNe), whose remnants may even be contained the Solar System. This would also

affect the spectra of the CR ions, that would have a galactic and a local component. Future high statistics measurements of the ions spectra made by AMS-02 and other experiments should be able to determine the relative importance of the two components.

1.5 Summary and future outlook

During the next five years our knowledge of the flux and charged composition of CR in the GeV to TeV energy range will be greatly improved thanks to the deployment of space borne spectrometers: PAMELA [28, 29] on a Russian rocket from 2006 to 2009 and AMS-02 on the International Space Station (ISS) from 2008 to 2011 [30]. AMS-02 will increase the statistical samples of charged CRs by several orders of magnitude by extending these high precision measurements well up to the TeV region, which is interesting for various topics of physics.

Polar BESS [31] long duration flights, thanks to BESS large acceptance, will have a good sensitivity to the lower energy part of the CR spectrum and will perform a precise measurement of low energy $\overline{p}$. On the other hand, the space borne PAMELA spectrometer, in spite of its small aperture, will have a chance to perform high statistic CR measurements, while for energies above O(1 GV) AMS-02 will be the best performing experiment.

1.5.1 AMS-02

AMS-02 is a high energy particle physics experiment to be installed on the ISS in 2008 for at least three years of operation. It is a large acceptance ($\sim 0.5\ m^2 sr$) super-conducting magnetic spectrometer, able to investigate the composition of cosmic rays with high statistics up to the TeV region [32].

A *"scaled-down"* version, AMS-01, was built and successfully flown on the shuttle Discovery (STS-91) for 10 days in June 1998 at a mean altitude of 370 km. The heart of the AMS-01 detector was a magnetic spectrometer, using a 0.15 T permanent dipole magnet and a partially equipped six plane silicon tracking detector. The set-up was completed by a two double layer scintillator time-of-flight system, an aerogel threshold Cherenkov counter and veto counters located on the magnet inner wall. The detector thus measured the charge Z, rigidity $R = pc/|Z|e$, velocity β and specific energy loss dE/dx of particles traversing its aperture. The main goal of the STS-91 10 day flight in June 1998 was to test the AMS-01 equip-

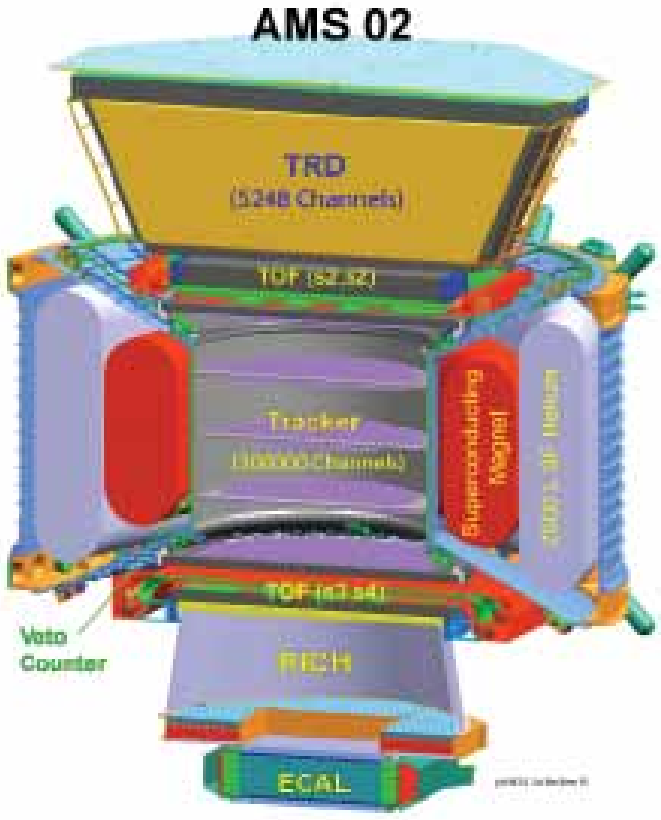

Figure 1.8: Full view of the AMS Spectrometer.

ment under stringent conditions during the launch and in the space environment, and to familiarize the AMS-01 team with operations in space. AMS-01 had control of the shuttle orientation for ninety hours. Data was taken at a variety of altitudes, between 320 and 390 km above sea level. The space shuttles orbit covered latitudes between $\pm 51.7^{\circ}$ and all longitudes. A total of 10^8 events were registered [33, 34, 35, 36, 37, 38].

Due to the environmental conditions in space, AMS-02 had to fulfill various special requirements concerning weight (limited to 7 tons), thermal vacuum, vibration, cosmic radiation, electromagnetic interference, power consumption (limited to 3kW) and data communication.

Following the experience gathered during the AMS-01 mission, a more am-

bitious detector with extended rigidity range from a few GV to the TV region was designed for installation on the ISS. This detector, AMS-02, is based on a spectrometer with a super-conducting magnet. Its main components are shown in figure 1.8.

The superconducting magnet [39] consists of two Helmholtz coils and two series of six smaller racetrack coils circumferentially distributed, cooled by superfluid helium at 1.8 K. This configuration was chosen for three reasons: to increase the overall dipole field, to reduce the stray field and to suppress the torque resulting from the interaction of the magnet's magnetic moment with the Earth's magnetic field. Close to the center, the magnetic field reaches 0.8 T which is six times the field strength of the AMS-01 permanent magnet. It is thermally connected to a 2500 l vessel of liquid helium for about 3 years of operation without refill.

Trajectories of charged particles are localized by double sided silicon sensors [40], arranged in eight layers of about one squared meter each on five planes of an ultra-light support structure. Close to 2500 sensors provide a tracking resolution of $\sim 10\ \mu m$ in the bending direction and $\sim 30\ \mu m$ orthogonal to it. Together with the improved magnet ($BL^2 = 0.9\ Tm^2$), particle rigidity is measured with an accuracy of better than 2% up to 20 GV and the maximal detectable rigidity is around 1 TV. The measurement of specific energy loss, $dE/dx \sim |Z^2|$, in the silicon serves to identify nuclei. The tracker also measures the direction and energy of photons, interacting the material above the first tracker layer, with excellent directional resolution and good energy resolution [40].

Separation between light and heavy particles is provided by the Transition Radiation Detector (TRD) [41] on top of the set-up, which measures the radiation emitted by particle upon changes in the index of refraction of the traversed medium. The detector features 20 layers of a fleece radiator and proportional straw tubes with a Xe/CO_2 gas mixture for X-ray detection. Since the intensity of emitted transition radiation (TR) is proportional to the Lorentz factor γ, light particles such as positrons have a much higher probability of emitting TR than heavy particles such as protons. Therefore the TRD will separate hadrons from electrons in the range 10 to 300 GeV. It will also help in the tracking of charged particles, identify photon conversion points and measure dE/dx.

As in AMS-01, two crossed double layers of scintillators placed at the magnet end-caps provide time-of-flight (TOF) [42] and thus measure particle velocity. Due to the higher magnetic stray field of the AMS-02 superconducting magnet, the phototubes have to be aligned carefully with the local magnetic field. A timing

resolution for protons of ~ 180 ps is nevertheless expected and 100 ps for light ions. In addition to measuring the velocity of particles and their direction, the time-of-flight system provides a redundant measurement of dE/dx with about a 10% resolution for minimum ionizing particles. It is also the principal trigger detector for charged particles.

Below the spectrometer, a Ring Imaging Cherenkov detector (RICH) [43] provides further velocity and charge measurements. Light emitted in the combined aerogel ($n = 1.05$) and sodium-fluoride ($n = 1.334$) radiators is detected as an elliptical pattern of photons by an array of position sensitive photo multipliers on the bottom. The emission angle measures velocity, with an expected resolution of $\delta\beta/\beta \simeq 10^{-3}$. The number of photo-electrons measures the charge with a resolution better than 20% for low Z ions, thus providing an independent measurement of the charge, up to the iron.

At the very bottom, an Electromagnetic Calorimeter (ECAL) [44] made of 640 kg of lead scintillating fiber sandwich completes the set-up. The calorimeter reconstructs the shower with a three dimensional sampling using crossed layers. Its energy resolution is expected to be $\delta E/E \simeq 10.1\%/\sqrt{E(GeV)} \oplus 2.6\%$ for electromagnetic showers. It distinguishes hadronic from electromagnetic showers by their lateral and longitudinal shape, thus suppressing protons by a factor of 10^{-4} up to several hundred GeV. The calorimeter will also serve as an independent photon detector, with an angular resolution of about $\sim 1^{\circ}$.

Particle identification on AMS-02 relies on a very precise determination of the magnetic rigidity, energy, velocity and electric charge. Velocity of low energy particles (up to ~ 1.5 GeV) is measured by the TOF detector while for kinetic energy, above the radiator thresholds, the RICH will provide very accurate measurements; a target resolution of 1% and $\sim 0.1\%$ for single charged particles is expected, respectively for sodium fluoride and aerogel radiators. The absolute value of the electric charge is measured by the silicon tracker and the TOF detectors through dE/dx sampling and by the RICH through Cherenkov signal integration. Ion identification at least up to iron is expected. The new detector thus features sophisticated particle identification devices that will allow to discriminate the small amount of antiprotons and other antinuclei against the large background of electrons, as well as positrons against the overwhelming background of protons, up to high energies. It will also have two ways of measuring high energy photons, by conversion in the tracker and in the electromagnetic calorimeter, which will allow systematic long term observations of the gamma ray sky.

Figure 1.9 shows the different signals produced by the AMS-02 sub-detector

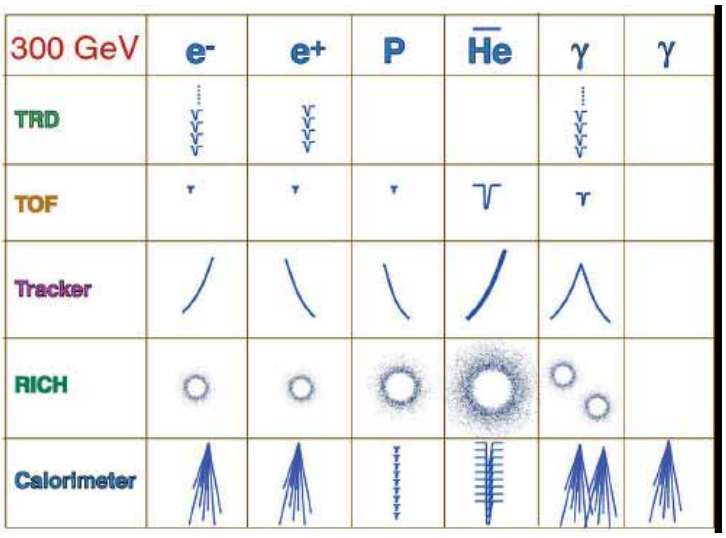

Figure 1.9: The different signals produced by the AMS-02 sub-detector when a crossing particle released part of its energy on the AMS-02 apparatus.

when a crossing particle released part of its energy on the AMS-02 apparatus.

1.5.2 Astroparticle physics with AMS-02

Charged Cosmic ray component

Since the 1998 measurement of AMS-01 [33] and the data published by BESS in 2000 [45] the flux of the main CR component, the protons, is known with 5-10% accuracy up to 200 GeV, and with 10-30% accuracy up to 100 TeV [46]. Helium flux is known with 10% accuracy up to 10 GeV but above this energy the measurements are rather poor. Light $Z > 2$ nuclei have been measured with about 5% accuracy only up to 35 GeV [47, 48, 11]. It would be important to extend with AMS-02 the energy range for precise measurements of hadrons up to the TeV region because they are the source of the atmospheric neutrinos used for the determination of the neutrino mass in underground experiments.

For the study of CR composition, precise measurements of some stable isotopes such as deuterium, boron and carbon or long-lived isotopes such as ^9Be are particularly important to understand the propagation and trapping mechanisms of CR in our galaxy (see figure 1.10). Accurate measurements of D are now avail-

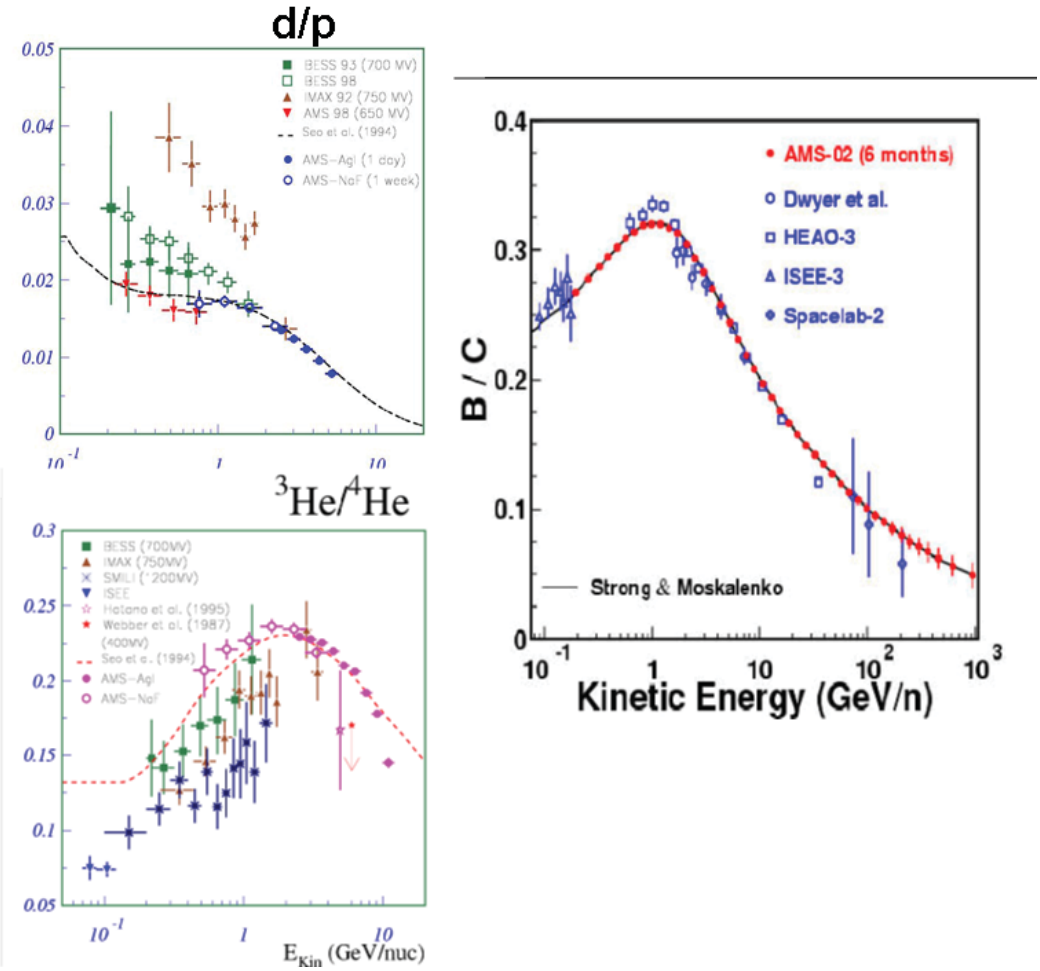

Figure 1.10: d/p, 3He/4He, B/C give information on cosmic ray propagation, AMS-02 like shown from the Monte Carlo simulations, will extend the energy range [1].

able only up to a few GV of rigidity while the knowledge of the ratio $^{9}Be/^{10}Be$ important for the confinement times and the galactic halo models, is very poorly known above about hundred MV of rigidity. AMS-02 like shown from the Monte Carlo simulation will extend the energy range (see figure 1.11).

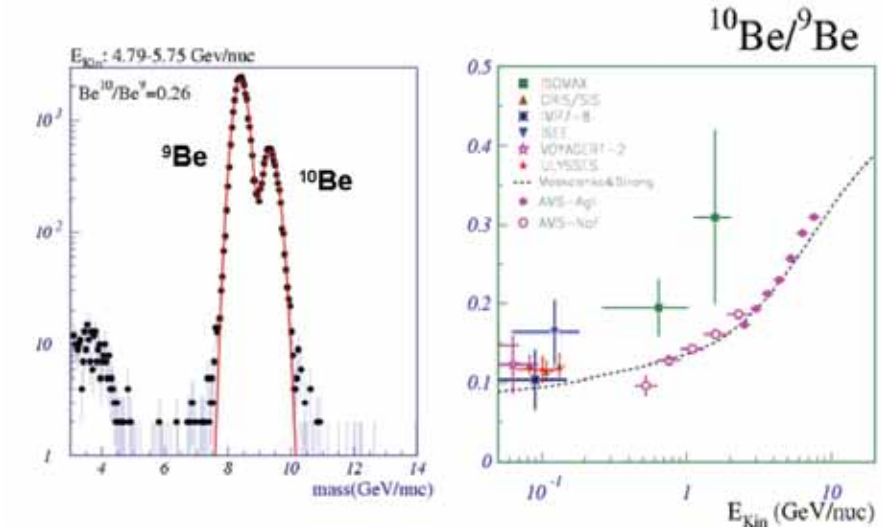

Figure 1.11: $^9Be/^{10}Be$ is important for the confinement times and the galactic halo models, AMS-02 can distinguish between the two isotopes and, like shown from the Monte Carlo simulation, will extend the energy range up to 10 GeV/nuc [1].

Antiprotons

Antiprotons are a rare but interesting hadronic component of high energy CR, because they could be produced by exotic sources such as antimatter dominated regions or by the decay or annihilation of new particles. Their flux ratio to protons is at the level of $O(10^{-4})$ with kinetic energies of around 1 GeV. This rate is in agreement with the expectation that $\overline{p}$ are produced in high energy CR interactions with the interstellar medium. However, in more than 40 years of experiments with balloons, only a few thousand $\overline{p}$ have been measured, mostly with energies below 10 GeV (see figure 1.12). Statistical errors are then quite large, in particular below 1 GeV and above 10 GeV. In addition systematic errors due to uncertainties in the modeling of the propagation in the interstellar-medium or of the solar-modulation are still at the level of 20/30%. The figure also shows a full Monte Carlo simulation of the expected AMS-02 accuracy on $\overline{p}$ spectrum after three years on the ISS, starting from a spectrum with a power law between 2.5 and 2.6 in the kinetic energy range $100 \div 400$ GeV and a 900 MV solar modulation parameter.

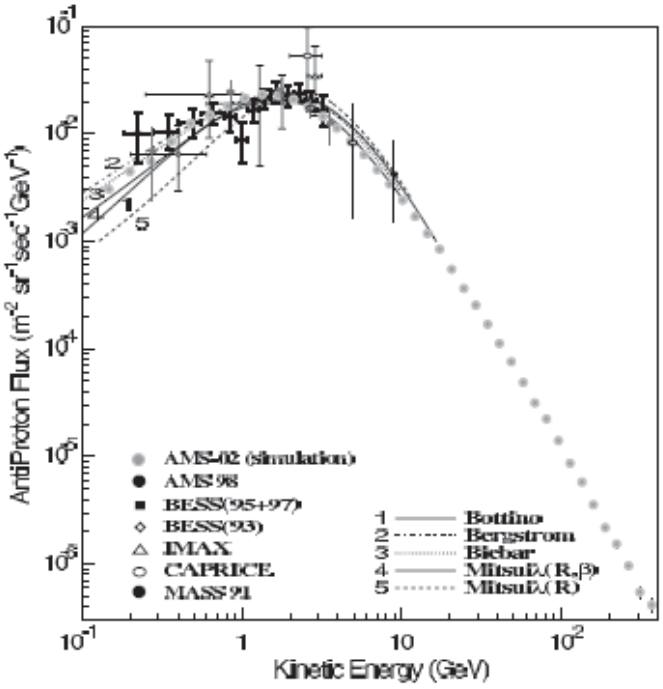

Figure 1.12: A compilation of antiproton measurements. A simulated measurement of the AMS-02 experiment on the ISS is also reported. For balloon data and models see [49] and references therein. For AMS-01 data see [50].

High energy gamma rays

High energy gamma rays are a rare ($O(10^{-5})$) component of cosmic radiation which is not traditionally included in a CR review paper. However, high energy gamma rays are produced by the same sources producing high energy CR and carry complementary information. They should then be considered when discussing astro particle physics, in particular since their study could give important contributions in understanding the problem of the origin of dark matter. Their energy spectrum could, in fact, be influenced by exotic sources such as neutralino annihilations taking place at the center of the galaxy. Most high energy gamma ray data has been collected by the EGRET experiment on the CGRO satellite during the 1990s. Since the end of the CGRO program (1999-2000) there has been

no experiments measuring high energy gamma rays in space. During the present decade there will be many space borne experiments which will be able to measure high energy gamma rays: AGILE [51] (2006) a small scientific mission of the Italian Space Agency, AMS-02 on the International Space Station (2008) [52, 53, 54] and GLAST [55] (2006). These experiments will be able to cover the region up to 300 GeV competing with ground based Cerenkov detectors which meanwhile will try to lower their threshold below 50 GeV.

Indirect search for dark matter

The presence at all scales in our universe of non-luminous components of matter, dark matter (DM) [56, 57], is possibly the most fascinating problem in astroparticle physics. The most promising candidate for the cold dark matter particles (CMD) is the *neutralino*: the Lightest Supersymmetric Particle (LSP). Supersymmetry links the existing standard model particles to a set of new, heavier, superparticles through R-parity conservation, where R is a combination of the particle spin, lepton and baryon numbers. The conservation of R-parity requires that the LSP is stable. LEP results suggest that the LSP is heavy ($m_\chi > 45$ GeV) [58] and therefore these particles could be a good DM candidate in the cold dark matter (CDM) scenario. Unfortunately SUSY is a theory with many parameters and is still poorly constrained.

Neutralinos can be detected by indirect methods by looking at annihilation products ($\overline{p}$, e^+, γ, ν) in cosmic rays, that would take place in the most dense regions of our galaxy, for example its centre or in other existing DM clumps.

Direct search for nuclear antimatter

The disappearance of antimatter [59, 60] is one of the most intriguing puzzles in our current understanding of the structure of the universe. Absence of nuclear antimatter from the scale of our galaxy to the scale of the local supercluster is experimentally established at the level of one part in 10^6 by direct CR searches and indirect methods such as the study of the energy spectrum of the diffuse gamma rays flux. For a genuine antimatter signal one should look to nuclei heavier than $\overline{p}$ since secondary $\overline{p}$ can be easily produced at the level 10^{-4} in high energy hadronic interaction of CR with the IM. This probability quickly vanishes with increasing atomic number. For $\overline{D}$ the secondary production is at the level of 10^{-8} or less and already for ${}^4\overline{He}$ it is well below 10^{-12}. This is why the unambiguous observation

of an $^4\overline{He}$ at the level of one part in a billion or more would have profound implications on our understanding of baryogenesis. The last 35 years of experiments on balloons have pushed the limit on the $^4\overline{He}$ to the level of less than about one part in a million (figure 1.13). Recently the AMS-01 spectrometer, during a 10 days precursor flight on the Shuttle, has reached the same level of sensitivity. In the coming years AMS-02 will eventually reach a sensitivity a thousand times better, reaching rigidities of the order of a TV.

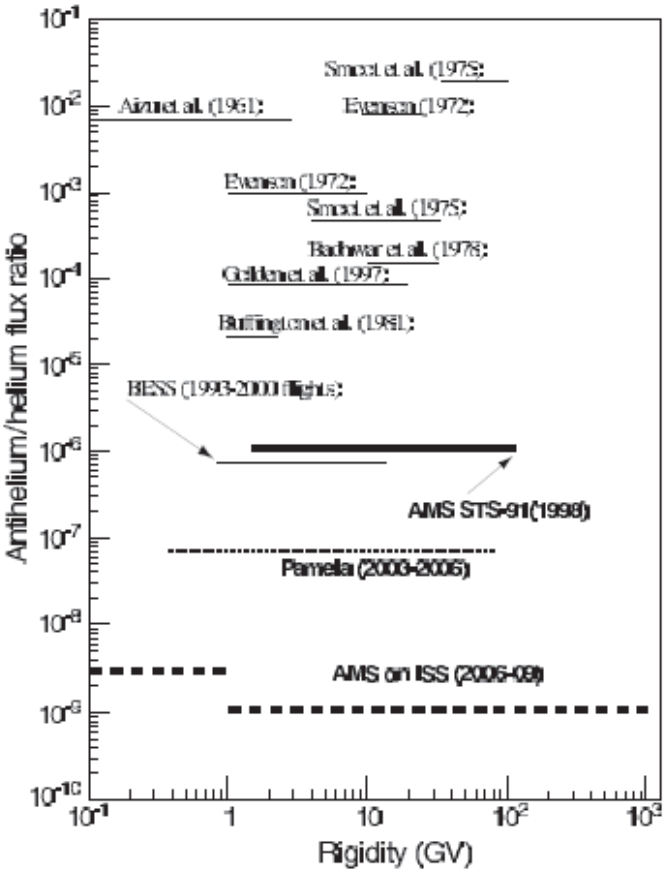

Figure 1.13: Antimatter limits. For the references see [61].

Chapter 2

Identification of the Cosmic nuclei with the TOF scintillators

In the firsts sections of this chapter, the physical processes that explain the passage of the particles through the matter, and the scintillation mechanisms will be reviewed. At the end of this chapter the TOF sub-detector of the AMS-02 experiment and the test beam results regarding the charge measurement and resolution will be described.

2.1 Passage of particles through the matter

Two principal features characterize the passage of the charged particles through the matter [62]: (1) a loss of energy by the particle and (2) a deflection of the particle from its incident direction. These effects are primarily the result of two processes:

1. inelastic collisions with the atomic electrons of the material,

2. elastic scattering from nuclei.

These reactions occur many times per unit path length in matter and it is their cumulative result which accounts for the two principal effects observed.

Of the two electromagnetic processes, the inelastic collisions are almost solely responsible for the energy loss of heavy particles in matter. In these collisions energy is transferred from the particle to the atom causing an ionization or excitation of the latter. The amount transferred in each collision is generally a very

small fraction of the particle's total kinetic energy; however, in normally dense matter, the number of collisions per unit path length is so large, that a substantial cumulative energy loss is observed even in relatively thin layers of material.

Elastic scattering from nuclei also occurs frequently although not as often as electron collisions. In general very little energy is transferred in these collisions since the masses of the nuclei of most materials are usually large compared to the incident particle. Nevertheless, the major part of the energy loss is still due to atomic electron collisions.

The inelastic collisions are statistical in nature, occurring with a certain quantum mechanical probability. However, because their number per macroscopic path length is generally large, the fluctuations in the total energy loss are small and one can meaningfully work with the average energy loss per unit path length. This quantity, often called the *stopping power* or simply *dE/dx*, was first calculated by Bohr using classical arguments and later by Bethe, Bloch and others using quantum mechanics.

The correct quantum mechanical calculation was first performed by Bethe, Bloch and others authors [62]. The formula obtained is then

$$-\frac{dE}{dx} = 2\pi N_a r_e^2 m_e c^2 \rho \frac{Z}{A}\frac{z}{\beta}^2 \Big[ln\Big(\frac{2m_e\gamma^2 v^2 T_{max}}{I^2}\Big) - 2\beta^2\Big]. \tag{2.1}$$

Equation 2.1 is commonly known as the *Bethe-Bloch formula* and is the basic expression used for energy loss calculations. In practice, however, two corrections are normally added: the *density effect* correction δ, and the *shell* correction C, so that

$$-\frac{dE}{dx} = 2\pi N_a r_e^2 m_e c^2 \rho \frac{Z}{A}\frac{z}{\beta}^2 \Big[ln\Big(\frac{2m_e\gamma^2 v^2 T_{max}}{I^2}\Big) - 2\beta^2 - \delta - 2\frac{C}{Z}\Big], \tag{2.2}$$

with

$$2\pi N_a r_e^2 m_e c^2 = 0.1535 MeV cm^2/g$$

and where:

r_e:	classical electron radius = 2.817×10^{-13}	ρ:	density of absorbing material
		z:	charge of incident article in units of e
m_e:	electron mass		
N_a:	Avogadro's number $= 6.022 \times 10^{23} mol^{-1}$	$\beta =$	v/c of the incident particle
		$\gamma =$	$1/\sqrt{1-\beta^2}$
I:	mean excitation potential	δ:	density correction
Z:	atomic number of absorbing material	C:	shell correction
		T_{max}:	maximum energy transfer in a single collision
A:	atomic weight of absorbing material		

The maximum energy transfer is that produced by the head-on or *knock-on* collision. For an incident particle of mass M, kinematics gives

$$T_{max} = \frac{2m_e c^2 \eta^2}{1 + 2s\sqrt{1+\eta^2+s^2}} \tag{2.3}$$

where $s = m_e/M$ and $\eta = \beta\gamma$. Moreover, if $M \gg m_e$, then

$$T_{max} \cong 2m_e c^2 \eta^2.$$

The mean excitation potential, I is the main parameter of the Bethe-Bloch formula and is essentially the average orbital frequency $\overline{\nu}$ from Bohr's formula times Planck's constant, $h\overline{\nu}$. It is theoretically a logarithmic average of ν weighted by the so-called oscillator strengths of the atomic levels. In practice, this is a very difficult quantity to calculate since the oscillator strengths are unknown for most materials. Instead, values of I for several materials have been deduced from actual measurements of dE/dx and a semi-empirical formula for I vs Z fitted to the points.

The quantities δ and C are corrections to the Bethe-Bloch formula which are important at high and low energies respectively.

The density effect arises from the fact that the electric field of the particle also tends to polarize the atoms along its path. Because of this polarization, electrons far from the path of particle will be shielded from the full electric field intensity. Collisions with these outer lying electrons will therefore contribute less to the total energy loss than predicted by the Bethe-Bloch formula. This effect becomes more important as the particle energy arises. As the velocity increases, distant collisions contribute more and more to the total energy loss. Moreover, this effect depends on the density of the material, since the induced polarization will be greater in condensed materials than in lighter substance such as gases.

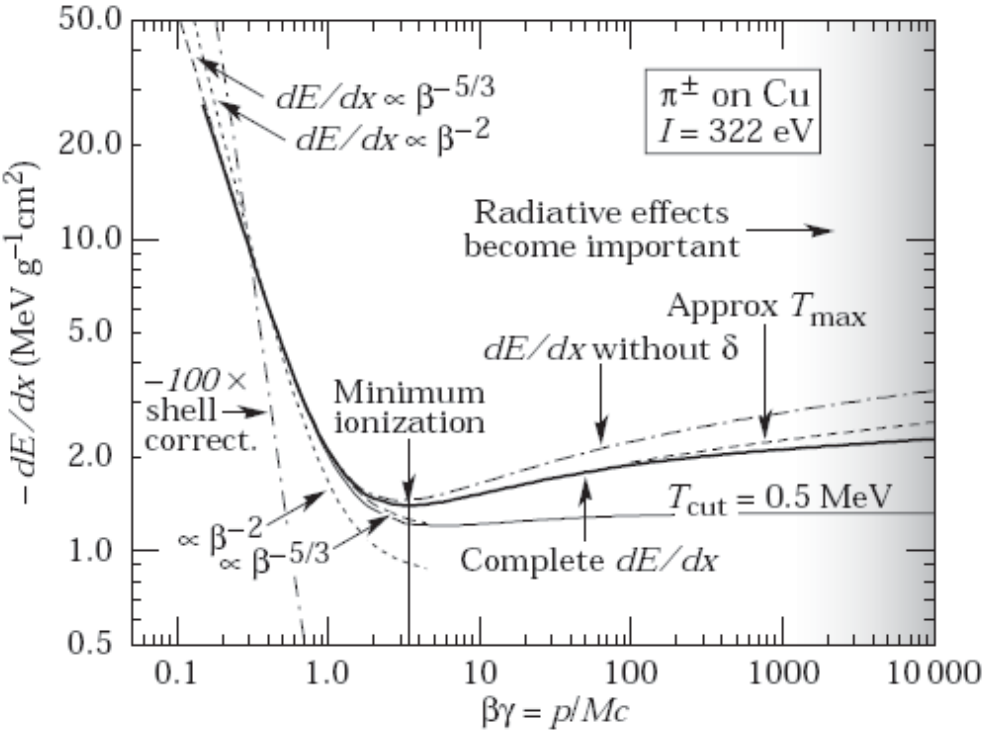

Figure 2.1: Energy loss rate in copper. The function without the density-effect correction, δ is also shown, as is the loss rate excluding energy transfers with $T < 0.5$ MeV. The shell correction is indicated. The conventional β^{-2} low energy approximation is compared with $\beta^{-5/3}$.

The shell correction accounts for effects which arise when the velocity of the incident particle is comparable or smaller than the orbital velocity of the bound electrons. At such energies, the assumption that the electron is stationary with respect to the incident particle is no longer valid and the Bethe-Bloch breaks down. This correction usually is small and it's given by an empirical formula.

In addition to the shell and density effects, the validity and accuracy of the Bethe-Bloch formula may be extended by including a number of other corrections pertaining to radiation effects at ultra-relativistic velocities, kinematic effects due to the assumption of an infinite mass for the projectile, higher-order QED processes and so on, but these are usually negligible to within $\simeq 1\%$.

At non relativistic energies the Bethe-Bloch formula is dominated by the overall $1/\beta^2$ factor and decreases with increasing velocity until about $v \simeq 0.96c$, where a minimum is reached. Particles at this point are known as *minimum ionizing particle* (MIP). Note that the minimum value of dE/dx rises again due to the logarithmic dependence of the formula (2.2). This *relativistic rise* is practically canceled, however, by the density correction as seen in figure 2.1.

2.2 Scintillation mechanism

The scintillation detector is one of the most often and widely used particle detection devices [62]. It makes use of the fact that certain materials when struck by a particle or radiation, emit a small flash of light, i.e. a *scintillation*. In general the scintillator signal is capable of providing a variety of information. Among is most outstanding features are:

- Sensitivity to energy lost by the crossing particle.
- Fast time response.
- Pulse shape discrimination.

Scintillator materials exhibit the property known as *luminescence*. Luminescent materials, when exposed to certain kinds of energy (light, heat, radiation, etc.) absorb and remit the energy like visible light. If the re-emission occurs immediately after absorption or more precisely within 10^{-8} s (being roughly the time taken for atomic transitions), the process is usually called *fluorescence*. However, if remission is delayed because the excited state is meta-stable, the process is called *phosphorescence* or *afterglow*. In such cases, the delay time between absorption and emission depends on the material.

As a first approximation, the time evolution of the emission process may be described as a simple exponential decay

$$N = \frac{N_0}{\tau} \exp\left(\frac{-t}{\tau}\right), \tag{2.4}$$

where N is the number of photons emitted at time t, N_0 the total number of photons emitted, and τ the decay constant. In general, a good detector scintillator should satisfy the following requirements:

1. hight efficiency for conversion of exciting energy to fluorescent radiation,
2. transparency to its fluorescent radiation so as to allow transmission of the light,
3. emission in a spectral range consistent with the spectral response of existing photomultipliers,
4. a short decay constant, τ.

Birks in 1951, assuming the response of organic scintillators to be ideally linear, explained the deviations as being due to quenching interactions between the excited molecules created along the path of incident particle, i.e. interactions which drain energy which would otherwise go into luminescence. Since a higher ionizing power produces a higher density of excited molecules, more quenching interactions will take place for these particles. In this model, the light output per unit length, dL/dx, is related to the specific ionization by

$$\frac{dL}{dx} = \frac{A\frac{dE}{dx}}{1+kB\frac{dE}{dx}}, \tag{2.5}$$

with A: absolute scintillation efficiency; kB: parameter relating the density of ionization centers to dE/dx.

In practice, kB is obtained by fitting Birk's formula to experimental data. As observed experimentally, the formula is reduced to a linear relationship for small dE/dx

$$\frac{dL}{dx} \simeq \frac{dE}{dx}. \tag{2.6}$$

However, for large dE/dx, the formula differs in its predictions.

Not all the organic scintillators are composed by a single material. Most of the organic scintillators to increase the efficiency in a particular application, make use of a *wavelength shifters* which absorbs light of one frequency and emits it into another frequency. This can also be added to make the spectrum compatible with a photomultiplier cathode. Chou in 1952, taking into account a solution of two materials, with different probabilities of emissions and quenching, and with a probability of photons transmission between themselves, suggested deviations at the second order on the Birks formulae (2.5) in order to better fit the experimental data

$$\frac{dL}{dx} = \frac{A(dE/dx)}{1+kB(dE/dx)+C(dE/dx)^2}. \tag{2.7}$$

2.2.1 Attenuation length

The *attenuation length* parameter of a scintillator is defined as that length of the scintillator after which the light intensity is reduced by a factor e^{-1} [62]. The light is lost in two basic ways: the light escapes through the scintillator boundaries, and the scintillator material absorbs the light. For small detectors, the latter effect is negligible. If the dimensions of the counter are such that the total path lengths traveled by the photons are comparable to the attenuation length, then the absorption must be considered. The light intensity as a function of length is then

$$L(x) = L_0 \exp\left(\frac{-x}{l}\right), \tag{2.8}$$

where l is the attenuation length, x the path length traveled by the light and L_0, the initial light intensity. Since a typical attenuation length is on the order of $\simeq 1$ m or more, it is clear that only very large detectors are affected.

The scintillators attenuation depends on the geometry (internal reflections and dispersion) and on the material (bulk attenuation length) of the scintillator.

2.3 The scintillator TOF counters

The Time Of Flight (TOF) system of the AMS-02 detector, is composed by 4 planes of plastic organic scintillator paddles (see figure 2.2), two above (upper TOF) and two below (lower TOF, see also figure 2.3) the magnet [22], [63], [64], [65]. It has four following essential tasks:

1. it has to generate the fast trigger signal of AMS-02. This signal is also used by the TOF electronics as the common reference time for all the counters, and for this task it covers all the acceptance of 0.4 m^2st.

2. The particle time of flight between the upper and the lower TOF is used to measured its velocity $\beta = v/c$, when the crossing positions (hence the track length) are known. The TOF counters design gives from the two sides, an independent measure of the position.

3. The time of flight resolution of the TOF is able to distinguish between upward and downward going particles with a rejection power in order to separate the $\overline{He}$ signal at level of 10^{-9} from the up going nuclei. After the TOF

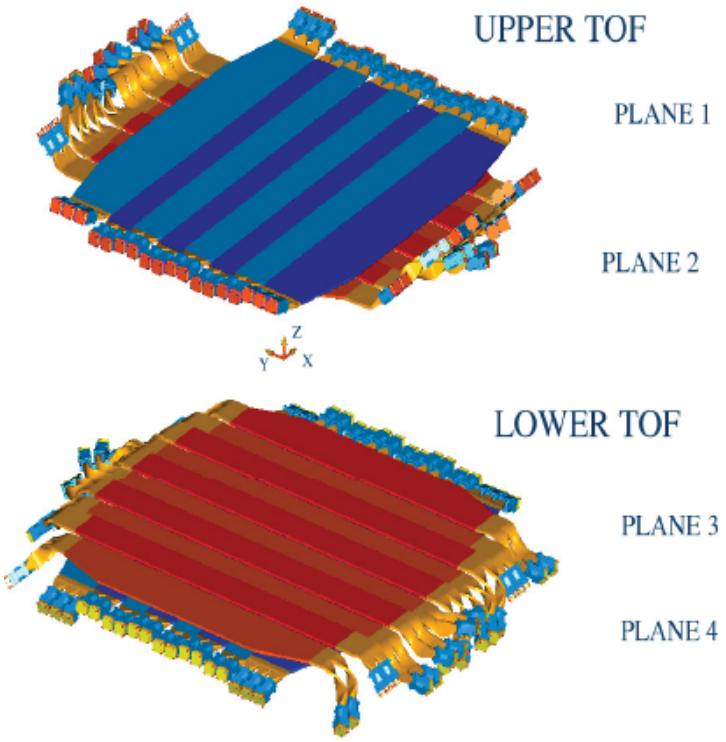

Figure 2.2: 3D view of the AMS-02 TOF scintillator paddles. The TOF is composed by 4 planes made of plastic scintillator paddles two above (upper TOF) and two below (lower TOF) the magnet with a distance of 1.20 m between upper and lower.

measurement of the particle direction, the Tracker measurement of the trajectory curvature is sufficient to distinguish between negative and positive electrical charges, that are deflected in opposite directions by the magnetic field up to impulse of the order of 1.5 TeV/c.

4. The energy loss measurement is used by the TOF system to generate a special flag for high Z charge events, used at the second level trigger. In addition, the TOF charge measurement is able to separate light ions from protons and He nuclei.

The 4 TOF planes form two structures, as shown in figure 2.2, placed above and below the magnet, made of 1 cm thick plastic scintillator paddles of differ-

ent shapes: the outermost counters have a trapezoidal *(x, y)* projection, while all other counters have a rectangular shape, as shown in figure 2.4. The shape of the external counters was chosen to match the desired geometrical aperture still satisfying the severe weight constraints of the TOF. Each structure has one plane with counters whose longitudinal axis is parallel to the field direction inside the spectrometer (that defines the x axis), and counters along the y direction in the other plane, in order to have a certain granularity at the trigger level. First and fourth planes have 8 counters along the x axis, while second and third planes have 8 and 10 counters along y, respectively. Each couple of adjacent TOF planes is enclosed in a carbon fiber light tight envelope. The inner rectangular counters are 12 cm wide in order to accommodate two Hamamatsu R5946 photomultipliers per side, and each two adjacent parallel counters have 0.5 cm overlap, in order to not have dead zones in the acceptance. Hence, at trigger time one has inner matrices of 6×6 and 6×8 of square *(x, y)* cells with 11.5 cm sides, plus surrounding cells of larger granularity. About 90% of all acceptable tracks will cross the central square cells.

Figure 2.3: The lower TOF builded in the Bologna INFN laboratories.

The plastic TOF scintillator counters type EJ-200 furnished by the Eljen-Technology (Texas,USA), have the main characteristics shown in the following table:

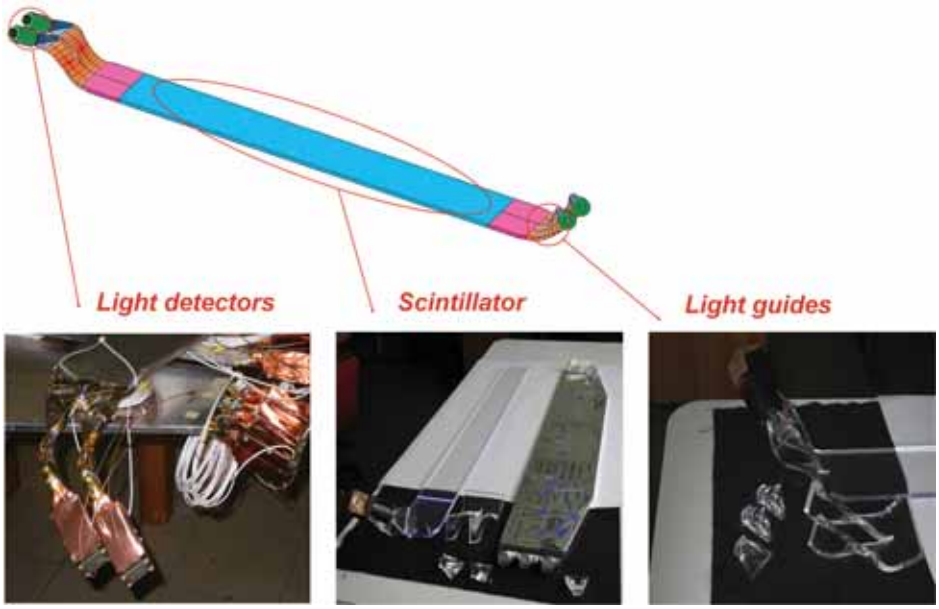

Figure 2.4: A sketch of a TOF counters of AMS-02 with the photomultipliers, the scintillator paddle and the tilted light guides.

Polymer	Polyvinyl-toluene
Luminous response	64 % Anthracene
Photons/1 MeV	10000 e^-
Rising time	0.9 ns
Falling time	2.1 ns
Density	$1.032 g/cm^3$
Refraction index	1.58
Attenuation length	3.80 m

The sensitive material is an organic plastic paddle (polyvinyl-toluene) whose scintillator light is internally reflected until it reaches the two edges, where plexiglas light guides bring it to the photomultipliers. The figure 2.4 shown a typical counter with the light guides and the photomultipliers.

The light guides consist of two different parts: a straight *extender* that prolongs the scintillator paddle is connected to two bended and twisted pieces that end with *conical* junctions whose the PMTs are fixed to. All the conical parts are identical to match the rectangular shape of the counter and the light guide with the circular

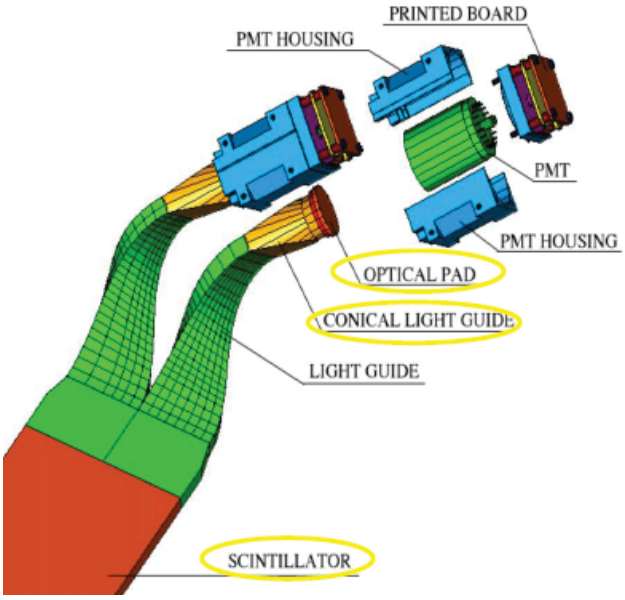

Figure 2.5: The mechanical fixation of the PMT to the conical part of the light guide is realized through the PMT housing.

photocathode of the PMT.

Between the guide and the PMT window a soft transparent pad, in Dow Corning 93-500 material, is placed, that guarantees the needed optical couplings. The phototube is enclosing into a black plastic box (figure 2.5), to be connected with the light guide. The scintillator, extenders and light guides are wrapped by a thin Mylar foils, that improves reflectivity blocking external light and protects the surfaces from dust and small debris that may be produced by the enclosing carbon fiber 0.5 mm thick boxes, that provide the needed rigidity. Light tightness is provided by a large carbon fiber envelope 0.7 mm thick that encloses the couple of adjacent planes and their photomultipliers.

2.3.1 The fine-mesh photomultipliers

Time Of Flight System of AMS-02 will operate in the strong (2-3 kG) and badly shaped fringing field of the dipole magnet (figure 2.6). This fact led to the choice of the R5946 Hamamatsu *fine-mesh* tubes (figure 2.7), for their intrinsic capability of tolerating the magnetic field. The PMT has a bialkali photocathode, a boron-

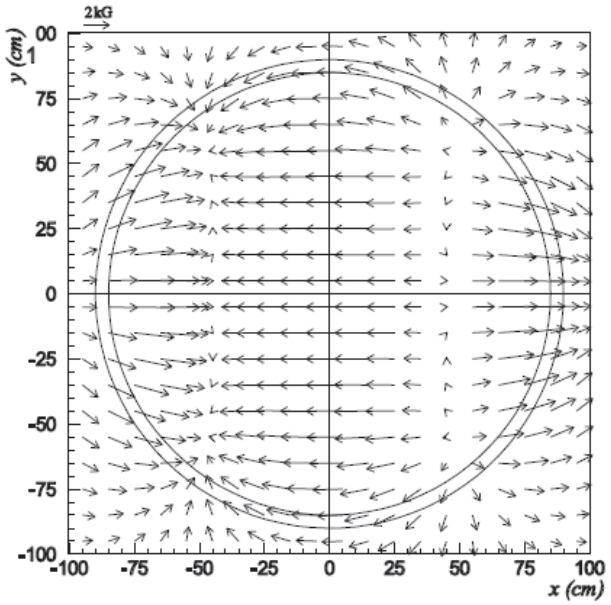

Figure 2.6: AMS-02 field map in the TOF PMT horizontal plane. The ring shows where PMTs are positioned [66].

Figure 2.7: The Hamamatsu fine mesh R5946 photomultiplier tube.

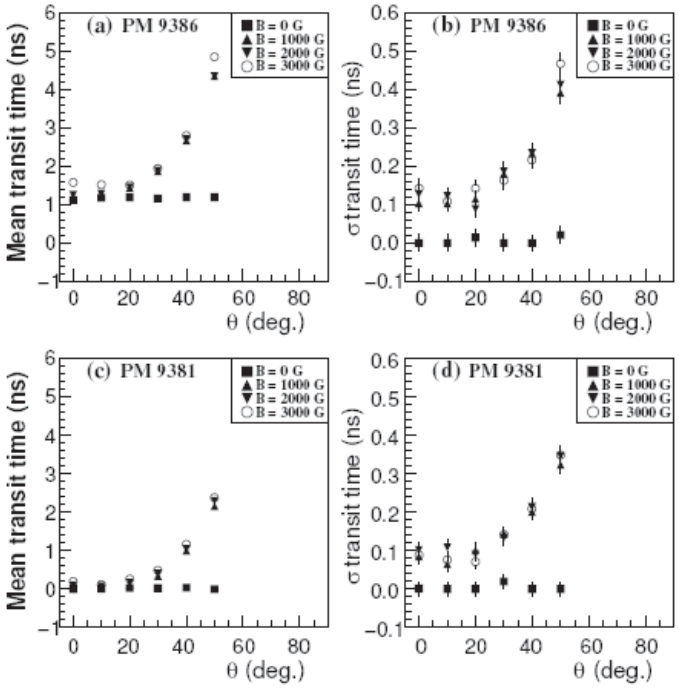

Figure 2.8: Magnetic field effects on the time measurement [66].

silicate glass window and 16 bialkali dynodes. The spectral response ranges from 300 to 600 nm with a maximum response at $\simeq 420$ nm (corresponding to a quantum efficiency of about 20%). The PMT characteristics are show on the following table:

Dimension	38 mm
λ (max sensitivity)	375 nm
Gain	10^6
Dark current	5 nA
Rising time	1.9 ns
Transit time	7.2 ns
Spread transit time	0.35 ns
Number of dynodes	16

The PMTs were tested in magnetic field [66] and the most critical parameter was found to be the time response of the phototube. In fact for $\theta \geq 35^\circ$ the transit

time and the transit time resolution worsen badly (figure 2.8). The choice of the twisted and tilted light guides has been done in order to keep the angles of the TOF PMTs below this critical value. The light from every paddle is transmitted to two PMTs per side for redundancy. The two PMTs on each side of the counters are chosen so as to have similar responses. Moreover, high gain PMTs are put at the critical positions, so that their voltage supply can be increased, if necessary, to compensate for the worsening of their timing response.

2.4 The TOF scintillator charge resolution

Prototypes of AMS-02 TOF polyvinyltoluene scintillator counters were tested at CERN in 2002 and 2003 with standard NIM and CAMAC electronics at the SPS ion beam facility [63].

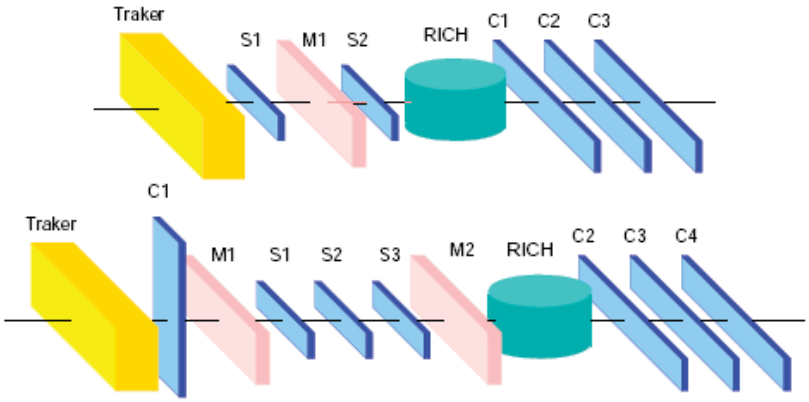

Figure 2.9: Detectors used during the test beam in 2002 (upper) and in 2003 (lower) [67].

Figure 2.9 shows the experimental set-ups for the 2002 and 2003 tests beam. In 2002 the set-up was composed by RICH and Tracker prototypes and three TOF counters (C_1, C_2 and C_3), plus two more counters for the trigger (S_1, S_2) and one multi wire proportional chamber (M_1). In 2003 the set up was changed in two wire chambers (M_1, M_2), three counters (S_1, S_2 and S_3) for the trigger, and four TOF counters (C_1, C_2, C_3 and C_4) with straight and tilted guides.

In 2002 the goal of the beam test was the study of the time and charge resolution of the scintillators in order to choose between different kinds of scintilla-

tors for the TOF of AMS-02: one scintillator was from the Bicron Industry, one from the Eljen Technologies Industry and the third one was one already used in AMS-01. From the test beam results we choose, for the TOF detector, the Eljen Technologies scintillators, that give the time of flight resolution of 150 ps for 1 MIP and of $(60 \div 70)$ ps for $Z = 10$. The time of flight resolution improves with increasing particle charge, reaching a limiting level dominated by the electronic noise. This level was between 50 and 60 ps for the standard electronics used during the ion beam test.

The 2003 test beam goal was the study of the time and charge resolution of the scintillators at hight Z of the TOF counters with different light guides: the light guides used in the four counters were short and straight in C_1 e C_4, tilted and twisted in C_2 and only tilted in C_3.

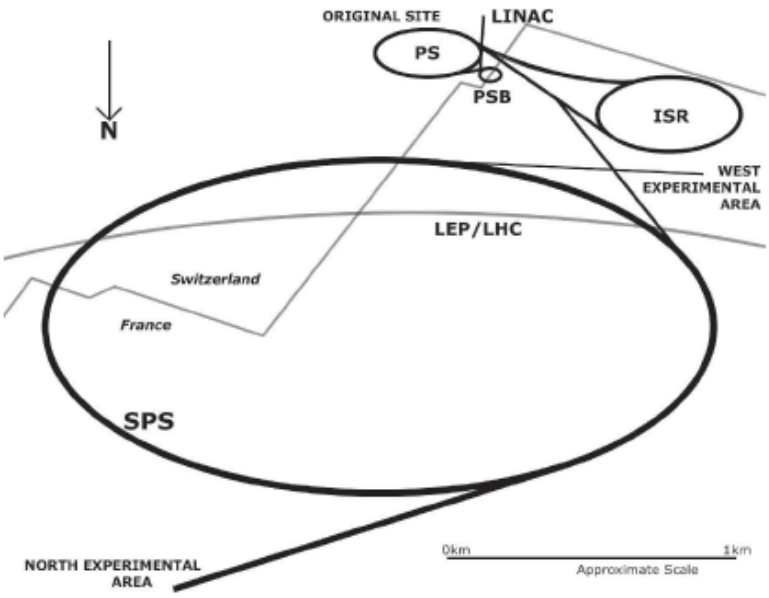

Figure 2.10: A projection of the accelerator system SPS at CERN.

The beam production (figure 2.10) starts on the LINAC (LINear ACcelerator) that accelerates protons produced into an hydrogen ionization chamber. These protons are accelerated to GeV energies into the booster (PSB), that is a small circular accelerator. From the the booster, the particles reach the Proton Synchrotron (PS), where the protons are again accelerated and are finally extracted to collide

against a heavy target to produce a secondary beam of heavy ions. In 2002 a Pb target was used and an In one in 2003. The partial ionized nuclei are then injected into the bigger ring of the Super Proton Synchrotron (SPS) for further acceleration. Finally the ion beam with 158 GeV/c is directed inside the SPS against a Be target ($10 \div 30$ cm long), producing secondary nuclei from proton to the incident ion itself with a small spread in β. Mass over charge selection was made possible by tuning the magnets of the T8 selection line. Runs with different values of *A/Z* were used to get large statistic of all important CR species. In particular it has been chosen:

- *A/Z* = 1 : to have a beam of protons;
- *A/Z* = 2 : to have ^4He and almost all stable nuclei up to iron;
- *A/Z* = 3/2 : to have ^3He;
- *A/Z* = 7/4 : to study the ^7Be;
- *A/Z* = 2.35 : typical of the Li.

2.4.1 The events selection

The counters are large compared to the beam spot, whose diameter is about 3 cm. Hence they picked up a lot of secondary particles that are off the beam axis. In order to clean the sample of single ions crossing each counter, it is necessary to apply a number of cuts to the sample.

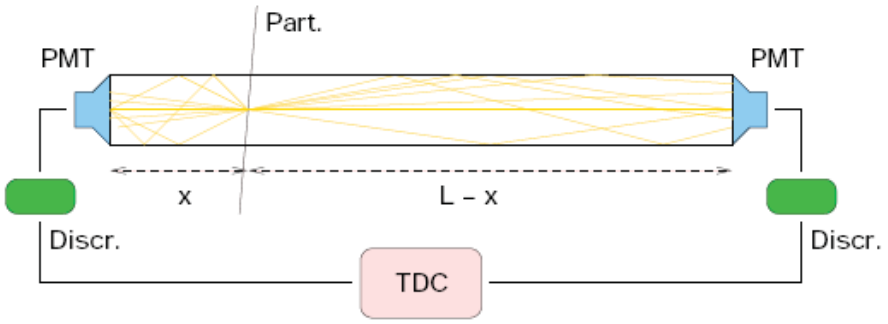

Figure 2.11: We measure the times of the two sides using the TDC [22].

In order to exclude the secondary off-axis particles that hit the counters over the whole area, we considered the half difference between the time measured in both ends of the same counter:

$$\Delta t_i = \frac{(t_{i,left} + x/v) - [t_{i,right} + (L-x)/v]}{2} = \frac{x}{v} - \frac{L}{2v} \tag{2.9}$$

where t_i is the particle crossing time for the counter i, L is the counter length, v is the effective light speed inside the scintillator, and x is the distance of the crossing position with respect to one of the two sides (see figure 2.11). Considering that the beam conditions were $x_{max} \approx 3$ cm and $v \simeq 16.5$ cm/ns then Δt_i dispersion was around 0.2 ns.

An other events cut was made in order to remove the events given when more than one secondary particle at the same time, crossed the scintillators. We removed them by the known of the mean counter time that corresponds to the sum of the delays between the TDC start and the arrival of the signals from both ends of the same counter

$$t_i = \frac{t_{i,left} + t_{i,right}}{2} = \frac{(t_0 + \frac{x}{v}) + (t_0 + \frac{L-x}{v})}{2} = \frac{2t_0 + \frac{L}{v}}{2} = t_0 + \frac{L}{2v}. \tag{2.10}$$

This measure is independent from the crossing position and the deviation of the mean time are caused by secondary particles. A gaussian fit reveals the mean values $\langle t_i \rangle$ and the standard deviation. As first set of cuts, it is required that events not consistent with $\langle t_i \rangle$ within one standard deviation are discarded.

The last cut is applied to all the events due to the slowly secondary particles that cross the scintillators close to the center that cannot be removed by the others two cuts. From the time of flight measure between each couple of counters we found a distribution that gives a valuation of the velocity of the crossing particles. We made a gaussian fit of the distribution and we excluded the events that were far more than one standard deviation from the medium value.

Apart from a constant term ($L/2v$), Δt_i gives the longitudinal coordinate x along the scintillator ($v \simeq 15$ cm ns^{-1} has been measured in the INFN laboratories in Bologna). The time resolution of the counters is of the order of 0.1 ns, hence the beam particles give a fixed time difference, because the spot radius is approximatively equal to the spatial resolution $\sigma_x \approx 1.5$ cm of the counters obtained with the half time difference measurement.

In general, off-axis particles will give a different value for Δt, hence they can be discarded by requiring that the half time difference is within one standard deviation from its mean value for each counter. A couple of secondaries that hit the

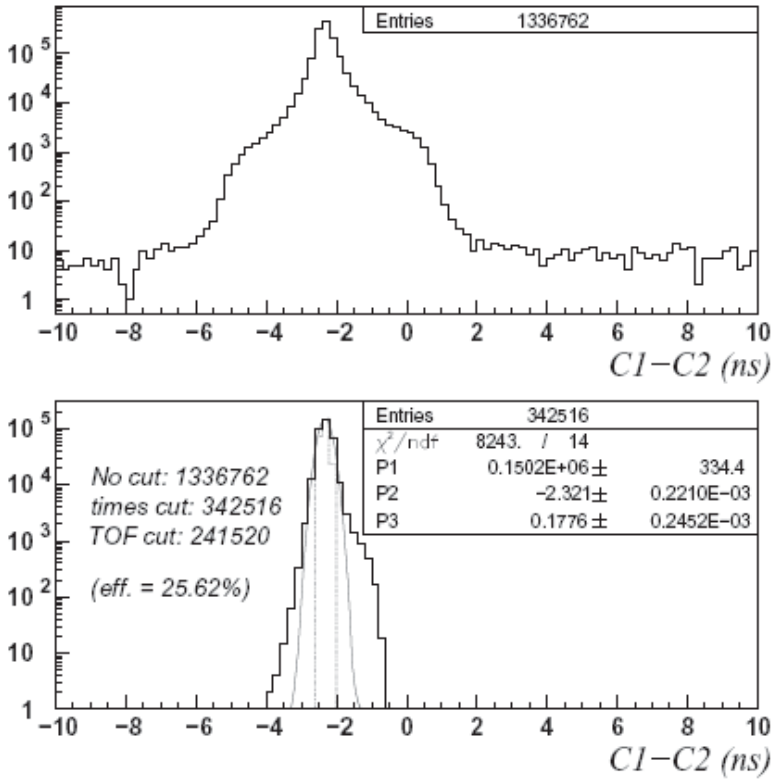

Figure 2.12: Time of flight between the first two counters without cuts (upper panel) and with mean time and half time difference cuts (lower panel). Only events within 1 standard deviation from the gaussian mean are kept.

counters in symmetric positions with respect to the beam spot cannot be rejected by this condition, but they produce a wrong measurement of the mean time, hence they are discarded by the other condition.

Figure 2.12 shows the time of flight between two counters without cuts (upper panel) and with mean time and half time difference cuts (lower panel). After the mean time and half time difference conditions the residual particle time of flight has a distribution that can be fitted by a Gaussian with standard deviation of 160-180 ps. Discarding also the events with time of flight measurements outside one standard deviation from the mean values, it is possible to obtain a quite clean

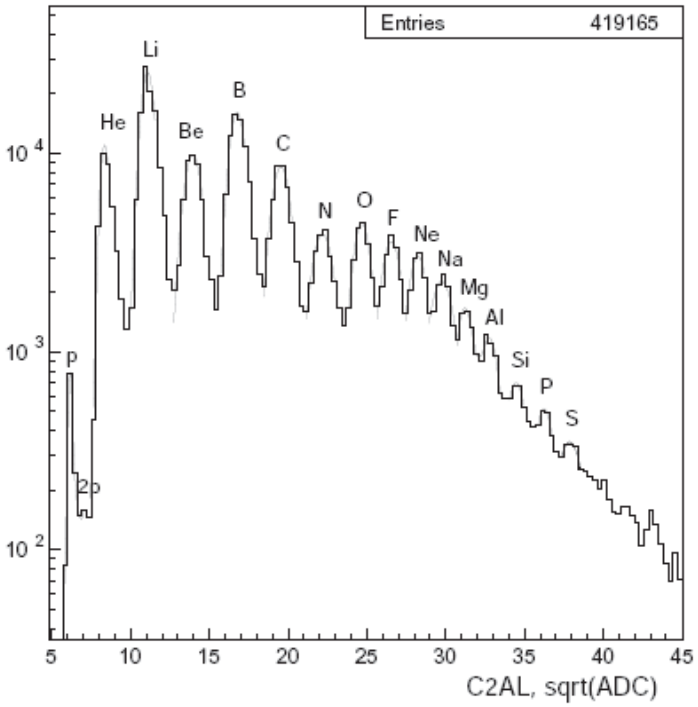

Figure 2.13: The ADC measures the integral of the charge Q in output from the PMT. After the cuts, the peaks relatives to the single charge are easily visible and can be approximate to a gaussian or landau shapes ([68] and references therein).

sample of appreciable statistics (25.6% of the considered events) useful to study the charge resolution.

2.4.2 Charge peaks

One of the most important informations gained with the beam tests is about the charge resolution of the AMS-02 TOF counters. The charge of a particle crossing the scintillator can be measured by looking at its energy loss: for particles heavier than electrons the mean rate of energy loss is a function (the well known Bethe Bloch equation) of the medium and of the incident particle velocity and charge. The charge peaks are well separated for the nuclei with atomic number $Z \geq 15$, as

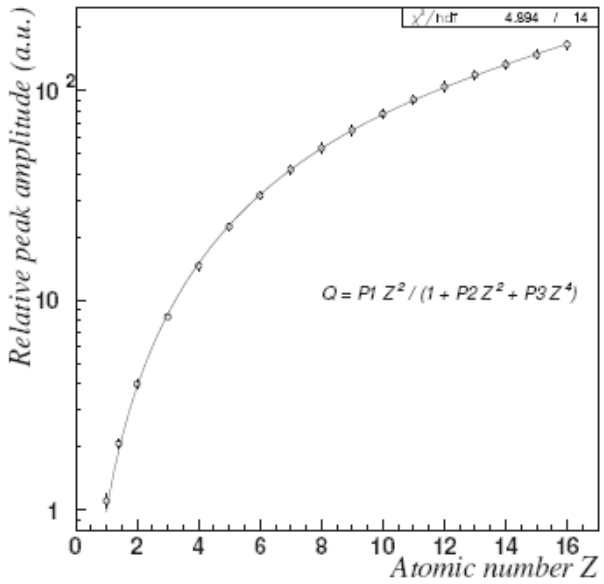

Figure 2.14: Fit of the measured average amplitude vs the atomic number [68].

shown in figure 2.13, where the events distribution as function of the square root of the ADC counts is shown, for a single counter side.

The scintillator response, as already explained in previous sections, is not a simple linear function of the ionization energy density, but it is well modeled by the Birks-Chou law [62]. For the particles with equal β that cross the same scintillator material and thick, the mean energy loss is a function only of their atomic number. The luminous response vs Z for all the tested scintillators, give compatible results. Figure 2.14 shows the global fit obtained with the averaged amplitude peaks of the four detectors. The uncertainties associated to each point are of the order of 5%.

To distinguish between the different crossing particle up to $Z = 16$ and more, became necessary to know the charge resolution of the scintillators. The measure of the integrated charge Q (for the PMTs with linear response) is proportional to the number of photoelectrons N_{pe} produced by the scintillator photons that hit the photocathode, multiplied to the gain of the dynodes chain G:

$$Q = qN_{pe}G, \tag{2.11}$$

where q is the inverse of the ADC-charge conversion factor. Then the charge

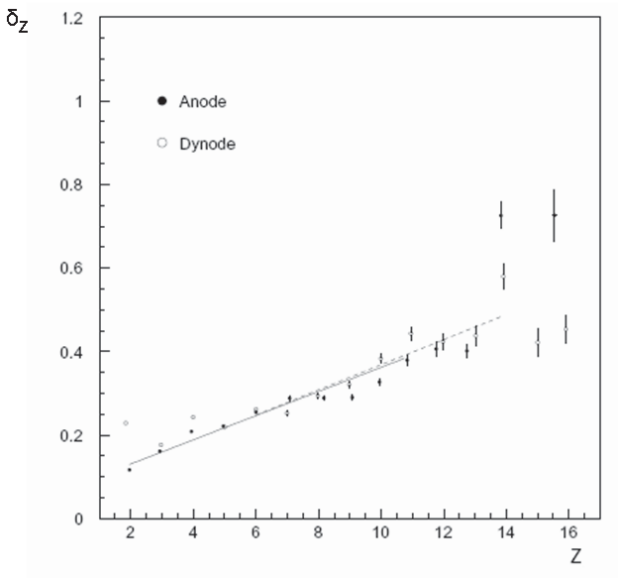

Figure 2.15: The charge resolution of the TOF counters relatives to the anode and dynode signals for a counter with straight light guides. The dynode resolution became important to distinguish bigger values of crossed charge particle in respect to one relatives the anode signals [68].

resolution σ_Q depends from three factors: (a) the Poisson distribution of the photoelectrons production on the photocathode, (b) the spread dues to the dynodes chain and (c) the electronic noise.

Q in first approximation, is proportional to Z^2 of the crossing particle, so σ_Z is proportional to Z like shown on figure 2.15, where high scatter at high Z values is due to the low events statistic [68].

Figure 2.16 shows the ions seen for the $A/Z = 2$ setting through the correlation between the charge measured by a TOF scintillator and the square root of the number of Cherenkov photoelectrons (proportional to Z) measured by the RICH prototype. Details on the beam design and performances are given in [69].

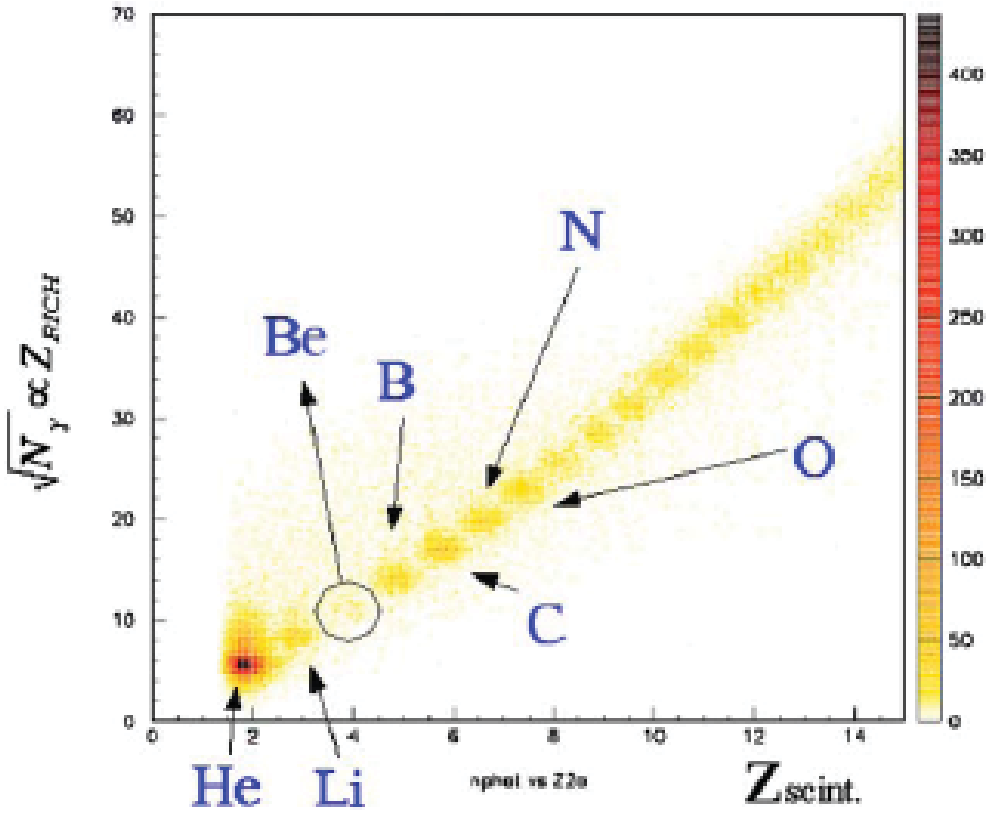

Figure 2.16: Correlation between a dE/dX scintillator and the square root of the number of Cherenkov photons [69].

Chapter 3

The charge measurement

In this chapter we describe the front-end electronics used to measure the charge collected by the photomultipliers when a crossing particle releases part of its energy in the TOF scintillators.

In order to measure the charge, a standard method is: first generate an analog voltage that is proportional to the integral of the analog input, then digitalize the obtained analog value using an Analog to Digital Converter (ADC).

The integral of the analog input (V_{in}) is performed by an integrator (see figure 3.1) giving in output an analog voltage (V_{out}) proportional to the input charge Q collected by the capacitor C_1

$$V_{out} = V_{C_1} = \frac{Q}{C_1};\ Q = \int I_{out}(t)dt. \tag{3.1}$$

Because the points 2 and 3 on figure 3.1, are connected to a common ground, one has

$$I_{out}(t) = -I_{in}(t) = -\frac{V_{in}}{R_1} \tag{3.2}$$

so

$$V_{out} = -\frac{1}{R_1 C_1}\int V_{in}(t)dt. \tag{3.3}$$

The analog value of V_{out} is then digitalized by a successive-approximation ADC, that works comparing the analog voltage in input to a known reference voltage until the best approximation is achieved. The ADC converts V_{out} to discrete digital numbers of 12 bits.

The TOF front-end boards for the charge measurement have been designed taking into account all this considerations.

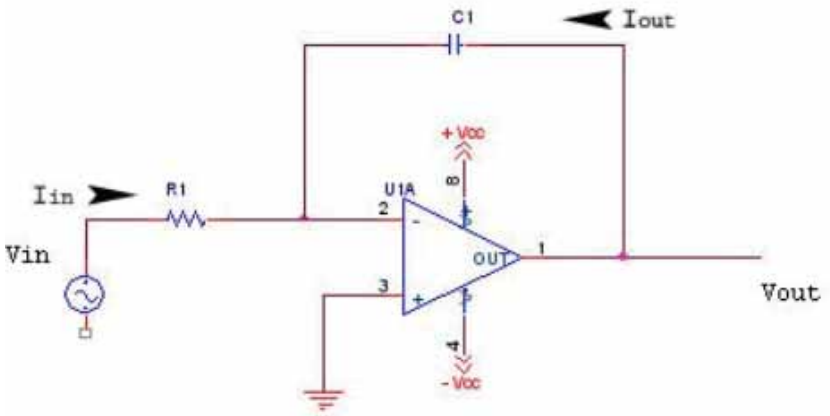

Figure 3.1: Scheme of an integrator.

3.1 The TOF front-end boards

The analog data coming from TOF and ACC phototubes are collected and digitalized by the TOF front-end boards, that are: the Scintillator Front End board for the Time measurement (SFET2[1]) necessary for the time and the charge measurement of the anode signals, the Scintillator Front End board for the ACC signals (SFEA2), necessary for the acquisition of the ACC anodes, and the Scintillator Front End board for the Charge measurement (SFEC) of the TOF dynode signals. All the data coming from the front-end boards are collected inside the Scintillator Data Reduction board (SDR2), where the Digital Signal Processor (DSP) on board compresses them, and memorizes the data on the RAM to be acquired by the general data acquisition system (DAQ) collecting data from all the AMS-02 sub-detectors.

While the SFECs are located directly on the detector, the other front-end boards are distributed inside the four TOF crates (S-crates). Each S-crate contains the same number and type of boards: one SDR2, four SFET2, one SFEA2, one scintillator pre-trigger board (SPT2). These boards are connected to the crate via VME connectors on the back plane [70].

[1]The number 2 at the end of the name of the TOF cards, means that the board consists of two identical modules (in this particular case two modules SFET), physically mounted on the same board. During normal operations, only one module is powered. The other one is necessary for redundancy.

3.1.1 The SFET2 boards

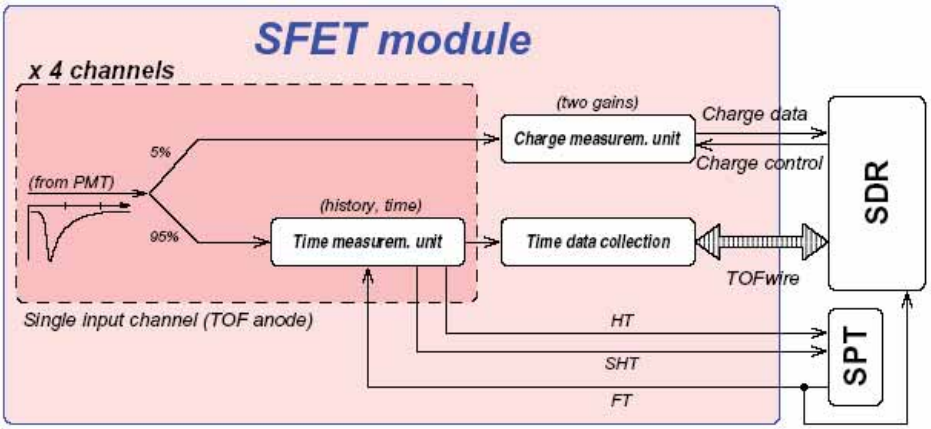

Figure 3.2: Block scheme of SFET board with the charge and time measurement units [71].

The SFET2 board consists of two identical SFET modules, located on the same PCB (printed circuit board). During normal operations, only one SFET module is powered. Each module is divided into two units: the time measurement unit and the charge measurement unit [71].

The SFET2 has 4 analog input lines, carrying the TOF anode signals coming from 8 PMTs, because of the anode signals are passively summed. Each input signal is split with a passive divider into two paths: the bigger fraction goes to the time measurement unit, whereas the smaller goes to the charge measurement unit. On figure 3.2 a scheme of the two units is shown.

The analog signals going to the time measurement units, are compared to three fixed thresholds, called *low threshold* (LT, roughly -20 mV), *high threshold* (HT, -60 mV), and *super-high threshold* (SHT, -350 mV). The digital signals produced by the comparators will be used to: measure the time in the case of LT; send a *charged particle* signal to the trigger logics in case of HT; and send a *big charge* signal to the trigger logics in case of SHT. In addition, LT and HT are used by the LeCroy MTD 135 TDC, that has two buffers per channel: the *time* and *history* buffers. The latter stores the four fronts of the time expansion and then freezes them. However, the history buffer can contain also additional pairs of elder fronts, produced by the crossing of the LT of pulses that are not followed by the FT,

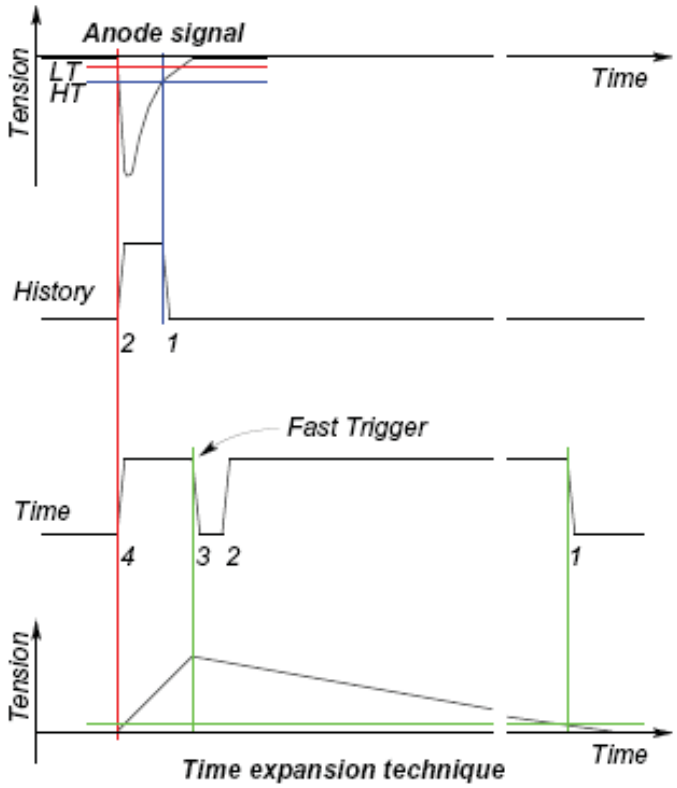

Figure 3.3: Schema of the time measurement. The analog signal is compared to fixed thresholds, and the precision of the time measurement is enhanced by the time expansion technique [71].

within a maximum delay. On the other hand, the history buffer is active even after the FT arrival, and keeps track of front pairs corresponding to the crossings of the HT [71].

In order to improve the time resolution, we used the *time expansion* technique: during the time elapsed between the passing of the LT and the arrival of the FT (in figure 3.3, time 4-3) a capacitor is charged linearly, upon the FT arrival, it starts discharging linearly on a circuit with a longer characteristic time (M = 25 $\div$ 30, in figure 3.3 time 31). If the intrinsic TDC resolution is σ_{TDC} and the fluctuations on M are negligible, the final time resolution after the time expansion is $\sigma \approx \sigma_{TDC}/M$. Any instability of the time expansion factor M will result in a

higher σ [71].

Each SFET module has a Charge Measurement Block (CMB) for the anode charge measurement that reads the 4 input channels, because of the CMB is common to all the front-end boards it will be explained only once in next section. The SFET boards are located inside the S-crate and are connected to the SDR by Back Plane connectors. To acquire the data from all the anodes of the TOF are necessary 16 SFETs and 4 SFEAs.

3.1.2 The SFEA2 boards

The SFEA2 board [71] consist of two (primary/secondary) identical SFEA modules for redundancy. Each module reads four ACC anodes and two TOF anodes. The TOF channels are identical to the SFET module. The ACC analog signals are split in two parts: the lower fraction goes to an amplifier and then to the CMB used to measure the released charge collected by the ACC and TOF channels, whereas the higher one is compared to one threshold only (instead of LT, HT and SHT). If the pulse passes the threshold, the TDC history buffer keeps track of the crossing time and a logical signal is sent to the trigger board for the trigger veto. An other difference with the SFET is that there is no time-expansion buffer for ACC channels. Also the SFEA boards, like the SFETs, are located inside the S-crate, one SFEA for each S-crate.

3.1.3 The SFEC boards

The SFEC board (shown in figure 3.4) has the goal to measure the charge collected by the dynodes of the TOF PMTs. This board is not doubly redundant because of the dynodes are read singly and this imply a signal redundancy from each counter, and because it is lodged directly on the detector and for this reason, it has to be small. In each TOF plane are located, close to the PMTs, two SFECs that read all the photomultipliers; each SFEC receives the signals from twenty dynodes via coaxial cables,soldered directly on the board. The SFECs are connected to the SDR board by twisted pair cables carrying both differential LVDS digital data and low voltage power. The SFEC board is composed by the charge measurement block that will be explained in next section.

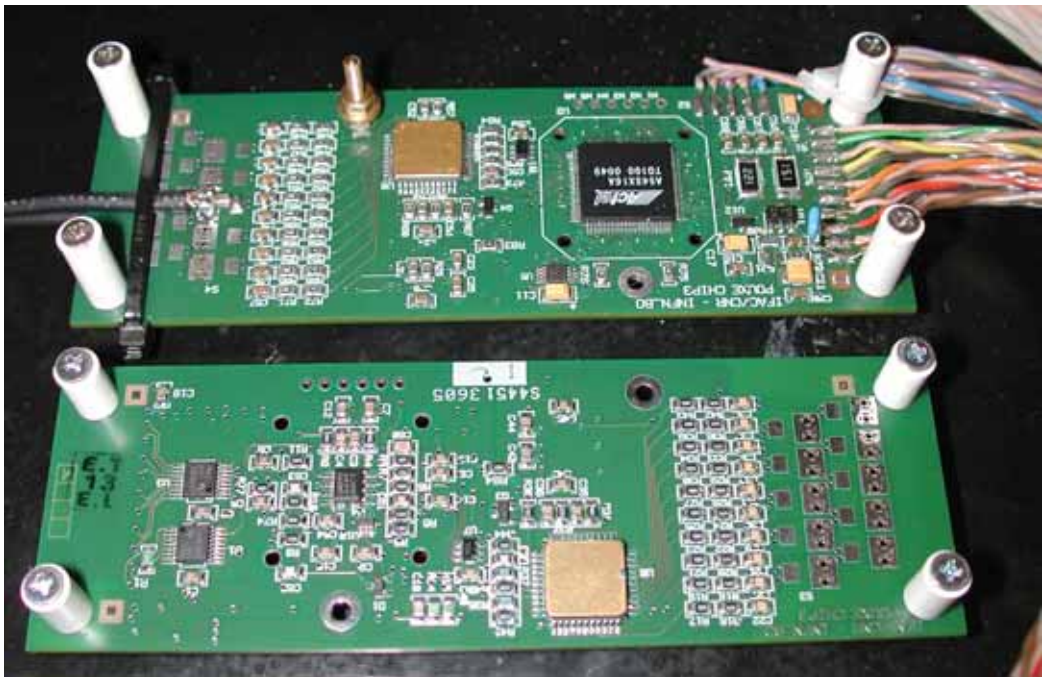

Figure 3.4: The two sides of the SFEC board. On the top is shown the side with the FPGA, one AICPPP chip, one ADC and the powering and digital connections. On the bottom is shown the other side (of another SFEC) with a AICPPP chip and the other ADC.

3.2 The Charge Measurement Block

The anode and dynode signals coming from the TOF PMTs, produced when a charged particle crosses a scintillation counter, are short current pulses of $10 \div 20$ ns, read on a 50Ω resistor.

The time-integrated current pulse represents the charge collected by the FE electronics, that is proportional to the number of photons produced in the scintillator by the ionization losses of the charged particle, and for this reason is a function of the ion charge and velocity.

In order to measure this collected charge, the pulse is sent to a preamplifier and to a shaper analog integrated circuit (AICPPP chip or FE chip), that transforms the few tens of ns long pulse into a much longer pulse ($\sim 1\mu s$), whose maximum voltage is proportional to the integrated charge. A *sample-and-hold* technique is

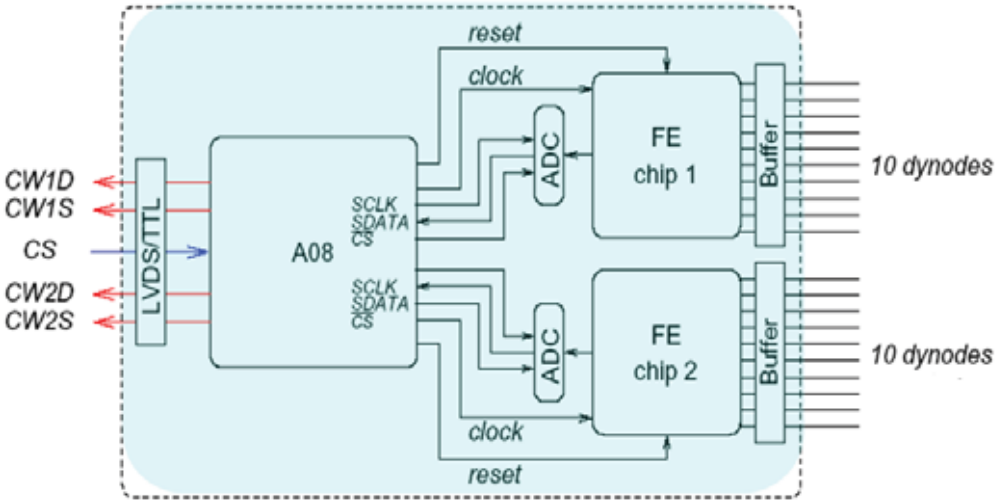

Figure 3.5: Block scheme of the charge measurement block prototype for dynodes [71]. The CMB for dynodes is composed by an FPGA (A08), two AICPPP chips and two ADCs, it transmits the data from twenty dynodes to the SDR board by LVDS links. The CMB for anodes has an FPGA (A08) that controls only one FE chip for negative signal.

then used to keep memory of this maximum voltage (reached roughly 2 μs after the input pulse), which is sent to a linear ADC (Analog Device AD7476) for the digitization. Finally the digital data are sent to the SDR2 board via serial links.

Two prototype of the charge measurement blocks were produced, to measure anode (negative) and dynode (positive) signal. The one for the dynodes (see figure 3.5) is composed by an FPGA (Field Programmable Gate Array), model Actel A08, two AICPPP chip, wich read the signals in parallel from ten dynodes, and two ADCs, each one connected to the output of a front-end chip. The prototype for anodes is composed by one FPGA, only one FE chip (instead of 2), that reads the signals from 4 anodes, and only one ADC. The difference between the two kinds of prototypes stays on: the number of input signals to acquire, this imply the number of FE chip and ADC used, and on the kind of AICPPP chip used, one born to process negative signals, and another one to process the positive ones. The architecture and the functionalities of the two kinds of chip, are completely the same.

3.3 The AICPPP integrated circuit for PMT pulses processing

The necessity to acquire a great number of anode and dynode signals suggests the use also for the TOF, of an integrated circuit already developed by the collaboration for the RICH sub-detector for a similar purpose [72], [73], [74]: the AICPPP chip (see figure 3.6).

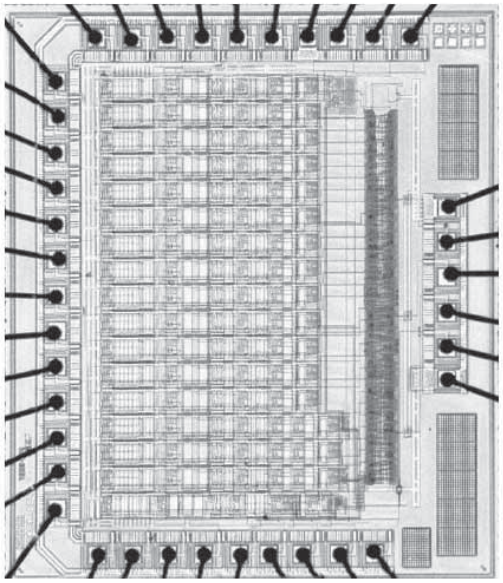

Figure 3.6: Picture of the chip AICPPP [72], [73], [74].

The AICPPP integrated circuit has to operate in space environment, which imposes some constraints: radiation hardness, low power consumption, and very compact front-end electronics; for that reasons has been designed a dedicated integrated circuit for the front-end signals processing. There are two different prototypes of this chip, one that processes the anode signals (negative signals) and another one for dynodes (positive signals). The architecture and the functionalities of the two chip prototypes are equal.

The AICPPP chip has an architecture based on a spectrometry chain. This method gives a voltage signal proportional to the charge of the input pulse. The circuit can integrate up to 16 identical channels at the same time. The analog

output of each channel is memorized into the track-and-hold circuit and the 16 outputs are read sequentially via a multiplexer in order to reduce the number of input/output pads (figure 3.7 shows the architecture of the complete circuit[2]). In order to increase the resolution for small signals, an amplifier with a $5\times$ gain has been added at the output. The amplifier with unit gain ensures a large dynamic range with a minimum distortion (see next chapter for more details).

In order to minimize the number of input pads, the logic control has only one clock input signal. The spectrometry chain is composed of a charge integrator followed by a first-order high-pass filter with a pole-zero cancelation, followed by a 5th order low pass filter (figure 3.8). The result is a quasi gaussian shaped pulse. The time constant of the circuit (around 200 ns) is large enough so that it is easy to sample the signal on its maximum (about 1.7 μs after the anode/dynode signal, i.e. about 1.6 μs after the fast trigger signal). The peak amplitude is directly proportional to the total charge. Our measure results show that a time shift of 100 ns on the hold pulse edge leads to an error on the peak amplitude of only 0.005%, as will be shown in chapter 5.

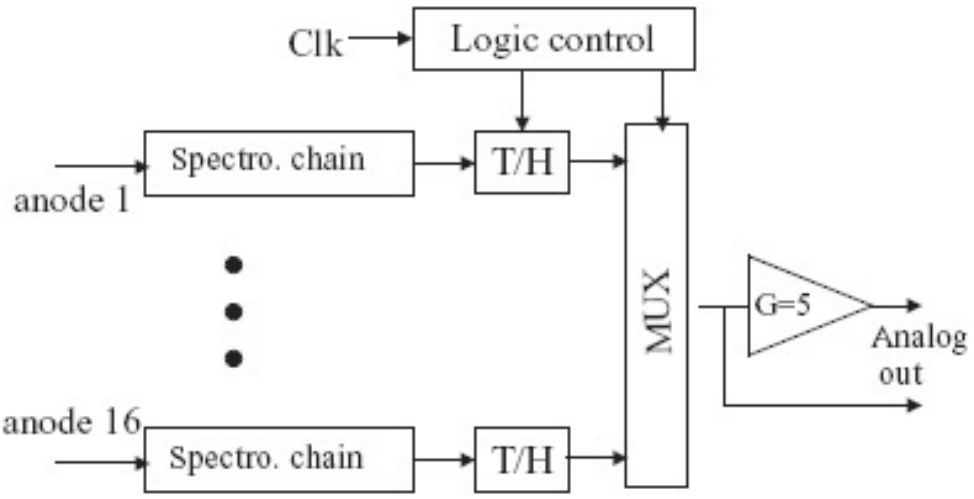

Figure 3.7: Circuit architecture [72], [73], [74].

The analog output waveform of the circuit is composed of 32 voltage steps, each step value corresponds to the maximum amplitude of one channel: 16 steps

[2]To simplify, all the figures represent only the anode signal in input to the chip. For a dynode signal it would be completely the same.

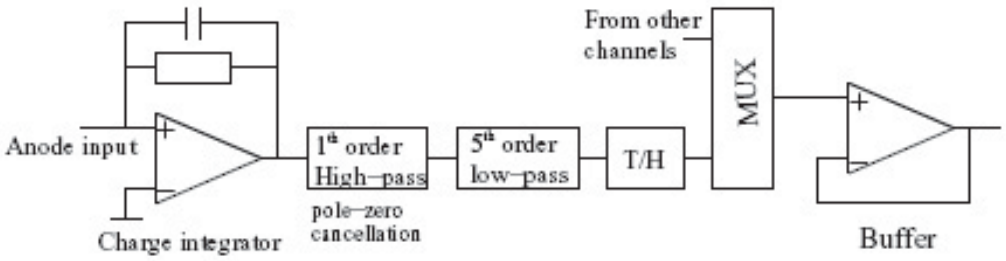

Figure 3.8: One channel architecture [72], [73], [74].

for the gain $\times 1$ followed by 16 steps for the gain $\times 5$ output. An example of output signal shape coming from the multiplexer output is given in figure 3.9. The first clock pulse gives the trigger to the chip. The second clock pulse holds the 16 analog values, and the 32 next pulses change the active multiplexer input. The delay of the second pulse must be adjusted to ensure the sampling of the analog pulses at their maximum. The 16 to 1 analog multiplexer is composed of four 4 to 1 multiplexers followed by a 4 to 1 multiplexer in order to reduce the load capacitance on each analog channel: each channel is loaded by only 4 switches in this case instead of 16. There is a 17th channel, the tagging channel that can be useful to give a logic information on the status of the PMT in order to optimize the data acquisition system, but we do not use this functionality.

Figure 3.9 shows the readout sequence of the 16 anode channels in input to the chip. From the top of the figure 3.9: *a)* the schematic view of the PMT signal in input to one of the 16 channels; *b)* the signal in output from the 5^{th} order filter, it is a quasi gaussian shape pulse directly proportional to the total charge; *c)* the track and hold output signal freezes the peak values of the 16 channels; *d)* an example of the 16 analog channels in the serial output of the chip, each peak representing the voltage value kept at the moment of the track and hold; *e)* the input clock to the chip, labeled *CLK*. The *CLK* comprises:

- a *Trigger* pulse to initiate the sequence in the logic module,
- a *Hold* pulse to memorize the peak of the shaper pulse,
- 32 pulses to control the multiplexer where the multiplexing frequency is limited to 1.5 MHz,
- a 33^{rd} to turn the output of the chip into high impedance state.

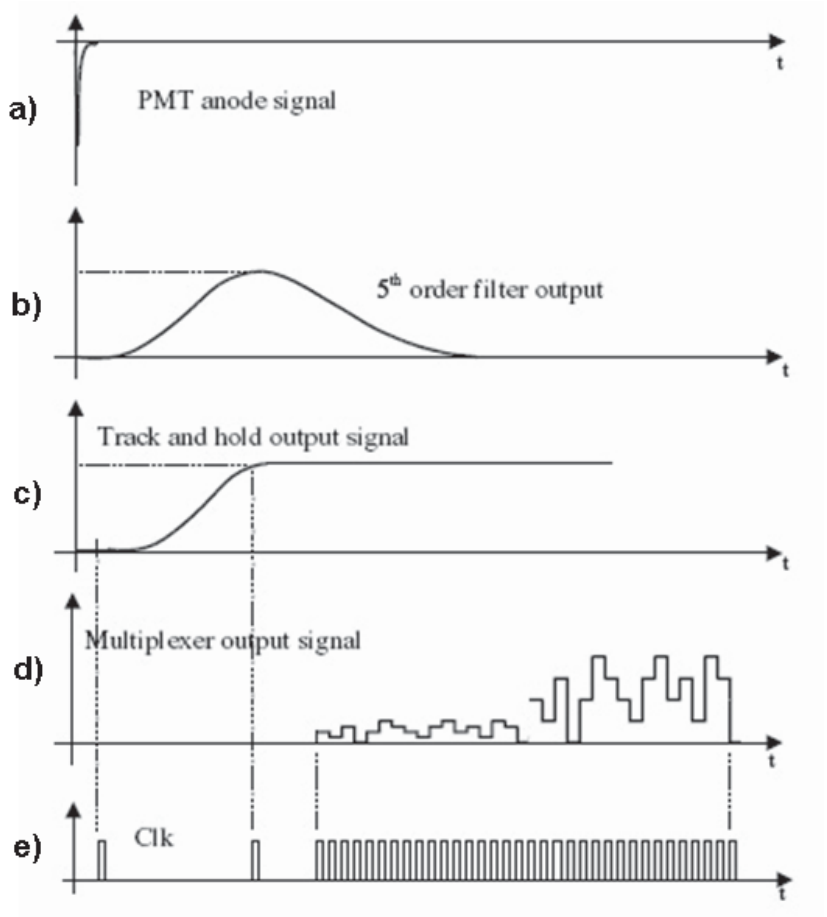

Figure 3.9: Circuit chronograms of the AICPPP chip [72], [73], [74].

It is possible to read less than 32 channels: it is enough to reduce the number of clock pulses to the multiplexer and to give a reset pulse to the chip at the end of acquisition, to restart the multiplexer from the first channel (more details on the reset procedure will be explained in chapter 5).

3.4 The analog to digital converter

The serial output of each AICPPP chip is connected to the input of the serial ADC AD7476 [75]. The AD7476 is a 12 bits, high speed, low power, successive-approximation ADC. It can operate from +2.35 V to +5.25 V power supply; the ADCs on the CMB block is powered at +3.3 V (figure 3.10). It contains a low noise, wide bandwidth track-and-hold amplifier that can handle input frequencies

in excess of 6 MHz. The AD7476 uses advanced design techniques to achieve very low power dissipation at high throughput rates. The analog input range is 0 V to +3.3 V. An external reference is not required for the ADC, because the reference for the AD7476 is derived from the power supply, to get the widest dynamic input range [75].

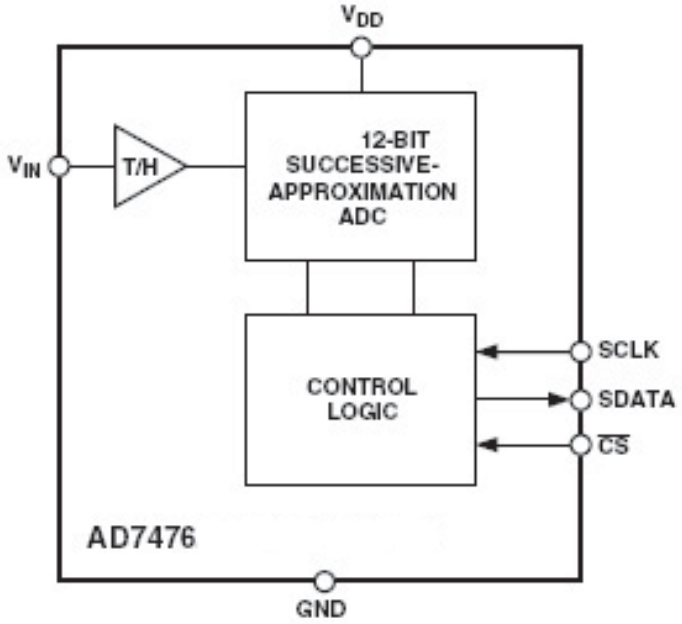

Figure 3.10: ADC AD7476 [75].

There are two possible modes of operation, *normal mode* and *power-down mode*. These modes of operation are designed to provide flexible power management options. These options can be chosen to optimize the power dissipation/throughput rate ratio for different application requirements. The mode of operation of the AD7476 is selected by controlling the logic state of the chip select (CS) signal during a conversion. The ADCs on the CMB work on normal mode, to obtain the fastest throughput rate performance. Figure 3.11 shows the general diagram of the operation of the AD7476 in normal mode. The conversion process and data acquisition are controlled using CS and the serial clock SCLK, that has a period of 80 ns. The input signal is sampled on the falling edge of CS and the conversion is also initiated at this point. There are no pipeline delays associated

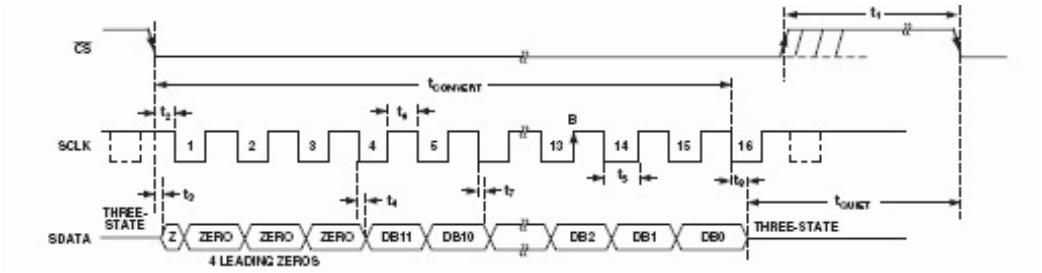

Figure 3.11: AD7476 serial interface timing diagram [75].

with the part. The CS signal initiates the data transfer and conversion process. The falling edge of CS puts the track-and-hold into *hold mode*, takes the bus out of three-state, and samples the analog input. The conversion is also initiated at this point and will require sixteenth SCLK cycles to complete.

To ensure the part remains fully powered up at all times, CS must remain low until at least 10 SCLK falling edges have elapsed after the falling edge of CS. If CS is brought high any time after the tenth SCLK falling edge, but before the sixteenth SCLK falling edge, the part will remain powered up but the conversion will be terminated and the output will go back into three-state. Sixteen serial clock cycles are required to complete the conversion and access the complete conversion result. The conversion result is output in a 16 bits word with four leading zeros followed by the most significant bit (MSB) of the 12 bits word. The final bit in the data transfer is valid on the sixteenth falling edge, having been clocked out on the previous (fifteenth) falling edge. CS may idle high until the next conversion. Once a data transfer is complete (the output has returned to three-state), another conversion can be initiated after the quiet time, tQUIET (50 ns), has elapsed by again bringing CS low.

The power-up time of the AD7476 is typically 1 μs.

3.5 The FPGA control logic

The FPGA control logic is the A54SX08A-TQ100. This device is necessary to control the front-end AICPPP chips mounted on the CMB block and to control the ADCs necessary to digitalize the output signals from the front-end chips.

The Actels SX-A family of FPGAs features a sea-of-modules architecture that

delivers device performance and integration levels [76]. Actels SX-A architecture features two types of logic modules, the combinatorial cell (C-cell) and the register cell (R-cell), each optimized for fast and efficient mapping of synthesized logic functions. The routing and interconnect resources are in the metal layers above the logic modules, providing optimal use of silicon. This enables the entire floor of the device to be spanned with an uninterrupted grid of fine-grained, synthesis-friendly logic modules (or *sea-of-modules*), which reduces the distance signals have to travel between logic modules. To minimize signal propagation delay, SX-A devices employ both local and general routing resources. The high-speed local routing resources (*direct connect* and *fast connect*) enable very fast local signal propagation that is optimal for fast counters, state machines, and data-path logic. The general system of segmented routing tracks allows any logic module in the array to be connected to any other logic or I/O module. Within this system, propagation delay is minimized by limiting the number of anti-fuse interconnect elements to five (90% of connections typically use only three or fewer anti-fuses). Further complementing SX-As flexible routing structure is a hard-wired, constantly loaded clock network that has been tuned to provide fast clock propagation with minimal clock skew.

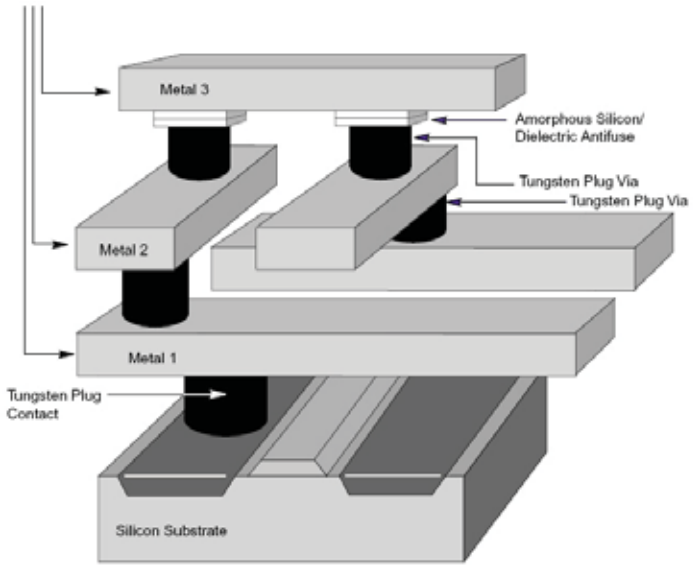

Figure 3.12: Example of a device structure. The A54SX72A has 4 layers of metal with the antifuse between Metal 3 and Metal 4 [76].

Interconnection between these logic modules is achieved using Actels patented metal-to-metal programmable anti-fuse interconnect elements. The anti-fuses are normally open circuit and, when programmed, form a permanent low-impedance connection. The R-cell contains a flip-flop featuring asynchronous clear, asyn-

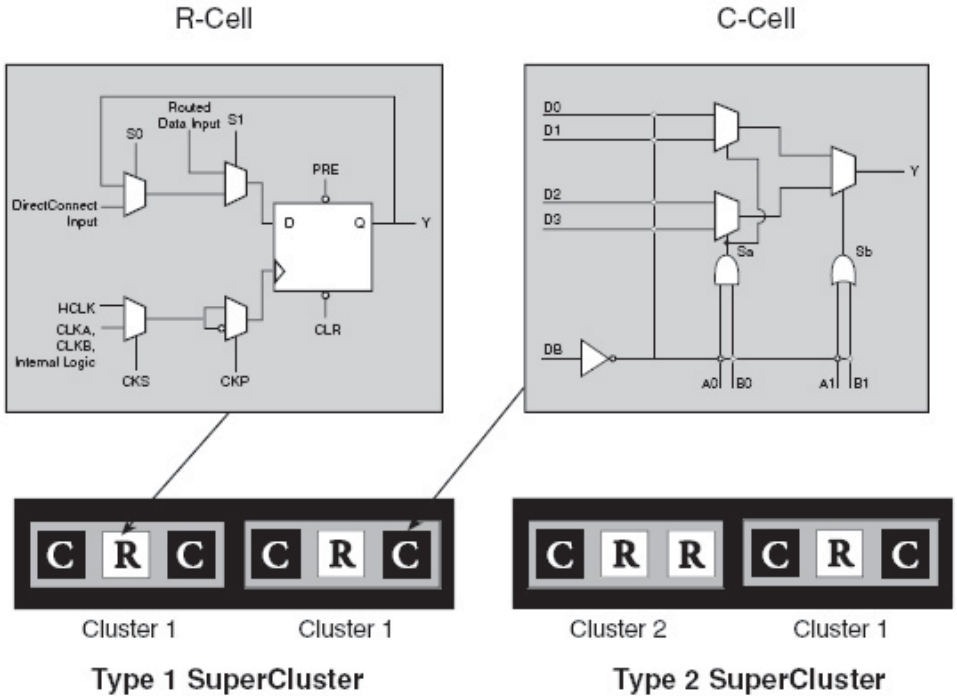

Figure 3.13: Super-cluster organization of the FPGA Actel: the C are the C-cells, with R the R-cells [76].

chronous preset, and clock enable (using the S0 and S1 lines) control signals (figure 3.13). The clock source for the R-cell can be chosen from either the hard-wired clock, the routed clocks, or internal logic. The C-cell implements a range of combinatorial functions up to 5 inputs (see figure 3.13). Actel has arranged all C-cell and R-cell logic modules into horizontal banks called Clusters. There are two types of Clusters: Type 1 contains two C-cells and one R-cell, while Type 2 contains one C-cell and two R-cells. To increase design efficiency and device performance, Actel has further organized these modules into Super-Clusters. Super-Cluster 1 is a two-wide grouping of Type 1 clusters. Super-Cluster 2 is a

two-wide group containing one Type 1 cluster and one Type 2 cluster (see figure 3.13). SX-A devices feature more Super-Cluster 1 modules than Super-Cluster 2 modules because designers typically require significantly more combinatorial logic than flip-flops.

Direct Connect is a horizontal routing resource that provides connections from a C-cell to its neighboring R-cell in a given Super-Cluster. Direct Connect uses a hard-wired signal path requiring no programmable interconnection to achieve its fast signal propagation time of less than 0.1 ns. Fast Connect enables horizontal routing between any two logic modules within a given Super-Cluster and vertical routing with the Super-Cluster immediately below it. Only one programmable connection is used in a Fast Connect path, delivering a maximum pin-to-pin propagation time of 0.3 ns. In addition to Direct Connect and Fast Connect, the architecture makes use of two globally oriented routing resources known as segmented routing and high-drive routing.

Actels high-drive routing structure provides three clock networks. The first clock, called HCLK, is hardwired from the HCLK buffer to the clock select MUX in each R-cell. HCLK cannot be connected to combinational logic. This provides a fast propagation path for the clock signal, enabling the 3.8 ns clock-to-out (pad-to-pad) performance of the SX-A devices. The hard-wired clock is tuned to provide clock skew less than 0.3 ns worst case. The remaining two clocks (CLKA, CLKB) are global clocks that can be source from external pins or from internal logic signals within the SX-A device. CLKA and CLKB may be connected to sequential cells or to combinational logic. We used the HCLK for the input clock to the FPGA on the CMB, while CLKA for the input to the *time-out reset* circuit, that will be explained in chapter 4.

Actels SX-A family [76] is implemented on a high-voltage twin-well CMOS process using $0.22/0.25$ design rules. The metal-to-metal anti-fuse is made up of a combination of amorphous silicon and dielectric material with barrier metals and has a programmed (*on* state) resistance of 25 Ω with capacitance of 1.0 fF for low signal impedance.

Each I/O on an SX-A device can be configured as an input, an output, a tristate output, or a bidirectional pin.

3.6 Data Strobe communication

The CMB blocks from all the front-end boards send all the anodes and dynodes data to the SDR2 board, using the *Data-Strobe* (DS) protocol [71].

In the DS protocol, the data line carries binary data values, and the accompanying strobe line changes state each time the next bit has the same value as the previous one[3]. By this means each DS pair carries a clock encoded in the logic XOR of the signals, in a way that allows up to a full bit-time of skew-tolerance between the two connections. Figure 3.14 shows the form of signals on the data and strobe connections.

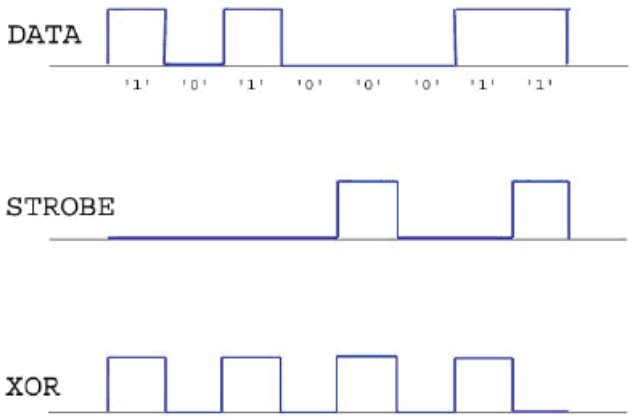

Figure 3.14: Example of transmission of the binary number **10100011** with data and strobe. It's shown also the logic **XOR** of data and strobe that gives a clock.

Since the data-strobe system carries a clock, the links are asynchronous; the receiving device synchronizes the incoming data, the only restriction being the transmission rate does not exceed the maximum speed of the receiver. This also simplifies clock distribution within a system, since the exact phase or frequency of the clock on a pair of communicating devices is not critical. Furthermore a single link can operate at different speed if necessary.

[3]This does not correspond with the usual meaning of *strobe* which would be a signal that indicates every time that another signal is valid.

Inside the CMB block each data value is digitalized by the ADC in a 16 bits word, the first four bits are zero and are discarded, the next 12 bits are the real data value. The 12 bits word is transmitted via data strobe communication from the least to the most significant bit without any parity check or bit error.

3.7 Powering and connections

The CMB is powered by +3 V and -2 V lines dedicated to the AICPPP chip [70]. These lines are obtained from the $\pm$5.0 V lines coming from SPT2 board in the case of the SFEC, and coming from the back plane in the case of the SFET2 and SFEA2. The ADC on the CMB, is powered by $+$3.3 V, while the FPGA device is powered with +3.3 V and +2.5 V. The +2.5 V line is obtained from +3.3 V using the HV regulator ADP3336 inside the CMB (the +3.3 V and +2.5 V lines are also used for the reset circuit that will be described on the next chapter).

Figure 3.15: The SFEC board is powered by the five connections on the top of the figure: ground, -5V, +3.3, ground and +5V. We can see on the right all the LVDS links, that are: two for the input clock, two for the data of the first chip and two for the strobe, two for the data of the second chip and two for the strobe.

In the case of the SFEC, multiwire cable carries twisted pairs are used for the digital communication and for low-voltage power lines. In figure 3.15 is shown

a detail of the board, we can see on the top the five lines connected respectively from the left to the right, to the: ground, -5V, +3.3, ground and +5V; on the right of the figure are shown all the LVDS links: two dedicated to the input clock, two relative to the data and two to the strobe of the first chip and finally two relative to the data and two to the strobe of the second chip. All these cables are soldered to one μD 15-pins connector with the LV and LVDS digital lines. The LVDS is a differential signalling system, which transmits two different voltages which are compared at the receiver. The transmitter on the SFEC is the SN65LVDS391PW and the receiver is the SN65LVDS390PW, both powered by +3.3 V. These devices can transmit 630 Mbit/s with a total power dissipation operating of 35 mW at 200 MHz. The transmitter injects a small current into one wire or the other, depending on the logic level to be sent. The current passes through a resistor of 110 ohms (matched to the characteristic impedance of the cable) at the receiving end, then returns in the opposite direction along the other wire. The small amplitude of the signal and the tight electric-field and magnetic-field coupling between the two wires reduces the amount of radiated electromagnetic noise. LVDS is currently the only scheme that combines low power dissipation with high speed. LVDS is often used for serial data transmission, which involves sending data bit-by-bit down a single wire.

In the case of the SFET2 and SFEA2 boards the signals are transmitted to the SDR2 through serial TTL links, routed on the back plane.

Chapter 4

Development of the SFEC

The final version of the SFEC, that will be installed on the TOF detector, has been obtained after several tests on preliminary prototypes. In this chapter will be presented the prototypes used to obtain the flight version of the SFEC, and the final version of the code on the FPGA on the SFEC, written in VHDL by *Libero* software and simulated by *Model Sim*. Then the Data Acquisition System (DAQ) and the laboratory set-up used to test it are described.

4.1 The CMB prototypes

In October 2003 we developed the first prototype of the Charge Measurement Block, shown in the figure 4.1. This prototype was composed of one AICPPP chip and one ADC for digitalization. The FPGA has not yet been placed on the CMB, but has been lodged on a testing board. The six pins on the left side of the figure 4.1 were connected to the power supply: two pins linked to +3.3 V, two pins to -2 V and two pins for the ground; the six pins on the right side were related to the signals necessary to control the FE chip and ADC devices (see the next section), and the pins on the top of the figure were the input signals to the chip connected to the photomultipliers.

To test the CMB prototype, we used a laboratory set-up composed ofthe testing board S9007 (shown on figure 4.13), that has a reprogrammable FPGA (mod. Asics). We also used the S9007 to acquire the data from the ADC and to transfer it to a PC for analysis.

First of all, to verify the reading process and the temporization necessary for the analog to digital conversion, we read the ADC with a fixed analog value in the

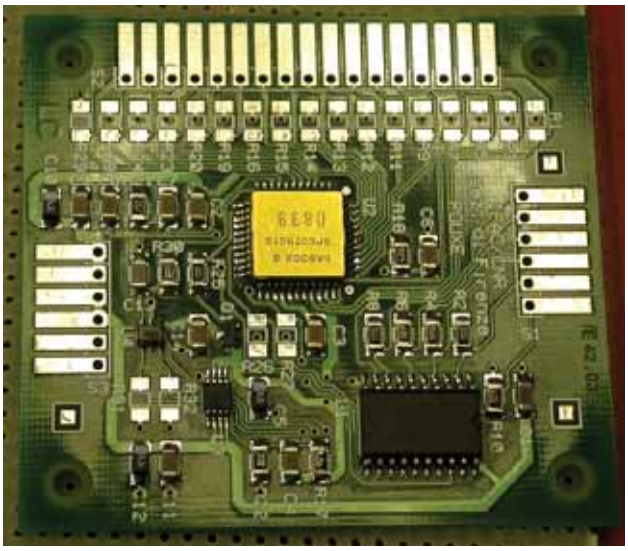

Figure 4.1: The first prototype of CMB composed of: one AICPPP chip and one ADC for digitalization. The six pins on the left side of the figure were connected to the power supply, the six pins on the right side were connected to the signals necessary to control the AICPPP chip and the ADC device, and the pins on the top of the figure were the input signals to the chip connected to the photomultipliers. The FPGA was not yet been place on the CMB but has been lodged on the testing board.

input. Then we acquired the values of the pedestals of the input channels, in order to develop and test the reading logic for the front-end chip acquisition. When the acquisition process was optimized, we focused on the choice of different passive components that connect the anode and the dynode outputs to the AICPPP chip inputs.

Once we defined the timings and the functionalities of the front-end chip and the ADC and we defined the passive components necessary to connect the anodes/dynodes to the FE chip, we developed the second prototype of the CMB, shown in figure 4.2. This prototype was composed of two AICPPP chips, one for the anodes and one for the dynodes, two ADCs and a socket for the unreprogrammable FPGA mod. Actel A54SX08A-TQ100. The socket was important because it allowed us to substitute the FPGA when necessary.

Thanks to this test model, we could translate the FPGA code on the testing

Figure 4.2: The second prototype of the CMB is composed of two AICPPP chips; one for anodes and one for dynodes, two ADCs and a socket with FPGA. The visible button on the board was used to manually reset the FPGA.

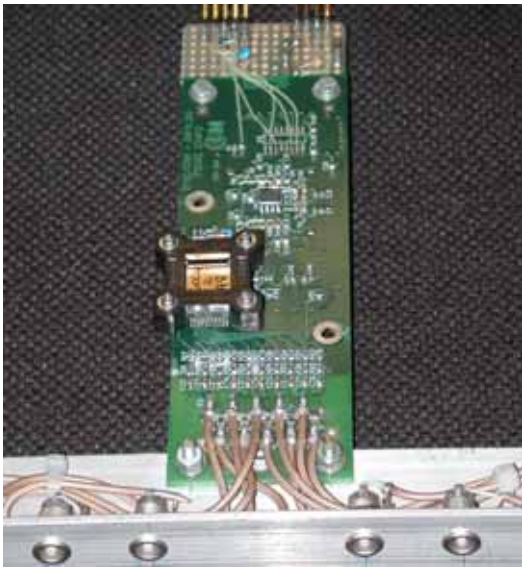

Figure 4.3: The third of the CMB and the first prototype of the SFEC, has a socket for the AICPPP chip in order to test and characterize all chips.

board inside the FPGA on the CMB, and we improved it to acquire data from two chips simultaneously and at faster frequency. Moreover this prototype has been used to define the reset procedure implemented on the third prototype (shown in figure 4.3). This prototype has been also used to match the dynamical range of the dynode and the anode signals in the input to the FE chip.

Figure 4.3 shows the third prototype of the CMB, that can be consider as the first prototype of the SFEC board. This model, improved respect to the second one, is equipped with a socket for the AICPPP chip, which allowed us to substitute the FE chips, in order to characterize all of them.

4.2 The FPGA on the CMB

The FPGA istalled on the CMB, is an un-reprogrammable FPGA Actel model which is radiation-hard. Space environments oblige the use of these kind of devices so that they do not loose their functionalities under hard radiation.

The code on the Actel, was written in VHDL (*Very High Speed Integrated Circuit Hardware Description Language*) using the *Libero* software and was simulated by *Model Sim*.

The code (see appendix A), uses around 50 sequential plus combinatorial cells inside the device, around 5% of the resources of the entire device. Figure 4.4 shows a schematic view of the functionalities of the FPGA. The logics are composed of three main blocks:

- the *AICPPP block* necessary to control the two front-end chips;
- the *ADC block* necessary to generate the signals which control the two ADCs for digitalization;
- the *DATA OUT block* that receives the data from the ADCs, converts them in the *Data-Strobe* protocol (see next section for details) and sends them to the SDR2 board.

Figure 4.4 also shows the FPGA input and output signals:

- *Input Clock* from the SDR2,
- *AICPPP res* to the front-end chips,
- *AICPPP clk* to the front-end chips,

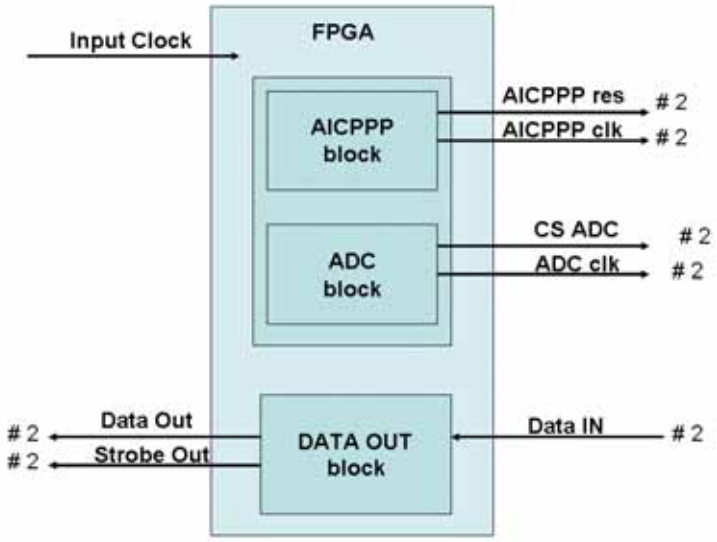

Figure 4.4: Schematic view of the functionalities of the FPGA (Actel) on the CMB, with the *AICPPP block*, *ADC block* and *DATA OUT block*. The input and output signals are also shown, the #2 means that there are two links connected to the FPGA.

- *CS ADC* to the ADCs,
- *ADC clk* to the ADCs,
- *Data IN* from the two front-end chip,
- *Data OUT* to the SDR,
- *Strobe OUT* to the SDR.

In order to reduce power consumption, no clock is installed on board the SFEC. Instead, the FPGA of the CMB is remotely controlled by the SDR2 board. This sends strobes (*Input clock* in figure 4.5) through twisted-pair cables, three meters long, carrying LVDS signals using the data-strobe mode in the case of the SFEC, and via back-plane in the case of the SFET2 and SFEA2. The clock has a fixed number of pulses, necessary to acquire an event, begins after a fast trigger signal.

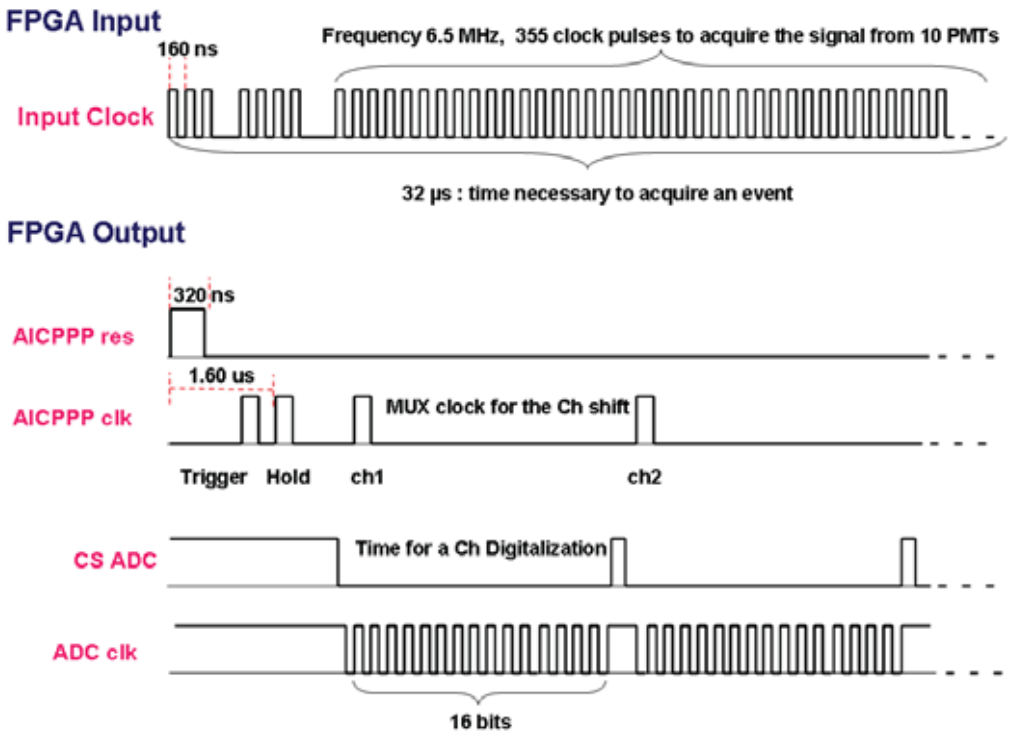

Figure 4.5: The *Input Clock* to the CMB with the signals for the AICPPPs (*AICPPP res*, *AICPPP clk*) and the ADCs control (*CS ADC*, *ADC clk*) that it generates.

The SDR2, at each event, sends the *Input Clock* to the CMBs (see figure 4.5, and appendix 2 for the code on SDR2 FPGA, called *Master*). The first three *Input Clock* pulses are necessary to activate the *AICPPP res* signal that initializes the multiplexer on the first channel. The next bunch of four pulses of the clock generate two hits of the *AICPPP clk*: one that starts the integrator process inside the chip, and the other after a known time of $\sim 1.7\ \mu s$, holds the peak of the integrated signal. Then a series of 355 clock pulses follow at the frequency of 6.25 MHz, necessary for the readout sequence of 10 photomultipliers. These pulses let the FPGA control the multiplexer inside the AICPPP chips, by the *AICPPP clk* signal, and the ADCs by the *CS ADC* and *ADC clk* signals. At the end of the sequence ($32\ \mu s$ after a fast trigger) a *time-out circuit* gives a reset pulse to the FPGA that re-initializes all the digital parts of the CMB.

4.2.1 The Power-up and Time-out circuits for the reset

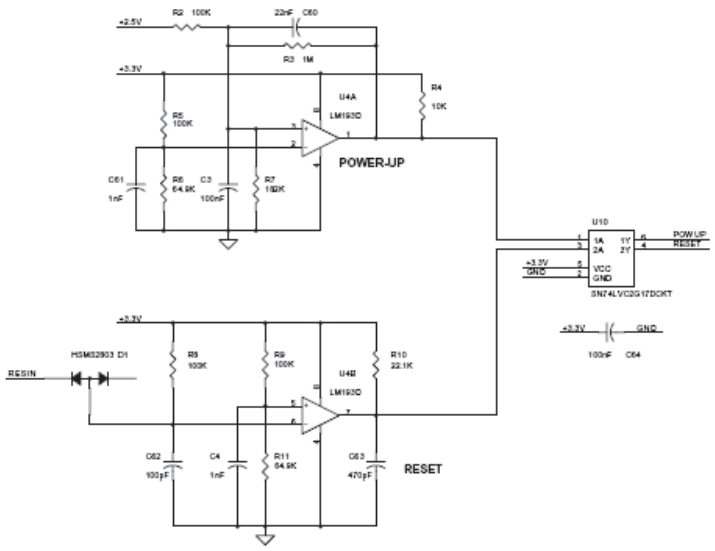

Figure 4.6: *Power-up reset* (on the top) and *time-out reset* circuits (on the bottom) of the CMB on the SFEC, SFET2 and SFEA2 boards.

The reset signal of the FPGA device on the CMB of the SFEC, SFET2 and SFEA2, is very important for the correct functioning of the boards. The reset procedure is controlled by two separate circuits (figure 4.6): the *power-up reset* and the *time-out reset*. The first is active only when the board is switched on. The voltage of the board reaches a steady state, charges a capacitor, the output of the capacitor is amplified and sent to a dual Schmitt trigger, which activates the reset till the capacitor is completely charged ($\sim 5\mu s$). Then the Actel is ready to start acquisition (see figure 4.7).

The other reset circuit, the *time-out reset*, is active at the end of every event acquisition. When the input clock to the CMB FPGA terminates, after each event acquisition, the time-out reset circuit charges a capacitor that after $\sim 3\mu sec$, discharges itself in a dual schmitt trigger that gives a reset pulse to re-initialize the digital parts of the board.

Figure 4.7 shows that the *reset* signal, given by the FPGA to all the digital parts on the CMB of the SFEC, SFET, SFEA, is the result of the logic AND between the *power-on reset* and the *time-out reset*. The *reset* is *ON* at ignition thanks to the

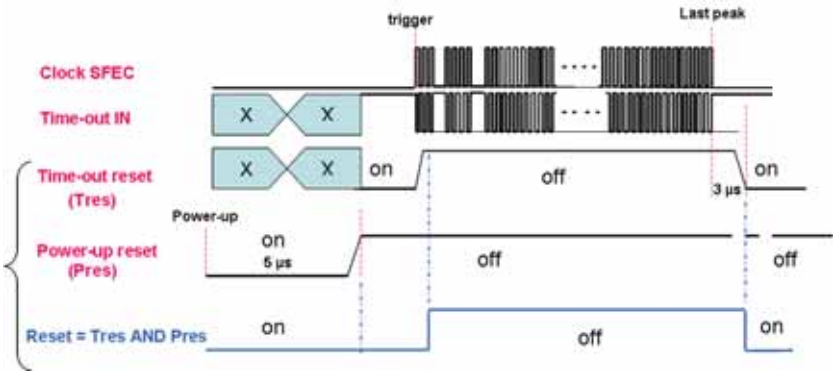

Figure 4.7: The *power-on reset* is active only when the board is switched on, and the *time-out reset* is active at the end of every single event acquisition. The *reset signal* given by the FPGA to all the digital parts on the CMB of SFEC, SFET2 and SFEA2,is the result of the logic AND between the *power-on reset* and the *time-out reset*. The *reset* is *ON* at ignition thanks to the *power-on reset*, and every time the acquisition is finished thanks to the *time-out reset*.

power-on reset, and every time the acquisition is finished thanks to the *time-out reset*.

4.3 Laboratory set up for the tests

The tests on the CMB prototype were done using the following laboratory set-up (figure 4.8):

- a **photomultiplier** connected by an **optical pad** to a **light guide** connected to a **scintillator**, that generates the input signal to the SFEC;
- a **NIM crate** and some modules of standard electronics that, using the PMT signal, generate the trigger for the testing board;
- a **testing board** (CAEN S9007 module) used to simulate the SDR board. It generates the clock signal to the FPGA on the CMB, acquires the data from the CMB and sends it to the serial port of a PC;

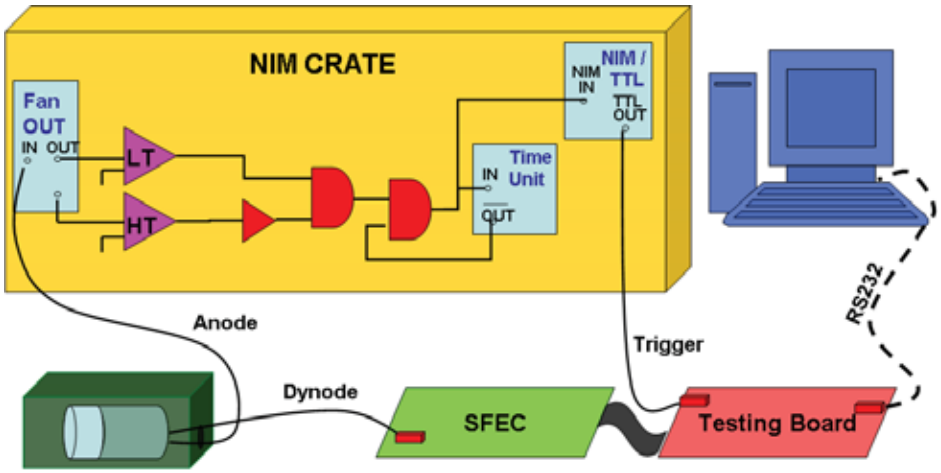

Figure 4.8: A schematic view of the laboratory set-up for the test.

- a **PC** that decodes the data and visualizes it on the terminal, or saves it into files to be analyzed off line.

4.4 The PMT and the scintillator

In Bologna laboratories, in order to calibrate the TOF scintillators, the signals from all the counters were equalized in order to produce the same pulse for MIPs crossing them at the center. This reference signal has a total charge of 50 pC when measured with the anode. We used this information to calibrate the FE chip and the CMB.

In order to calibrate the CMB of the SFET and the SFEA, we used a photomultiplier connected by an optic pad, to a light guide, which was then connected to a small scintillator. Everything was positioned in a black box, as shown in figure 4.9. The scintillator is a piece of plastic scintillator (Eljen-Technology type: EJ-200), of 5×5 cm^2 and 1 cm thick. The PMT, used to do all the tests on CMB, is a Hamamatsu (mod.R5946) RH-ZH5555. The intrinsic characteristics of this PMT from a previous calibration and Hamamatsu data sheets are shown in following table[1]:

[1]Data sheets available at website http: www.hamamatsu.com

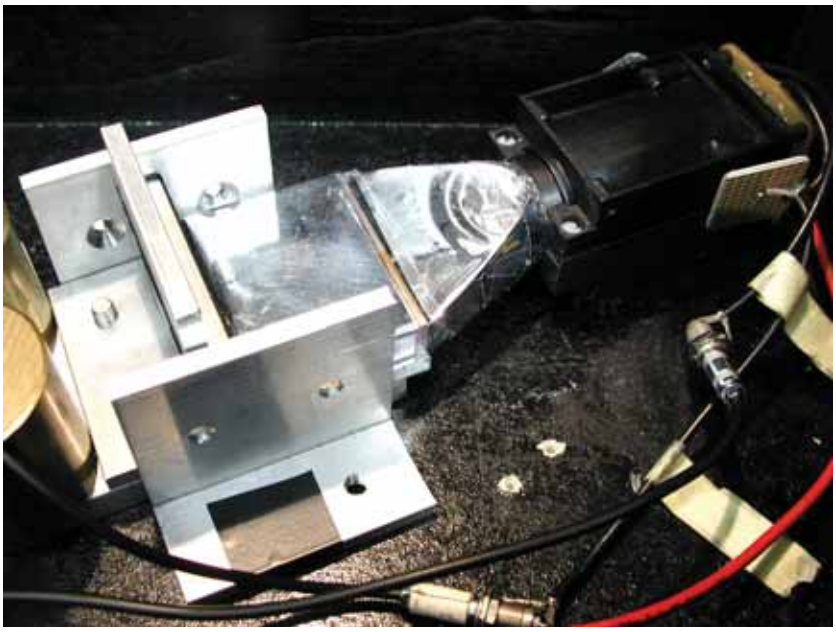

Figure 4.9: A photomultiplier connected, by an optic pad, to a light guide which was then connected to a small scintillator.

Serial number	Nominal gain (2000 V)	Cathode Lum. sens. (μA/lm)	Anode Lum. sens. (A/lm)	Anode dark curr. (nA)	Cathode blu sens. ind.
ZH5555	10.7e+6	91.2	980	7.4	9.88

The PMT gain was tuned, in order to produce an anode pulse for a vertical particle crossing a small scintillator, roughly equivalent to two MIPs. The high voltage (HV) of the PMT was set at about 1440 V. At this HV the signal of the PMT anode measured by an oscilloscope has an area of about 5.3 nVs corresponding to 106.2 pC, as shown in figure 4.10. We connected the anode pulse to the input of the CMB prototype. The CMB distribution is shown in figure 4.11.

Figure 4.12 shows the dynode response for the same event. The area of the signal ($\sim$ 520 pVs) is about 10 times lower than the anode one. The TOF PMTs have an anode/dynode ratio that varies in range from 4 to 11. The ZH5555 PMT

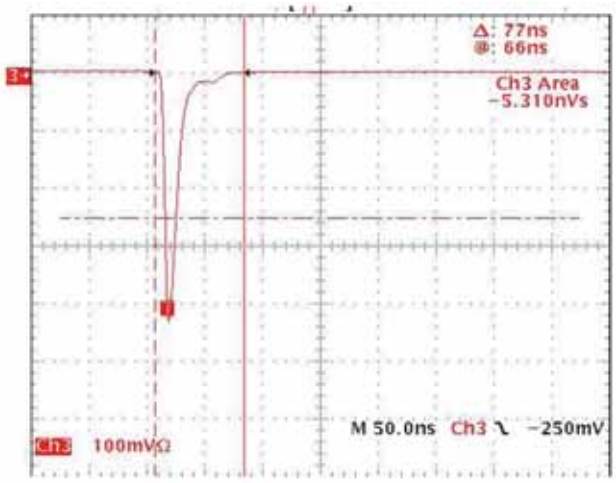

Figure 4.10: Average anode signal produced by CR muons crossing the small scintillation counter.

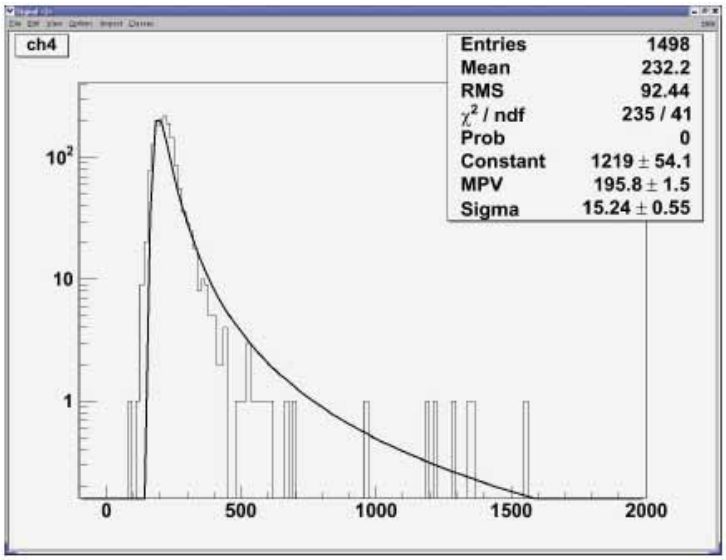

Figure 4.11: The charge distribution from vertical crossing muons measured with the anode of the small scintillation counter.

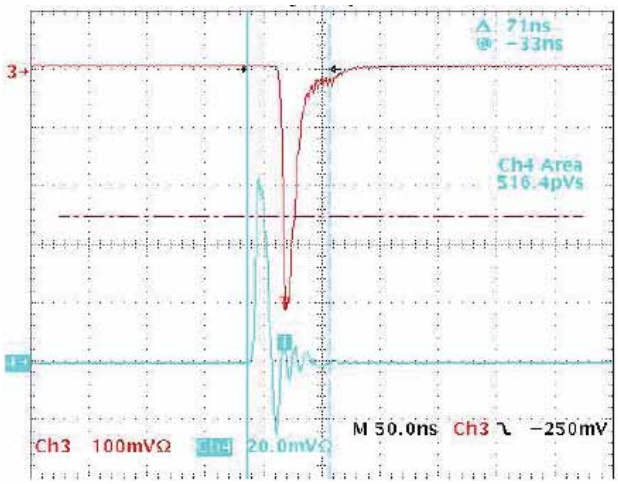

Figure 4.12: An average anode (upper) and dynode (lower) signals by CR muons on the small counter.

has an anode/dynode ratio ≈ 10. Thanks to this characteristic the dynode signal is allowed to reach values of charge at which the anode is saturated.

4.5 The trigger system

When a particle crosses the scintillator it becomes necessary to generate a trigger signal to acquire the event. The trigger signal is generated using the anode pulse of the photomultiplier.

Figure 4.8 shows a schematic view of the set-up to generate the trigger. The anode signal of the PMT is compared to two discriminator thresholds. A trigger pulse is generated only if the released signal from a crossing particle is higher than the threshold of the first discriminator and lower than the second one. In this way the charge lost by the particle on the scintillator is selected and a fast trigger is generated.

Using a *time unit*, the trigger pulse generates a busy signal that enables the trigger until the acquisition is finished.

4.6 The testing board and the PC console

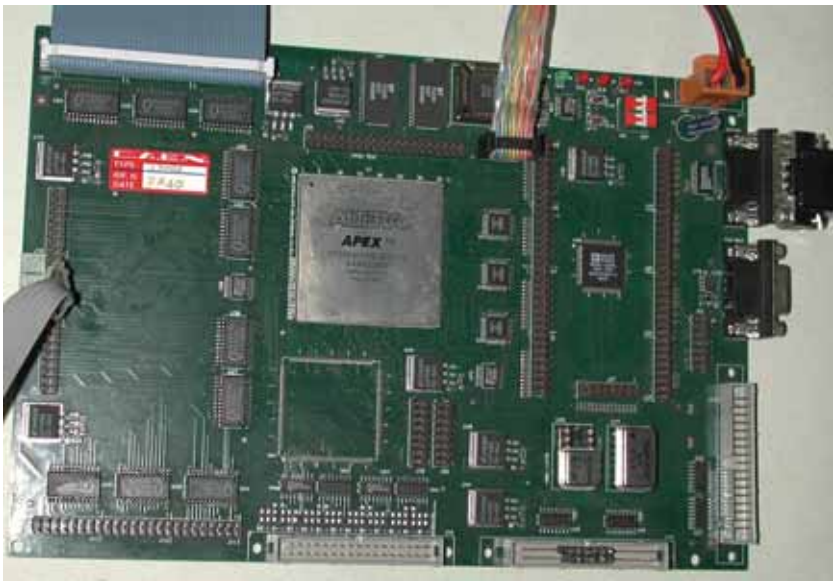

Figure 4.13: A picture of the S9007 testing board.

The testing S9007 board is shown in figure 4.13. It simulates the functions of the SDR2 board. It is composed of an Altera Apex EP20K400EBC652 FPGA, an Analog Device ADSP2187L DSP, drivers with IN/OUT TTL, LVDS, a RS232 port and so on.

The logics on the FPGA is organized in two main blocks (see figure 4.14):

- The **Master** sends the **Clock** signal to the FPGA on board of the CMB when it receives a fast trigger;

- The Data Acquisition System **DAQ** receives the output signals from the FPGA on board of the CMB (**data1**, **strobe1**, **data2** and **strobe2**) and sends serially the data to the PC.

Two versions of the DAQ were developed, the first one created for the first prototype of the CMBs to read only one FE chip, and the second one for the acquisition of two CMBs in parallel.

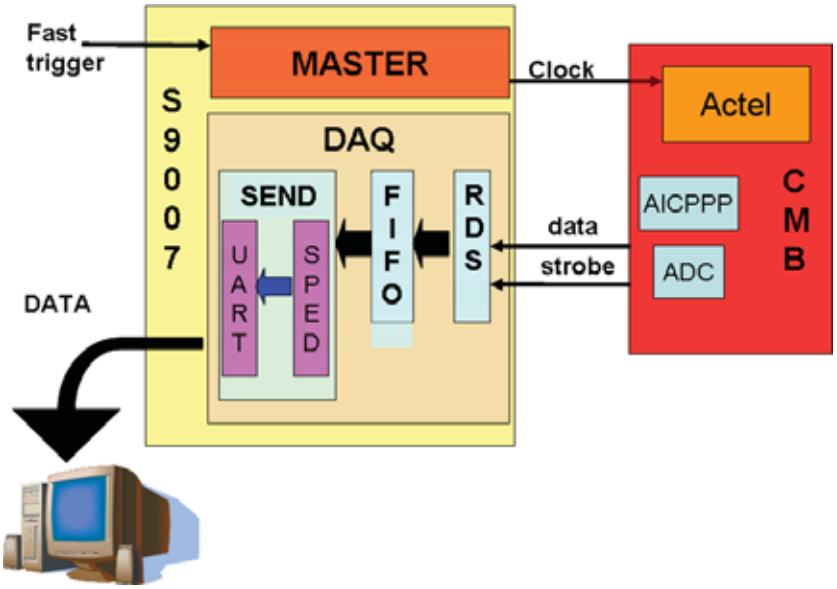

Figure 4.14: Block scheme of the first version of the FPGA logic on the testing board for acquisition from the CMB. The inputs and outputs of the testing board and the connection with the CMB are also shown.

4.6.1 The first version of the DAQ

The DAQ receives the output signals from the CMB (**data** and **strobe**) and sends the data serially to the PC. The DAQ block is composed of three sections (see figure 4.14):

1. The **RDS receiver** (Data-Strobe Receiver) receives the data from the CMB and sends it to the FIFO. It generates the clock from the logic XOR between data and strobe lines and synchronizes it with the internal clock to hold the data input. Then the RDS transfers the decoded data to the FIFO.

2. Because of the acquisition rate is faster than the transfer rate to the PC, it becomes necessary to save the data of each acquisition into a buffer: the **FIFO**. The FIFO can hold 10 words of 12 bits each.

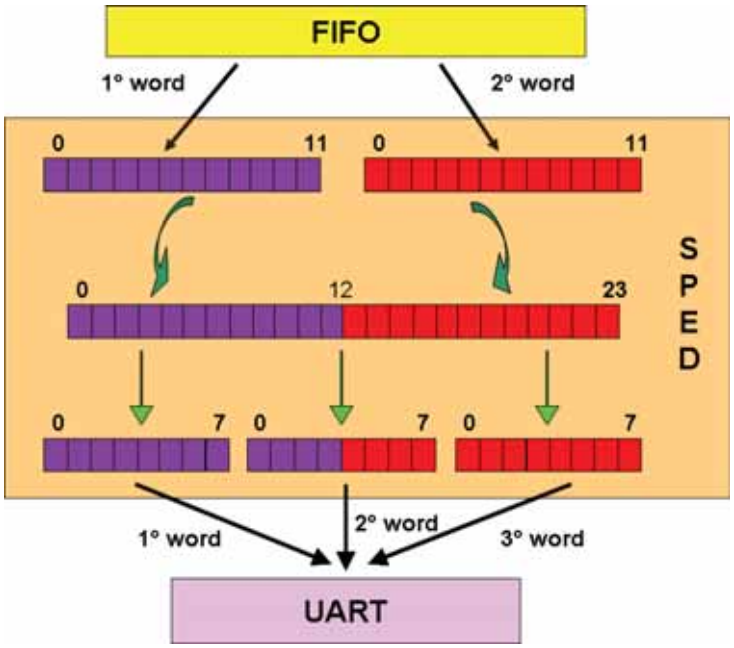

Figure 4.15: The Sped takes from the FIFO two sequential words (of 12 bits each), puts two words together making a word of 24 bits. Then it divides this word in three words of eight bits each to be sent to the PC by the Uart.

3. When the FIFO is full, **Send** takes the data from the FIFO and transfers it to the PC via a RS232 serial link. The Send section is composed of two more parts: Sped and Uart (see figure 4.13).

   When the testing board receives the Fast Trigger (FT), the acquisition starts. **Sped** sends the hexadecimal word ”6F” to the PC by Uart and when the FIFO is full, it takes from the FIFO two sequential words (of 12 bits each), it puts them together, making a word of 24 bits, and then, as shown in figure 4.15, it divides this word in three words of eight bits each to be sent to the PC by the Uart.

   The **Uart** transmits the bytes of data to the serial port of a PC via RS232. As shown in figure 4.16, the RS232 standard transmits the data in bytes. Each byte is preceded by a start bit and followed by a stop bit in order to synchronize the serial receivers. The data byte is always

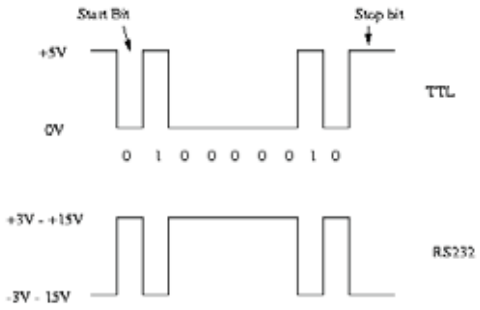

Figure 4.16: The RS232 standard transmits the data in stream of 8 bits. Each byte is preceded by a start bit and followed by a stop bit.

transmitted least-significant-bit first. The bits were transmitted at specific time intervals (104 μs) determined by the baud rate of the serial signal (9600 bd).

4.6.2 The last version of the DAQ

In order to acquire the data from the SFEC boards that have two FE chips, we developed a new DAQ program more efficient, that uses less FPGA resources.

This time the DAQ, as shown in figure 4.17, receives the output signals from the SFEC board, (or from two CMB) **data1**, **strobe1** and **data2**, **strobe2**, and then it sends the serially data to the PC. The DAQ block is composed by three sections:

1. The **RDS** blocks are the data strobe receivers already used in the first version of the DAQ. The only difference with the previous code is that these RDS receivers decode 8 bit words, instead of the 12 bit ones.

2. The **RAM** blocks are two *Quartus RAMs Mega-function* necessary to save 8 bit words from the two RDSs. Each RAM has a *WR-enable* signal that permits us to read or write the RAM at the reading or writing corresponding *address*.

3. The **UART** block transmits the 8 bit data to the PC via the RS232 protocol.

This code is simpler than the previous one, and can be easily modified to acquire many CMBs or SFECs in parallel. For the next thermal-vacuum and vibration test that will be made on the lower TOF (in May 2006), we will modify

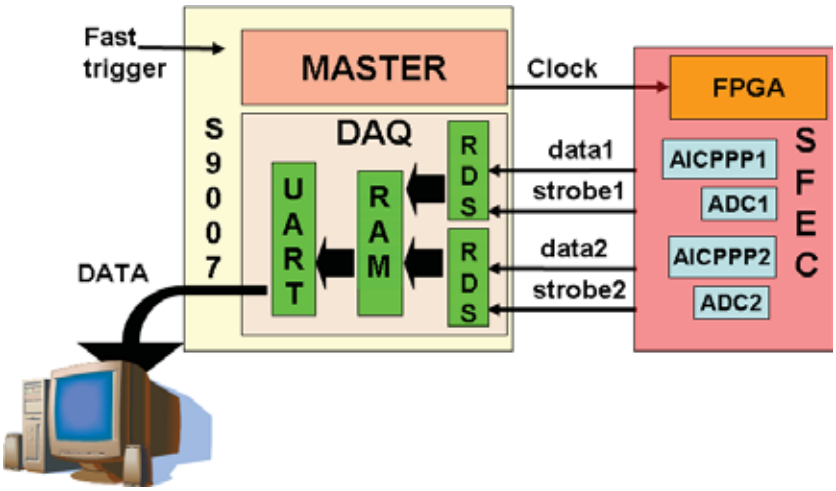

Figure 4.17: Block scheme of the second version of the FPGA on the testing board for the acquisition of the SFEC board. The inputs and outputs of the testing board and the connection with the SFEC are also shown.

once again the DAQ code in order to acquire simultaneously the two flight models of the SFECs, already installed inside the lower TOF detector, and two CMBs for the anode signals.

4.6.3 The PC

The data arrives to the PC by the RS232 serial port. Figure 4.18 shows a screen shot of the Graphical User Interface (GUI) used to acquire the data. The data flow, in hexadecimal words, is displayed on the GUI during an acquisition and it can be stored on files for off-line analysis. To analyze the off-line the data from the CMBs, programs and routines using CERN ROOT libraries have been developed. Figure 4.19 shows some screen shots of the data analyzing programs used.

4.7 The charge injector circuit

At sea level, most detectable cosmic rays are muons. In order to simulate bigger charge CRs, we changed the gain of the PMT, increasing the HV, but this proce-

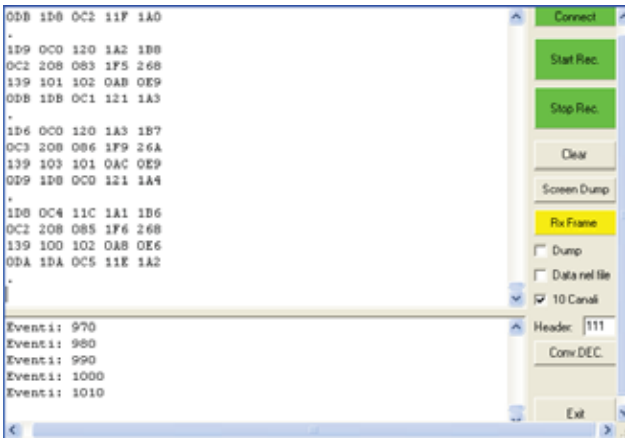

Figure 4.18: The reading of the RS232 serial port by the GUI.

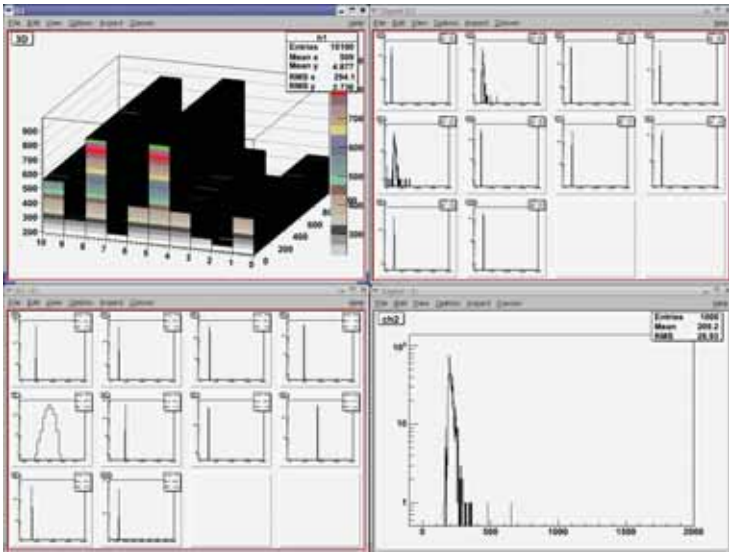

Figure 4.19: Some screen shots of the CERN ROOT routines used for data analysis.

dure also augmented the noise. For this reason, in order to calibrate the CMB with larger ion charges, we built the special circuit that is shown in figure 4.20.

This circuit simulates the anode/dynode signal of a PMT with a very large

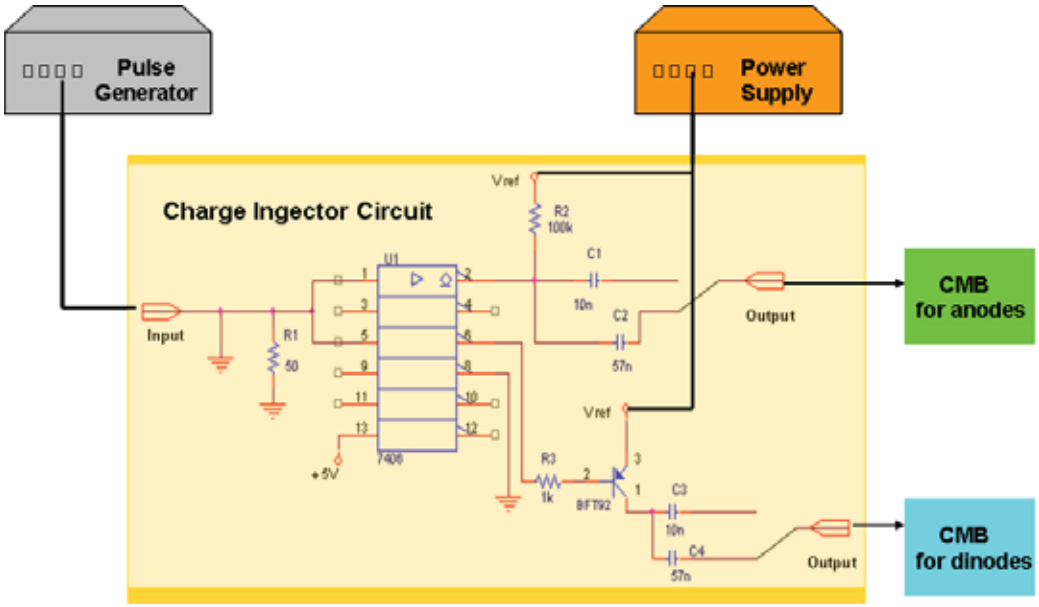

Figure 4.20: The charge injector circuit for the calibration of CMB for the SFET2, SFEA2 and SFEC boards.

dynamic range. Figure 4.21 shows the output signals of the circuit.

The circuit is powered at +5 V. It needs in input a TTL positive pulse of at least 100 nsec, as a trigger, and a positive reference voltage (V_{ref}) to modify the amplitude of the output signal. As shown in figure 4.22, increasing V_{ref} from $\sim 1V$ up to $\sim 14V$, with a capacitor of 57 pF, the output signal changes respectively to ≈ 100 pC up to ≈ 900 pC, i.e. from ~ 2 to ~ 18 MIPs, for the anode signal, while for the dynodes it depends from the A/D ratio.

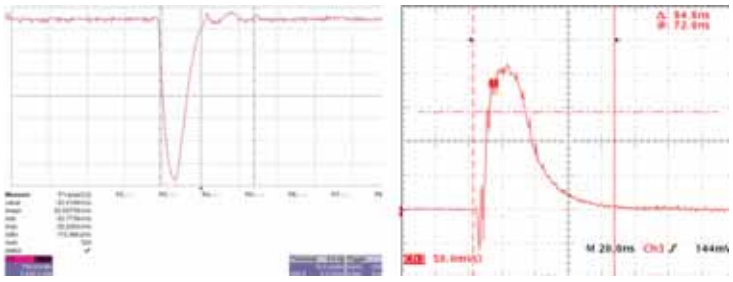

Figure 4.21: The output signal of the circuit that simulates an anode signal (left) and a dynode one (right) from a PMT.

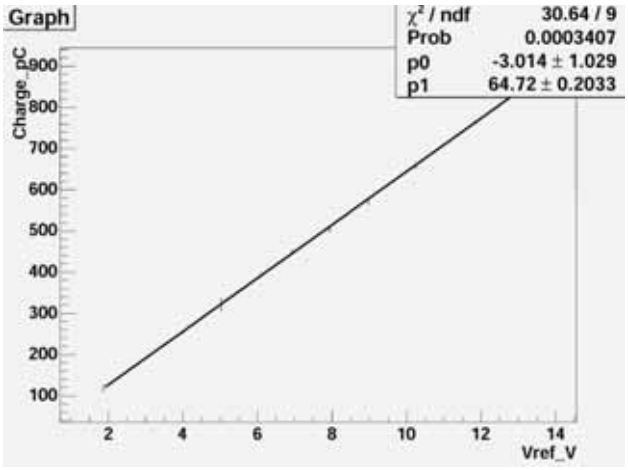

Figure 4.22: V_{ref} in input vs the charge of the signal in output to the circuit.

Chapter 5

The Tests on SFEC

The flight model of the SFEC (shown in figure 3.4 of chapter 3), already installed on the lower TOF subdetector, has been achived after several tests on the SFEC components and on the first prototypes of the board. This chapter will describe the most significant tests on the SFEC, that were delivered to the fight model; for example tests on components, of dynamic range, of temporization, thermal, thermal-vacuum and finally vibration test.

5.1 Space qualified components

Current trends throughout NASA, military and commercial space sectors favor the insertion of commercial off-the-shelf (COTS) technologies for applications [77]. However, taking into account the space environment shown in figure 5.1, for assuring reliable performance in the presence of ionizing particle environments and of total ionizing dose, it becomes necessary to test COTS with apposite *space qualification* procedures.

Ionizing radiation effects in space electronic can be separated into two areas: Total Ionizing Dose (TID) and Single Event Effects (SEE). The two effects are different, as are the requirements and mitigation techniques.

- TID is due to long-term degradation of electronics due to the cumulative energy deposited on to a material. Effects include parametric failures, variations in device parameters such as leakage current, threshold voltage, etc., and functional failures. Significant sources of TID exposure in the environment of space include trapped electrons, trapped protons, and solar flare protons.

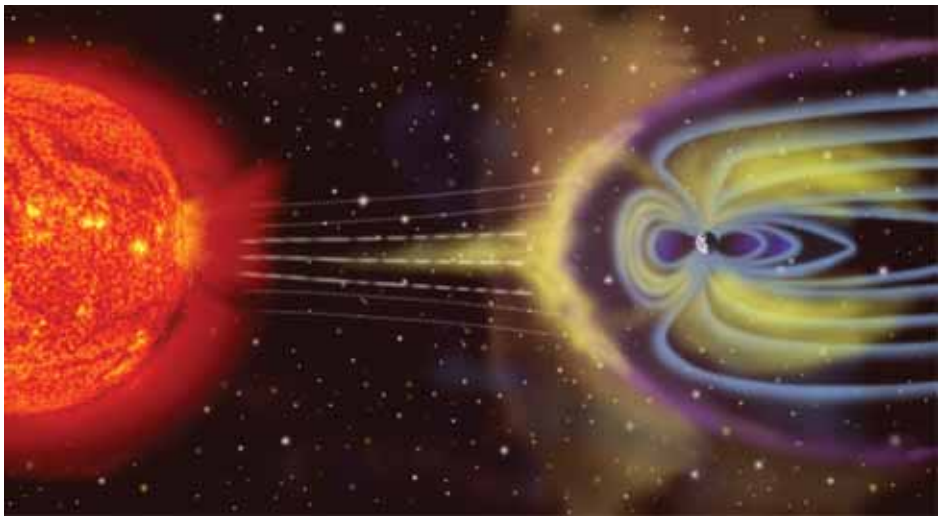

Figure 5.1: The environment of space between Earth and Sun.

- SEEs occur when a single ion strikes the material, depositing sufficient energy into the device to cause a SEE. The multiple types of SEEs may be divided into two main categories: soft errors and hard errors. In general, a soft error occurs when a transient pulse or bit-flip in the device causes an error detectable at the device output, known as Single Event Upset (SEU). A hard error causes a permanent change to the operation of a device or device destruction, examples are SHE (Single Hard Error), SEL (Single Event Latchup) and SEB (Single Event Burnout).

The main sources of energetic particles that contribute to TID and SEE are:

1. protons and electrons trapped in the Van Allen belts,
2. cosmic ray protons and heavy ions,
3. protons and heavy ions from solar flares.

Heavy ions trapped in the magnetosphere do not make a significant contribution to TIDs but have sufficient energy to generate the ionization necessary to cause SEEs. The levels of all of these sources are affected by the activity of the sun. Observations of sunspots over the past two centuries show that the number of sun spots varies with time. The solar cycle averages about 11 years from sunspot

maximum to minimum and back again, with approximately four years of solar minimum and seven years of solar maximum. The last solar maximum occurred in 2000, and the next one is predicted in around 2011. At the time of solar maximum, the number of flares observed increases dramatically.

The radiation dose rate expected during the mission is of about 0.4 krad/year, for this reason all the AMS-02 components have been tested for TDI by the AMS collaboration. These tests were been done at the ENEA-Casaccia in Italy, with the corresponding 100 Rad/year radiation. The tests for the SEE, were done at GSI during the three beam tests explained in the following table [77], [78], [79]:

Date	Location	Ions	LET $(MeV/mg/cm^2)$
Nov'00	GSI	Xe, Au, U	$6 \div 59$
Nov'01	GSI	Kr, Au	$3 \div 40$
May'02	GSI	U	$16 \div 59$

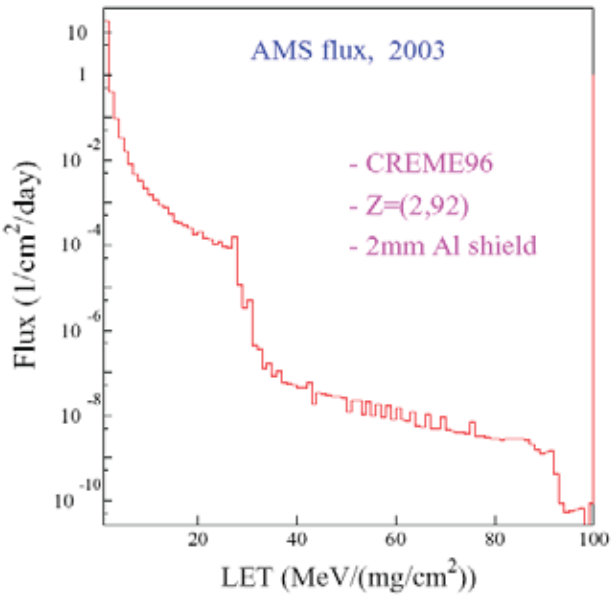

Figure 5.2: Expected fluxes on ISS in 2003 [77], [78], [79].

Figure 5.2 shows the expected value of radiation fluxes on the ISS in 2003. For the AICPPP chip the SEE rates per day expected on ISS are estimated to be: $(4 \pm 1) \times 10^{-8}$ for SEL and $(8 \pm 1) \times 10^{-8}$ for SEU [77], [78], [79].

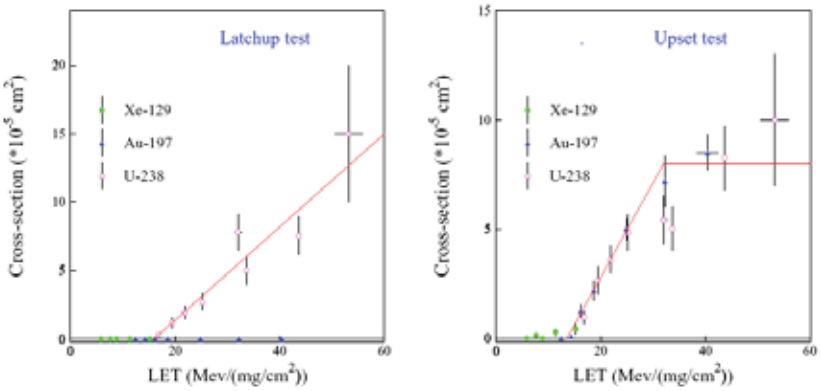

Figure 5.3: SEE rates as measured at GSI for the AICPPP front-end chip [77], [78], [79].

These tests have also been done on the other components, on the ADC and on the FPGA, and the results have been accepted.

5.2 The characterization of the AICPPP chips

The characterization of the AICPPP chips (FE chips) was done using the third prototype of the CMB shown in figure 4.3. This prototype is equipped with a socket for the FE chip, that permits it to characterize all of them. For each chip we measured the pedestal values of the different channels, we monitored the cross talk between close channels, and in addition we determined all the best fit parameters of the calibrations. Then we found the optimal time interval for the sample of the input values that is important to find the dynamic range of the chips.

5.2.1 Measures of pedestals of the AICPPP chip

First of all, to characterize the FE chips, we measured the noise of the chips through the acquisition of all the pedestal values. Figure 5.4 shows examples of the pedestal values of the FE chip for anodes. We can note that all the pedestals have similar values, that vary between $\sim$ 100 and $\sim$ 200 ADC channels, with an RMS between $\sim$ 0.8 and $\sim$ 1.7 ADC channels.

The pedestals of the chip for dynodes, on the contrary, are more variable than

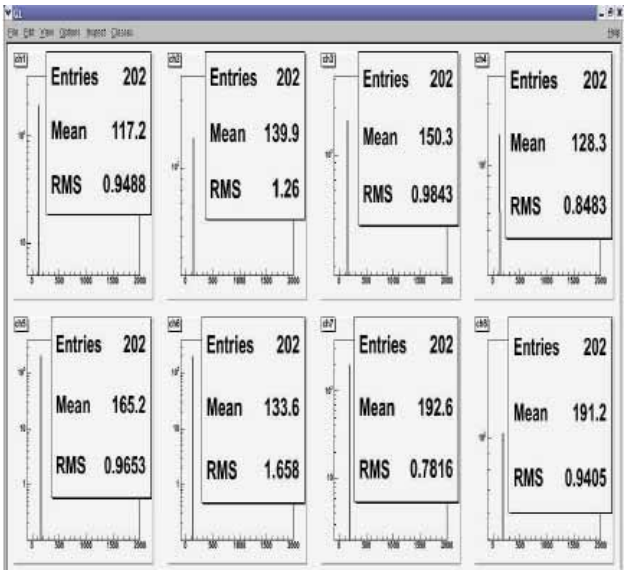

Figure 5.4: Some examples of the anode pedestals the AICPPP chip measured.

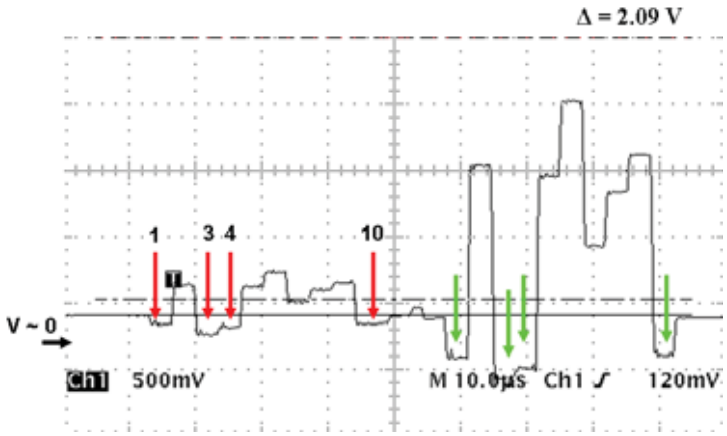

Figure 5.5: The analog output of the pedestals of a chip for dynodes. The negative values of the pedestals are well visible and indicated by the red arrows in the low scale output (gain 1) and with a green arrow in the $\times 5$ scale (gain 5).

the ones for anodes. Moreover, looking at the analog output of the FE chip, we noted some negative values, as shown in figure 5.5 which represents a screen-shot of the analog output of the chip for dynodes. In the figure, the negative values of the pedestals are well visible and indicated by the red arrows in the $1\times$ scale output (gain 1), and with a green arrow in the $5\times$ scale (gain 5). Because ADCs, dedicated to the digitalization, accepts only positive signals, the digital outputs of the negative pedestals were all fixed to zero. This effect induced an overestimation of the value of the pedestals and consequently an underestimation of the signals. In order to solve this problem, it was necessary to add a positive off-set to the analog output of the chip, shifting the pedestals to positive values before the ADC input.

For all the dynode FE chips, we measured the pedestal values, looking at the negative analog outputs. The following table shows all the thirty dynodes chips tested, the chips channels that had negative values of the pedestals, and the maximum offset found for the gain $1\times$[1].

Chip	**Channels**	**Max Offset (-mV)**	**Chip**	**Channels**	**Max Offset (-mV)**
$1-1$	1, 7	100	$2-1$	1, 4, 6, 8, 9, 10	250
$1-2$	1, 6	200	$2-2$	2, 4	200
$1-3$	1, 3, 4, 7, 8	200	$2-3$	1, 3, 4, 10	150
$1-4$	2, 5, 6	150	$2-4$	1, 2, 4, 6, 9, 10	100
$1-5$	2, 6, 8	100	$2-5$	1, 3, 4	150
$3-1$	4, 6, 8	200	$4-1$	1	200
$3-2$	3, 6	100	$4-2$	5, 6	150
$3-3$	2	50	$4-3$	-	-
$3-4$	2	50	$4-4$	10	200
$3-5$	2	50	$4-5$	6	50
$5-1$	4	150	$6-1$	10	50
$5-2$	2, 3, 6, 8	200	$6-2$	1, 4, 5, 10	100
$5-3$	2, 3, 7	200	$6-3$	3	100
$5-4$	5, 6	200	$6-4$	-	-
$5-5$	1, 4	100			

From the results shown in previous table, we found that it was enough to add a positive offset $\geqslant 250$ mV to made all the pedestal values acceptable. We created

[1]Flight electronics make use only of the gain $1\times$ measurement, because the anode/dynode PMTs read out is already a double scale measurement, as will be explained in next section.

this offset with a resistor ($R_{pull\ up}$) inserted between the FE chip output and the ADC input. A resistor $R_{pull\ up} \sim 16\ k\Omega$ was enough to increase the pedestals up to a positive value as shown by the red arrows in figure 5.6. This figure shows the same pedestals of figure 5.5, after the application of the $R_{pull\ up}$.

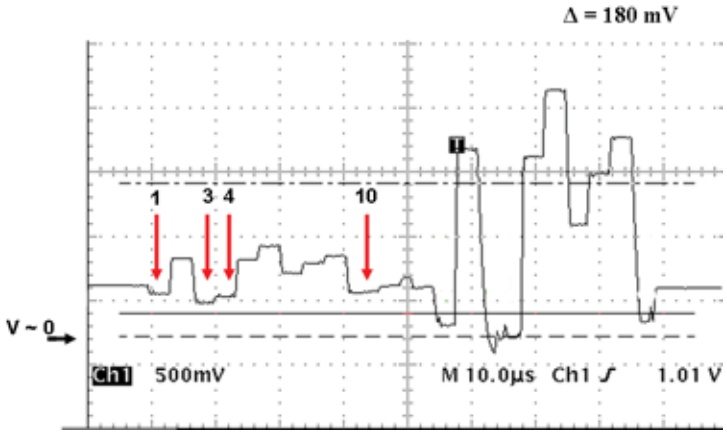

Figure 5.6: This figure shows the same pedestals of the figure 5.5, after the application of the $R_{pull\ up}$, we can note that the values of the channels in the low scale, as suggested by the red arrows, now are all positives.

As a side effect, the presence of the $R_{pull\ up}$ increases the time constant of the connection between the front-end chip and the ADC, loosing the synchronism with the ADC sample (*chip select*)[2]. This effect induced cross-talk between contiguous channels.

In order to sample the correct input value, we changed the software on the FPGA device. Finally combining the $R_{pull\ up}$ and the new software, we were able to make all thirty chips for dynodes signals fully efficient without any cross-talk between contiguous channels. Between the thirty chips we choose the best twenty-two to be installed on the TOF apparatus. The following table shows the dynode pedestals measured, one for each channel of every chip.

[2]The functionalities of the ADC has been already explained in chapter 3. It's useful to remember that the ADC digitalizes the analog value measured at the instant of the sample, i.e at the falling edge of the *chip select* signal.

Ch.	CHIP $1-2$	CHIP $1-3$	CHIP $1-4$	CHIP $2-1$
1	240.9 ± 2.0	89.2 ± 0.8	89.0 ± 0.8	170.6 ± 2.0
2	678.3 ± 2.1	409.5 ± 2.1	408.8 ± 1.9	302.3 ± 2.0
3	474.8 ± 1.9	128.2 ± 1.7	128.8 ± 1.8	369.1 ± 2.1
4	687.5 ± 1.7	127.4 ± 1.9	127.7 ± 1.9	202.6 ± 2.1
5	510.4 ± 1.9	330.8 ± 2.2	327.7 ± 2.3	744.3 ± 2.2
6	103.5 ± 1.8	347.6 ± 2.5	350.2 ± 2.3	118.9 ± 2.3
7	438.9 ± 1.9	44.9 ± 2.0	45.4 ± 2.0	530.1 ± 2.2
8	464.6 ± 2.0	110.6 ± 1.7	110.9 ± 1.8	4.6 ± 1.9
9	598.7 ± 2.0	366.7 ± 2.2	363.1 ± 2.2	226.8 ± 2.0
10	310.5 ± 1.9	435.6 ± 2.3	434.2 ± 2.3	174.9 ± 2.2

Ch.	CHIP $2-2$	CHIP $2-3$	CHIP $2-4$	CHIP $2-5$
1	439.1 ± 2.2	199.0 ± 2.0	163.9 ± 2.1	199.7 ± 2.0
2	226.6 ± 2.3	515.6 ± 2.1	210.3 ± 2.4	383.8 ± 2.4
3	319.1 ± 1.7	124.4 ± 2.0	547.3 ± 2.3	95.1 ± 2.0
4	85.0 ± 1.8	176.3 ± 2.0	210.6 ± 2.1	246.2 ± 2.0
5	620.2 ± 2.2	502.5 ± 2.1	460.8 ± 2.6	309.1 ± 1.8
6	546.6 ± 1.8	624.8 ± 2.2	200.4 ± 2.1	539.3 ± 2.1
7	356.3 ± 1.8	384.9 ± 2.2	513.34 ± 2.3	429.9 ± 1.1
8	369.7 ± 1.8	475.9 ± 2.1	631.6 ± 2.3	759.0 ± 2.1
9	665.0 ± 2.0	540.2 ± 2.3	237.0 ± 2.2	483.0 ± 2.1
10	557.0 ± 1.8	212.6 ± 2.2	183.1 ± 2.1	396.5 ± 1.8

Ch.	CHIP $3-1$	CHIP $3-2$	CHIP $3-3$	CHIP $3-4$
1	291.9 ± 2.0	418.1 ± 2.2	386.3 ± 2.0	597.1 ± 1.9
2	446.0 ± 2.0	347.4 ± 1.9	221.6 ± 2.1	256.3 ± 1.8
3	471.8 ± 2.0	230.6 ± 1.9	603.2 ± 2.0	462.1 ± 1.9
4	253.9 ± 2.0	444.3 ± 2.2	660.3 ± 2.1	331.7 ± 2.3
5	288.4 ± 2.0	327.7 ± 2.0	316.1 ± 2.1	275.3 ± 1.8
6	91.0 ± 2.7	196.8 ± 2.1	353.9 ± 2.0	315.1 ± 2.0
7	320.1 ± 1.9	470.3 ± 2.1	297.9 ± 2.2	447.5 ± 1.8
8	239.6 ± 2.2	538.2 ± 2.1	337.4 ± 2.1	623.9 ± 1.9
9	580.9 ± 2.4	435.0 ± 1.9	446.2 ± 2.0	379.8 ± 2.5
10	621.8 ± 2.1	463.7 ± 1.9	575.1 ± 1.7	365.1 ± 2.0

Ch.	CHIP $3-5$	CHIP $4-1$	CHIP $4-2$	CHIP $4-4$
1	606.9 ± 2.0	82.5 ± 1.6	385.1 ± 1.8	386.4 ± 1.9
2	256.8 ± 1.8	333.1 ± 2.1	374.3 ± 1.9	413.0 ± 2.4
3	509.2 ± 2.0	462.7 ± 2.2	479.2 ± 2.0	319.1 ± 2.0
4	559.5 ± 2.1	627.8 ± 2.0	305.0 ± 2.1	472.0 ± 1.7
5	286.2 ± 2.0	368.3 ± 2.1	248.5 ± 2.0	514.2 ± 1.9
6	348.7 ± 2.1	514.5 ± 2.0	117.0 ± 2.0	418.7 ± 2.5
7	544.3 ± 1.9	579.8 ± 1.9	290.3 ± 2.1	532.9 ± 2.0
8	741.0 ± 2.1	463.5 ± 2.0	533.9 ± 2.1	769.8 ± 1.9
9	369.1 ± 2.0	636.3 ± 2.1	474.7 ± 2.0	272.3 ± 2.1
10	362.9 ± 2.2	414.9 ± 2.1	517.1 ± 2.3	105.2 ± 1.7

Ch.	CHIP $4-5$	CHIP $5-1$	CHIP $5-2$	CHIP $5-3$
1	603.8 ± 1.9	468.3 ± 1.9	430.3 ± 2.1	439.4 ± 2.1
2	557.6 ± 2.1	763.2 ± 2.0	265.3 ± 2.1	232.1 ± 1.9
3	288.8 ± 2.2	510.9 ± 2.1	205.1 ± 2.1	268.0 ± 2.0
4	477.8 ± 2.0	125.3 ± 1.9	320.1 ± 1.9	438.2 ± 2.0
5	359.3 ± 2.0	733.3 ± 2.5	500.1 ± 2.0	384.2 ± 2.0
6	246.3 ± 2.1	423.4 ± 2.0	229.0 ± 2.0	441.5 ± 2.0
7	297.8 ± 1.9	408.4 ± 2.1	326.0 ± 2.1	235.8 ± 1.8
8	341.7 ± 2.0	279.0 ± 2.1	94.0 ± 2.0	874.4 ± 2.1
9	571.5 ± 2.1	606.6 ± 2.0	538.3 ± 2.4	305.6 ± 2.2
10	387.8 ± 1.9	567.4 ± 2.1	513.8 ± 7.0	563.1 ± 2.3

Ch.	CHIP $5-4$	CHIP $5-5$		
1	361.3 ± 2.1	188.0 ± 1.9		
2	783.3 ± 2.3	354.7 ± 1.9		
3	489.1 ± 1.9	413.0 ± 2.1		
4	577.4 ± 2.2	254.0 ± 2.1		
5	55.1 ± 1.9	322.8 ± 2.2		
6	163.6 ± 1.9	435.2 ± 2.0		
7	310.2 ± 2.0	473.2 ± 2.3		
8	387.3 ± 2.1	413.9 ± 1.9		
9	397.3 ± 2.1	441.9 ± 2.2		
10	632.6 ± 2.2	398.3 ± 2.0		

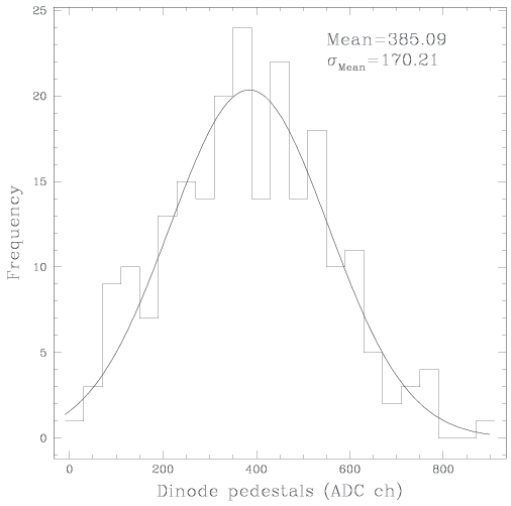

Figure 5.7: The distribution of all the dynode pedestals for the TOF apparatus. In contrast with the anode pedestals, the dynodes have a large distribution and can assume a wide range of values.

Figure 5.7 shows the distribution of all the dynode pedestals for the TOF apparatus. We can note that, in contrast with the anode pedestals, the dynodes have a large distribution and can assume a wide range of values.

5.2.2 The calibration of the chips for dynodes

All the chips for dynodes, already assembled on the SFEC cards, have been characterized before to be installed on the TOF detector. In order to characterize all of them we utilized the charge injector circuit already explain in the previous chapter.

Using the charge injector circuit, we gave in input to each channel of the chips, installed on the SFECs, an increasing signal. An example of the results obtained for three chips (chip 1-2, chip 1-3 and chip 1-4) is shown in figure 5.8. This figure shows the output of each channel (from 1 to 10) to the different charges in input: $\sim$ 125 pC, $\sim$ 320 pC, $\sim$ 515 pC, $\sim$ 710 pC and $\sim$ 900 pC. We can note form the figure that at every value of the input charge the output signals from the channels are all distributed around a common value excepted for some channels that differs around two or three sigma from the others.

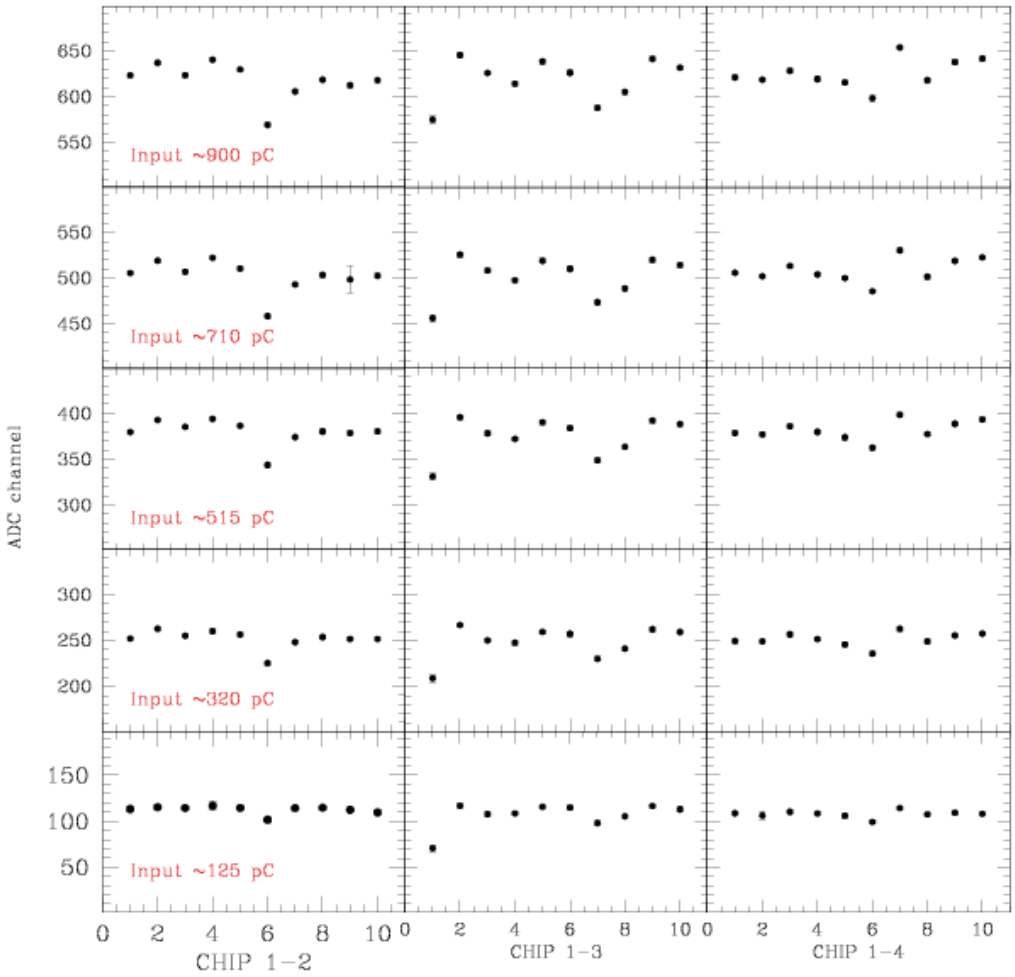

Figure 5.8: The results obtained for the three chips: chip 1-2, chip 1-3 and chip 1-4. The horizontal axis represents the channels, from 1 to 10, of the threes chips, while in the vertical axis are shown the ADC channels obtained in output when the charges of $\sim$ 125 pC, $\sim$ 320 pC, $\sim$ 515 pC, $\sim$ 710 pC and $\sim$ 900 pC are in input to the different channels of the chips.

In addition we made the calibration of the channels of the chips used and the fit parameters are shown on the following table.

CHIP 1-2		CHIP 1-3	
P_0	P_1	P_0	P_1
37.1 ± 2.1	42.2 ± 0.2	-3.3 ± 3.8	41.5 ± 0.4
40.7 ± 2.1	43.1 ± 0.2	41.1 ± 2.1	43.6 ± 0.2
40.9 ± 2.1	42.0 ± 0.2	30.3 ± 2.0	43.0 ± 0.2
49.1 ± 2.5	42.5 ± 0.2	33.0 ± 2.1	41.9 ± 0.2
38.9 ± 1.8	42.6 ± 0.2	37.2 ± 2.2	43.4 ± 0.2
29.7 ± 2.1	38.8 ± 0.2	40.5 ± 2.3	42.3 ± 0.2
41.2 ± 2.0	40.7 ± 0.2	23.2 ± 2.5	40.6 ± 0.3
39.7 ± 1.9	41.8 ± 0.2	30.8 ± 2.0	41.3 ± 0.2
40.2 ± 1.9	41.3 ± 0.2	39.7 ± 2.1	43.3 ± 0.2
35.8 ± 1.8	42.1 ± 0.2	37.9 ± 2.2	42.9 ± 0.2
CHIP 1-4		CHIP 2-1	
P_0	P_1	P_0	P_1
33.8 ± 2.1	42.4 ± 0.2	1.4 ± 1.9	48.3 ± 0.2
41.7 ± 2.8	41.5 ± 0.3	62.4 ± 5.1	42.9 ± 0.4
36.7 ± 2.2	42.9 ± 0.3	0.92 ± 2.01	50.1 ± 0.2
34.3 ± 2.0	42.3 ± 0.2	36.9 ± 2.1	45.8 ± 0.2
30.9 ± 2.2	42.2 ± 0.3	37.0 ± 2.0	46.8 ± 0.2
25.7 ± 2.2	41.4 ± 0.3	48.2 ± 3.2	44.0 ± 0.3
35.7 ± 2.4	44.6 ± 0.3	59.8 ± 3.3	45.7 ± 0.3
32.9 ± 1.9	42.2 ± 0.2	25.5 ± 2.2	45.1 ± 0.2
32.3 ± 1.7	43.8 ± 0.2	34.7 ± 2.0	46.4 ± 0.2
32.1 ± 2.1	44.1 ± 0.2	32.3 ± 2.1	46.5 ± 0.2
CHIP 2-2		CHIP 2-3	
P_0	P_1	P_0	P_1
38.5 ± 2.2	41.4 ± 0.2	36.9 ± 1.9	42.1 ± 0.2
35.8 ± 2.3	41.1 ± 0.2	37.1 ± 2.1	46.3 ± 0.2
39.3 ± 1.8	41.5 ± 0.2	32.6 ± 2.0	43.6 ± 0.2
26.6 ± 2.2	39.4 ± 0.2	34.6 ± 1.9	43.7 ± 0.2
41.1 ± 2.1	42.5 ± 0.2	37.9 ± 2.1	45.0 ± 0.2
39.0 ± 1.7	42.2 ± 0.2	40.3 ± 2.2	45.3 ± 0.2
41.3 ± 1.7	42.1 ± 0.2	41.1 ± 2.1	45.2 ± 0.2
38.4 ± 1.7	42.2 ± 0.2	38.4 ± 1.9	44.3 ± 0.2
37.9 ± 1.9	44.7 ± 0.2	39.6 ± 2.2	45.2 ± 0.2
37.6 ± 1.8	43.3 ± 0.2	37.9 ± 2.2	44.0 ± 0.2

CHIP 2-4		CHIP 2-5	
P_0	P_1	P_0	P_1
34.8 ± 2.1	42.0 ± 0.2	39.4 ± 1.9	42.8 ± 0.2
34.6 ± 2.2	42.5 ± 0.2	37.7 ± 2.4	44.0 ± 0.2
38.6 ± 2.3	44.1 ± 0.2	34.7 ± 2.1	43.2 ± 0.2
34.5 ± 1.9	43.0 ± 0.2	39.7 ± 1.8	43.0 ± 0.2
36.4 ± 2.2	43.1 ± 0.2	37.5 ± 1.7	44.7 ± 0.2
36.9 ± 2.1	42.1 ± 0.2	38.8 ± 2.0	44.6 ± 0.2
40.3 ± 2.5	43.1 ± 0.2	0.35 ± 1.12	-0.038 ± 0.125
37.7 ± 2.1	44.5 ± 0.2	40.6 ± 2.0	45.4 ± 0.2
35.8 ± 2.1	44.3 ± 0.2	38.1 ± 2.0	45.5 ± 0.2
34.8 ± 1.9	43.3 ± 0.2	37.6 ± 1.9	44.0 ± 0.2
CHIP 3-1		CHIP 3-2	
P_0	P_1	P_0	P_1
38.8 ± 2.0	44.82 ± 0.2	38.6 ± 2.3	40.4 ± 0.2
38.5 ± 2.1	44.96 ± 0.2	37.8 ± 2.1	40.1 ± 0.2
37.5 ± 1.9	44.39 ± 0.2	35.6 ± 2.0	39.4 ± 0.2
37.5 ± 1.9	43.41 ± 0.2	41.1 ± 2.1	39.7 ± 0.2
39.3 ± 2.0	43.31 ± 0.2	36.8 ± 1.9	39.7 ± 0.2
29.5 ± 2.7	43.46 ± 0.2	35.8 ± 2.1	38.7 ± 0.2
39.6 ± 2.0	44.04 ± 0.2	38.7 ± 2.1	41.9 ± 0.2
38.2 ± 2.0	44.10 ± 0.2	37.7 ± 2.1	42.7 ± 0.2
40.9 ± 2.2	45.65 ± 0.2	39.9 ± 2.0	40.5 ± 0.2
40.8 ± 2.0	46.08 ± 0.2	36.6 ± 1.8	41.8 ± 0.2
CHIP 3-3		CHIP 3-4	
P_0	P_1	P_0	P_1
42.2 ± 1.9	43.5 ± 0.2	38.3 ± 1.7	43.0 ± 0.2
38.0 ± 2.0	44.7 ± 0.2	38.9 ± 1.9	41.5 ± 0.2
40.0 ± 1.9	45.3 ± 0.2	38.2 ± 1.7	41.9 ± 0.2
41.2 ± 2.0	44.6 ± 0.2	38.4 ± 2.2	41.6 ± 0.2
39.7 ± 2.0	43.2 ± 0.2	38.3 ± 1.7	40.3 ± 0.2
38.7 ± 2.0	44.1 ± 0.2	39.9 ± 2.0	40.5 ± 0.2
41.4 ± 2.1	43.6 ± 0.2	38.8 ± 1.8	42.7 ± 0.2
38.8 ± 1.9	45.3 ± 0.2	40.3 ± 1.9	42.7 ± 0.2
38.7 ± 2.0	44.1 ± 0.2	40.9 ± 2.4	41.7 ± 0.2
38.3 ± 1.9	44.2 ± 0.2	38.4 ± 1.8	41.5 ± 0.2

CHIP 3-5		CHIP 4-1	
P_0	P_1	P_0	P_1
38.9 ± 2.0	44.5 ± 0.2	20.4 ± 2.5	38.3 ± 0.2
39.1 ± 1.8	42.5 ± 0.2	36.8 ± 2.0	41.1 ± 0.2
39.7 ± 1.8	44.2 ± 0.2	37.0 ± 2.0	42.9 ± 0.2
40.0 ± 2.0	42.1 ± 0.2	39.3 ± 2.0	42.7 ± 0.2
36.3 ± 1.9	44.0 ± 0.2	36.9 ± 2.1	41.9 ± 0.2
39.2 ± 2.1	43.5 ± 0.2	39.9 ± 2.0	42.0 ± 0.2
42.7 ± 1.9	41.7 ± 0.2	38.3 ± 1.9	43.0 ± 0.2
42.9 ± 2.0	44.7 ± 0.2	36.4 ± 1.9	42.4 ± 0.2
37.0 ± 1.9	43.6 ± 0.2	39.4 ± 2.0	43.1 ± 0.2
38.5 ± 2.0	42.7 ± 0.2	38.5 ± 2.1	43.0 ± 0.2

CHIP 4-2		CHIP 4-4	
P_0	P_1	P_0	P_1
40.7 ± 1.8	43.5 ± 0.2	39.3 ± 1.8	42.4 ± 0.2
39.3 ± 1.9	44.4 ± 0.2	39.0 ± 2.2	40.5 ± 0.2
41.7 ± 1.9	44.7 ± 0.2	41.3 ± 2.1	40.9 ± 0.2
41.4 ± 1.9	43.0 ± 0.2	38.5 ± 1.8	41.7 ± 0.2
40.4 ± 2.0	42.5 ± 0.2	39.7 ± 1.9	42.4 ± 0.2
36.2 ± 2.1	43.2 ± 0.2	39.6 ± 2.4	41.4 ± 0.2
39.0 ± 1.9	43.4 ± 0.2	38.4 ± 1.9	41.7 ± 0.2
41.7 ± 2.0	45.9 ± 0.2	44.1 ± 1.9	42.8 ± 0.2
42.0 ± 1.9	44.5 ± 0.2	40.9 ± 2.2	40.3 ± 0.2
38.6 ± 2.1	43.8 ± 0.2	29.0 ± 1.9	41.2 ± 0.2

CHIP 4-5		CHIP 5-1	
P_0	P_1	P_0	P_1
41.0 ± 1.9	42.0 ± 0.2	39.8 ± 2.0	44.8 ± 0.2
38.4 ± 2.0	42.7 ± 0.2	40.4 ± 2.0	46.7 ± 0.2
37.1 ± 2.2	41.9 ± 0.2	38.6 ± 2.2	44.6 ± 0.2
39.9 ± 1.9	41.8 ± 0.2	35.4 ± 1.9	40.9 ± 0.2
37.6 ± 2.0	41.7 ± 0.2	42.4 ± 2.2	44.3 ± 0.2
39.8 ± 2.2	40.4 ± 0.2	39.9 ± 1.8	44.1 ± 0.2
38.0 ± 1.9	41.6 ± 0.2	41.4 ± 2.2	44.0 ± 0.2
38.3 ± 1.9	41.8 ± 0.2	39.6 ± 1.9	44.7 ± 0.2
39.8 ± 2.0	43.4 ± 0.2	39.1 ± 1.9	45.7 ± 0.2
35.8 ± 1.8	43.3 ± 0.2	40.4 ± 2.0	45.2 ± 0.2

CHIP 5-2		CHIP 5-3	
P_0	P_1	P_0	P_1
44.3 ± 2.1	43.1 ± 0.2	41.9 ± 1.9	42.9 ± 0.2
41.7 ± 1.9	41.7 ± 0.2	41.2 ± 2.0	41.8 ± 0.2
38.9 ± 2.1	42.4 ± 0.2	37.2 ± 1.8	44.4 ± 0.2
40.4 ± 1.8	43.9 ± 0.2	39.3 ± 1.9	42.2 ± 0.2
41.0 ± 2.0	43.9 ± 0.2	40.3 ± 2.1	43.7 ± 0.2
39.6 ± 2.1	40.6 ± 0.2	39.2 ± 1.9	43.7 ± 0.2
38.3 ± 2.0	43.4 ± 0.2	39.7 ± 1.8	43.4 ± 0.2
29.1 ± 1.9	40.1 ± 0.2	40.1 ± 2.0	46.0 ± 0.2
42.3 ± 2.2	44.3 ± 0.2	37.9 ± 2.0	43.5 ± 0.2
40.5 ± 1.9	43.4 ± 0.2	40.9 ± 2.2	44.0 ± 0.2
CHIP 5-4		CHIP 5-5	
P_0	P_1	P_0	P_1
39.8 ± 2.1	43.3 ± 0.2	36.6 ± 1.9	41.9 ± 0.2
40.1 ± 2.2	45.9 ± 0.2	38.7 ± 1.8	41.7 ± 0.2
40.9 ± 1.9	43.6 ± 0.2	40.4 ± 1.8	42.9 ± 0.2
41.5 ± 2.2	44.6 ± 0.2	38.7 ± 2.1	40.8 ± 0.2
30.3 ± 2.3	42.0 ± 0.2	41.5 ± 2.1	41.5 ± 0.2
35.0 ± 2.0	42.3 ± 0.2	39.5 ± 2.1	43.1 ± 0.2
40.0 ± 2.0	43.6 ± 0.2	38.3 ± 2.1	42.8 ± 0.2
33.3 ± 2.5	46.2 ± 0.2	39.9 ± 1.8	44.2 ± 0.2
39.5 ± 2.0	44.5 ± 0.2	40.3 ± 2.0	43.2 ± 0.2
38.0 ± 2.1	46.0 ± 0.2	41.5 ± 2.1	43.0 ± 0.2

5.2.3 The time interval for the sample

The AICPPP chip, as already explained in chapter 3, has an architecture based on a spectrometry chain, which gives an output voltage signal proportional to the charge of the input pulse. So, an important characteristic of this chip is the sample time of the input signal, which has to memorize the peak of the shaper pulse when it is at its maximum and not during its rising or falling edge.

In order to find the right sampling temporization, we did many tests in most of the chips, changing the timing between the peak of the signal and the sample of the AICPPP chip. Figure 5.9 shows one of these tests for a FE chip. We note that between $\sim$1.6 μs and $\sim$1.85 μs the output signal remains constant. Taking into account that the temporization between the crossing particle signals and the fast

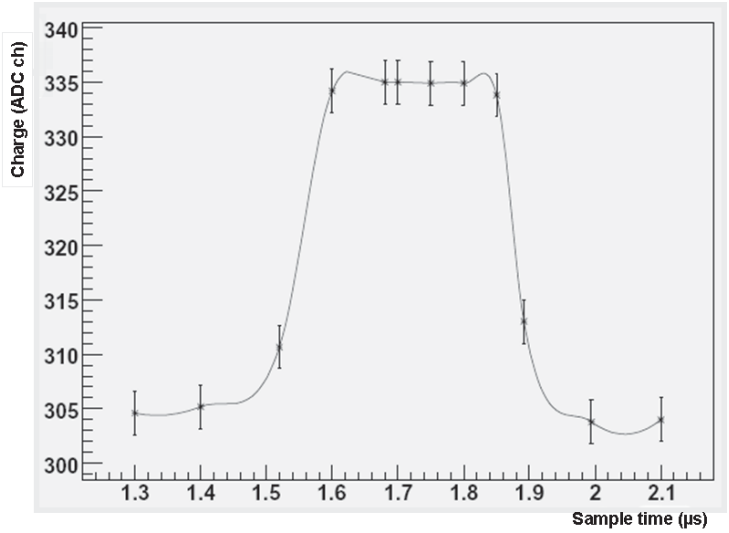

Figure 5.9: The horizontal axis shows the timing between the peak of the input signal and the sample of the AICPPP chip. Between $\sim$1.6 μs and $\sim$1.85 μs the output signal remains constant.

trigger generation is (100 ± 0.1) nsec [80], we decided to sample the signal 1.6 μs after the fast trigger one, i.e. about 1.7 μs after the anode/dynode peak. The peak amplitude is directly proportional to the total charge.

5.3 The dynamic range

The Charge Measurement Block of the TOF will have to measure the released charge from the particle crossing the TOF scintillators. We know from chapter 3 that the FE circuit can receive from 0 to 36 pC in input.

In the lower panel of figure 5.10: the vertical and the horizontal axis represent respectively the electrical charges in pC injected to the FE chip and the corresponding ADC channels measured in output by the CMB for each event. The upper panel of figure 5.10 shows, on the vertical axis, the number of events acquired, plotted on the lower panel, for each of the input charges. We can note that the FE chip has a linear response up to $\sim 36pC$ as input, i.e. $\sim$ 3500 ADC channels.

The reference signal, found in the Bologna laboratories, for a MIP that crosses

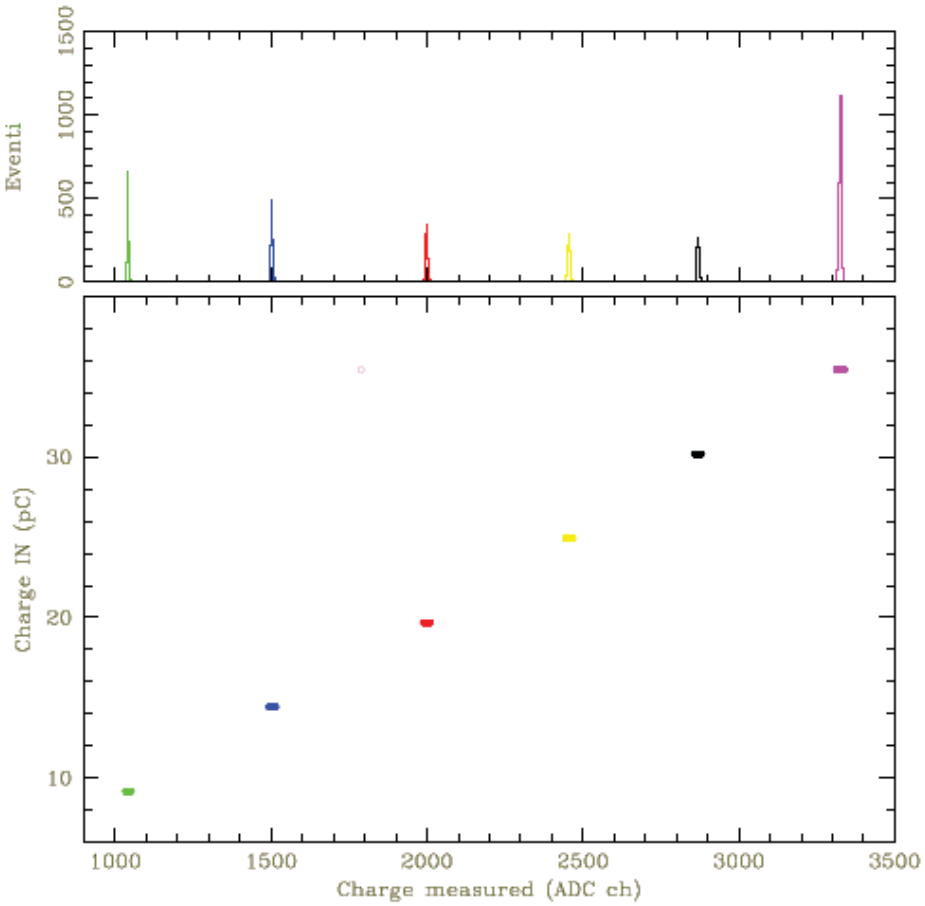

Figure 5.10: Lower panel: the vertical and the horizontal axis represent the electrical charges in pC, injected inside the front-end chip, and the corresponding ADC channels revealed at the output of the CMB for each event. Upper panel: the vertical axis represents the number of events plotted for each value of the input charge.

the TOF scintillators near the center, is a charge of 50 pC from the anode (as explained in chapter 4). So taking into account the dynamic input range of the chip, in order to reveal high Z CRs, it is necessary to reduce the signal generated by a crossing particle before putting it to the chip input.

After many tests with different kinds of resistors and capacitors, we reduced the input anodes and dynodes signal to the FE chip of a factor 100, using the

passive components shown in figures 5.11 and 5.12[3]: where the capacitor C has a value of 10 nF and the resistors R_1 and R_2 are equal to 50 Ω and 5 $k\Omega$ respectively. The 50 Ω resistor is used in order to avoid reflection on the cable, while the 5 $k\Omega$ to transmit only a fraction of the signal to the FE chip. Moreover the signal of the anodes is bigger, from 3 to 11 times, than the one of the corresponding dynodes. For this reasons, while the anodes will be important for the measure of low charge values, the dyno

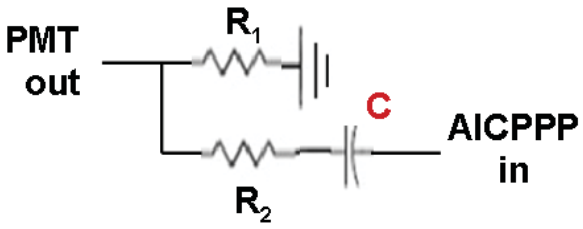

Figure 5.11: The passive components that connect the anode signals of a photomultiplier to the input of the front-end chip on the CMB of the SFET2 and SFEA2.

Figure 5.12: The passive components that connect the dynode signals of a photomultiplier to the input of the front-end chip on the CMB of the SFEC.

We can note that this method has the ability to increase the dynamical range of the CMBs for anodes and for dynodes. In order to measure the dynamic range of the CMBs, we used the test bench explained in the previous chapter, with the S9007 testing board and the charge injector circuit built for this purpose, already explained in previous chapter.

[3]Because the anode and dynode signals are in voltage and current mode signals respectively, the connections with the FE chips are different.

5.3.1 The dynamic range measurements

As already explained, the CMB input range has been increased reducing the PMT signal to a factor of 100, through the passive components placed before the chip input.

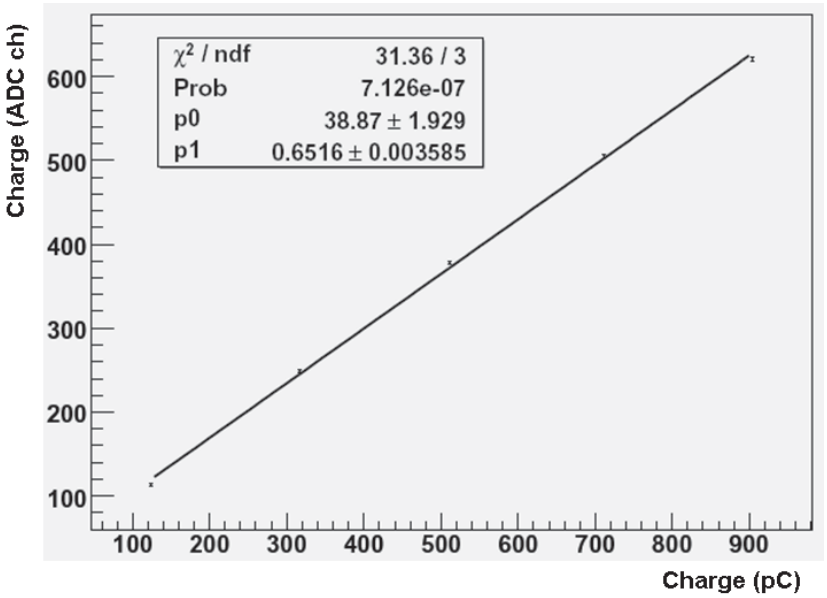

Figure 5.13: The horizontal and vertical axis represent respectively the electrical charges in pC, in input to the CMB, and the corresponding ADC channels measured at the output.

The anode signal that can be reveled by the CMB, varies from 0 to 3600 pC, i.e. from 0 to 72 MIPs (where 1 MIP $\simeq$ 50 pC). Using the charge injector circuit, increasing the signals in input to the CMB from a charge of few pC to a charge of 900 pC (the maximum value allowed with this circuit), we obtained the graph in figure 5.13 for a chip. In this figure the horizontal and the vertical axis represent respectively the electrical charges in pC in input to the CMB, and the corresponding ADC channels measured at the output. Assuming that all the crossing particles are at their minimum of ionization with a fixed β, the charge lost on the scintillator can be considered $\propto Z^2$. The anode range can then be expressed in terms of Z of the crossing CR, so we expect to detect with the anode signal CRs til $Z = 8$. For example, in figure 5.13 we expect the Helium's peak at 200 pC that correspond to

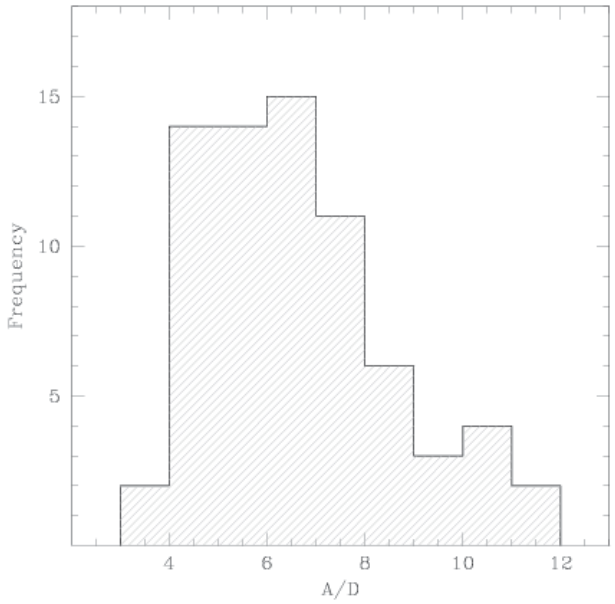

Figure 5.14: The anode/dynode signals (A/D) ratio of the PMT mounted on the TOF, varies from 3 to 11.

$\sim$ 170 ADC channels from the pedestal value.

The dynode signal that can be reveled by the SFEC, depends on the anode/dynode (A/D) ratio, which for the flight TOF PMTs has values from 3 to 11, as shown in figure 5.14. When A/D ratio is equal to 3, the corresponding anode value varies between 0 to 14400 pC, i.e from 0 to 288 MIPs; when the A/D ratio is equal to 11, the anode varies between 0 and 39600 pC, i.e. from 0 up to 792 MIPs. The same considerations made for the anode, can be applied to the dynodes, i.e. the dynode range can be expressed in terms of Z of the crossing CR.

Figure shows the expected dynamic range of the anodes (red line), the one of the dynodes when A/D ratio is equals 3 (dotted line) and when A/D ratio equals 11 (solid line). The sketched area indicates the dynode's dynamic ranges when A/D ratio is between 3 and 11.

Considering that for each crossing particle the released charge is collected by at least 6 anodes and 12 dynodes, we have the possibility to choose the most appropriated dynamic range to identify the charge.

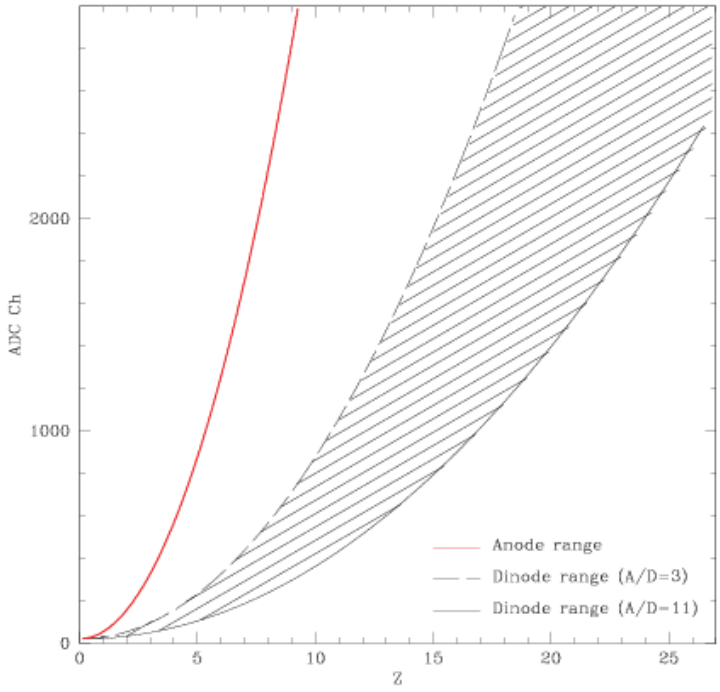

Figure 5.15: The expected dynamic range of the anodes (red line), the one of the dynodes when the A/D ratio is equal to 3 (dotted line) and when the A/D ratio is equal to 11 (solid line). The sketched area indicates the dynode's dynamic ranges when the A/D ratios are between 3 and 11.

5.4 Thermal tests

Most of the electronics on the AMS will have to be able to stand temperatures from -20 °C up to +50 °C, depending on whether the ISS is exposed to the sun or is in the earth's shadow. The purpose of the thermal tests is to verify the ability of the SFEC to operate in the extreme conditions of space.

The thermal tests were done at the IFAC Institute, in Florence, with a set-up composed of: a SFEC board, a temperature monitored chamber, a thermistor (mod. B57703-M103G10k) to measure the temperature on the board, the testing board for the data acquisition and a photomultiplier for the input signals (see figure 5.16).

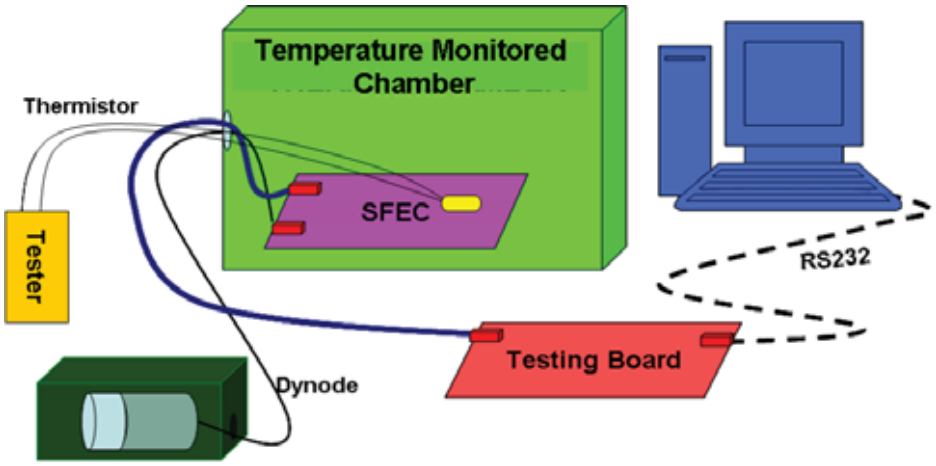

Figure 5.16: The set-up used for the thermal tests on the SFEC was composed of: a temperature monitored chamber, a thermal sensor on board of the SFEC, the testing board for the acquisition of the data and a photomultiplier that generates the input signals.

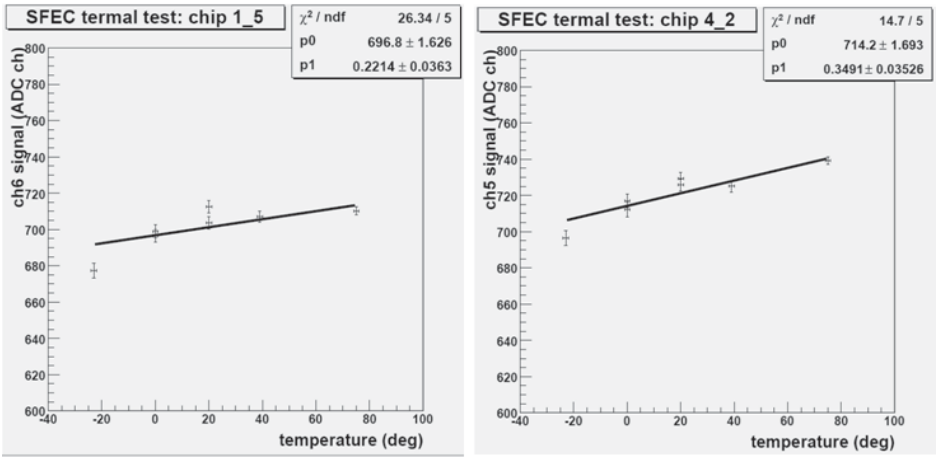

Figure 5.17: This plot represents the variations of the signals coming form the chip 1-5 (left) and the chip 4-2 (right) as a function of the temperature.

We tested the functionalities of the SFEC changing the temperatures between +75.5 °C and -20 °C, and also measuring at +40°, +20° and 0°C. We first ac-

quired the pedestals and then the signals from all the channels of the two FE chips mounted on the SFEC (chips 1-5 and chip 4-2). The pedestal variation was around $\pm 3\%$. The signal of one channel from each chip is shown on the figure 5.17. In both cases the signal changes proportionally to the temperature of $(2\% \div 3\%)$ from the environment temperature values. Finally we can say that the SFEC board did not significantly change its intrinsic characteristics and the value of the measurements with the temperature.

This thermal test was done on the prototype of the SFEC board. The space qualification test of the board, necessary for the endorsement of AMS-02 collaboration, will be made on flight models of the SFEC (installed on the detector) together with the TOF detector. This test, described in the next section, will be made for the lower TOF detector in May 2006 in Terni (Italy).

5.5 The thermal-vacuum test

The assembly of the lower TOF detector (figure 5.18) has already been started in the Bologna INFN laboratories, and will be finished at the end of March 2006. In order to qualify this half part of the TOF detector, a thermal-vacuum test will be done in May 2006 at SERMS laboratories in Terni. The purpose of this test is to verify the correct behaviour of the whole system under conditions similar to the possible space environment. The test will consist of four cycles in a vacuum chamber, and it shall demonstrate the ability of the equipment to operate when exposed to extreme operational temperatures after being exposed to an extreme non-operational in vacuum environment.

The characteristics of the SERMS Thermal-Vacuum (TV) chamber shown in figure 5.19, which will be used for the Thermal Vacuum Test (TVT) of the lower-TOF, are:

- Chamber dimensions (diameter $\times$ height): $2100 \times 2100\ mm^2$;
- Pressure range: 1000 mbar to 3×10^{-5} mbar (10^{-7} mbar reached during commissioning);
- Temperature range: -70 up to $+125°$C;
- Temperature gradient: $1°$/minute with empty chamber;
- Temperature stability: $\pm$ 1 degree

Figure 5.18: The assembly of the lower TOF detector has already been started in the Bologna INFN laboratories.

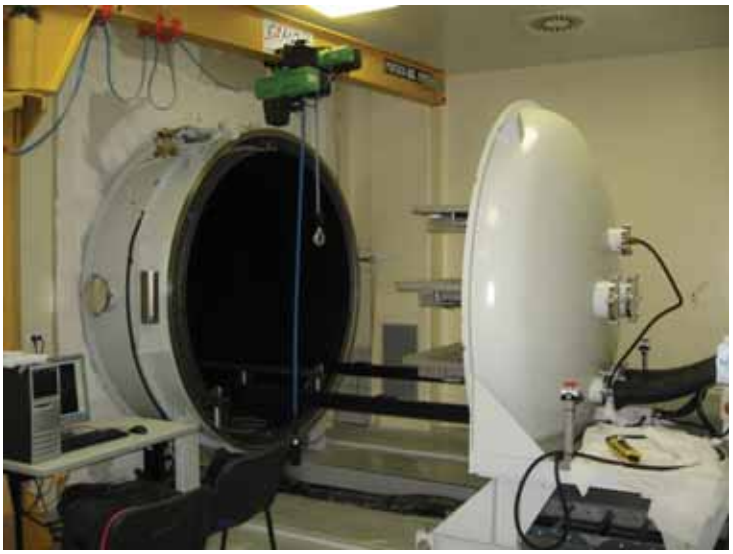

Figure 5.19: The SERMS Thermal-Vacuum chamber where will be tested the Lower TOF apparatus.

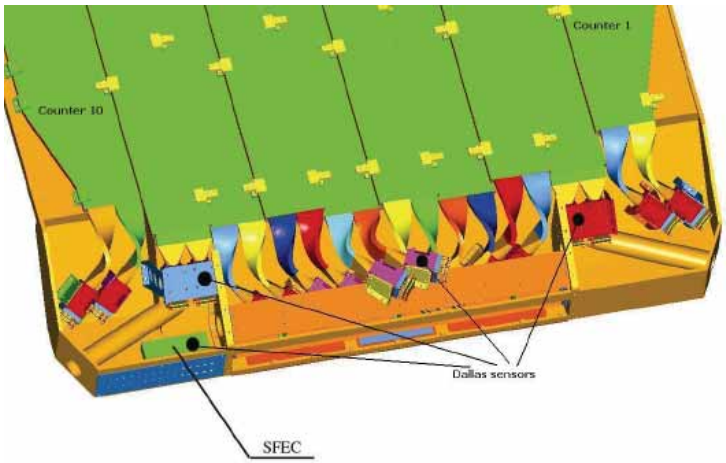

Figure 5.20: The PMTs are placed on an internal side of the Lower TOF, and they will be monitored by means of flight temperature sensors (Dallas sensors). The position of the SFEC board is also shown.

- Cold plates (mounted on the inner wall of the door): low $500 \times 1820\ mm^2$, mid $500 \times 1970\ mm^2$, and high $500 \times 1550\ mm^2$.

The SFECs are placed on an internal side of the Lower TOF together with the PMTs, all powered at 1950 Volts, and monitored by means of flight temperature sensors (Dallas sensors). Their locations are shown in figure 5.20. Two different kinds of thermal sensors are foreseen to be used during the test:

- (16) flight Dallas sensors located internally,
- (44) test sensors (PT100) located externally.

The anode signals of one central counter of plane X and of one central counter of plane Y will be monitored and processed by a 4 channel digital scope used to generate a trigger signal at the passage of cosmic rays. Figure 5.21 shows the lower TOF electronic setup for the functional TVT. The expected rate of cosmic rays being about 20 Hz.

Figure 5.22 shows the test profile of the TVT made by the Carlo Gavazzi Space SpA. The maximum and minimum PMTs acceptance temperature are:

- max and min acceptance operating: + 50 °C and -30°C;

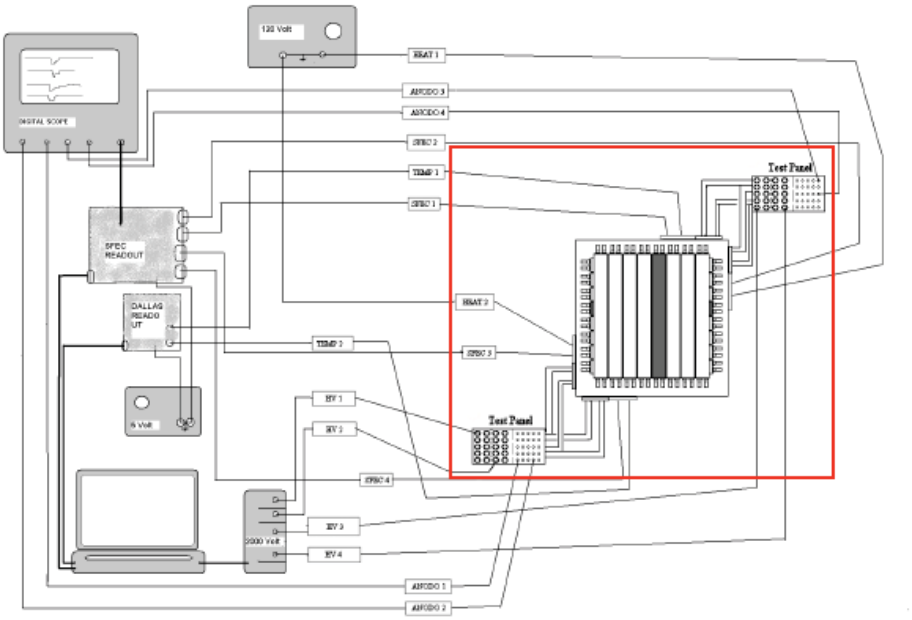

Figure 5.21: Lower TOF electronics setup for the functional TVT.

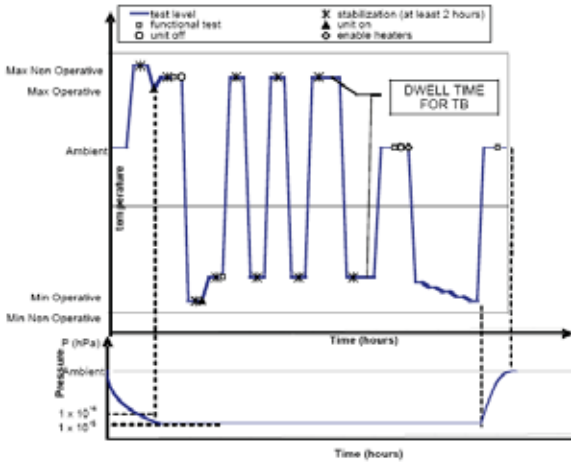

Figure 5.22: Carlo Gavazzi Space planned TVT test profile for Lower TOF.

- max and min acceptance non operating: +55 °C and -40 °C.

The thermal cycling test shall be considered successful in absence of degradation or malfunction of the Lower TOF during and after exposure to extreme hot and cold environments.

5.5.1 The vibration test

As part of the qualification procedure of the detector (including SFECs), the vibration tests of the lower TOF will be done in the SERMS laboratories in Terni. The vibration test is a very complicated test because its target is the full reproduction of all the vibration modes induced by the shuttle departure and flight. For this reason C. G. Space has produced many structural analysis to be verified by the test. From the vibrational analysis made by C. G. Space a specific test for the SFECs are not necessary because they are very small (5 $\times$ 12 cm), and have many points of connection with the TOF apparatus. Therefor they will be tested for the vibration inside the TOF. In order to understand if the vibrations will modify the way the apparatus functions we will test it before and after the vibration test. In figure 5.23 the vibration camber is shown.

Figure 5.23: The vibration test of the lower TOF will be done with the SERMS vibration chamber shown in this figure.

Conclusions

The SFEC card for the released charge measurement has been developed with the purpose to improve the measure of the charge released by cosmic rays crossing the TOF scintillators of the AMS-02, with the respect to AMS-01.

This thesis presents the work of my PhD studies in the AMS-Bologna group. At the beginning I deepened my knowledge of the cosmic rays astrophysics. First of all I focused on primary cosmic rays electrons and then I investigated the power of the TOF of AMS-02 in the study of the composition of cosmic rays. Subsequently, as principal task, I was responsible for the development of the SFEC board and of the Charge Measurement Blocks (CMBs) inside all the front-end cards of the TOF starting from the prototype and up to the flight model.

The flight version of the SFECs has been obtained thanks to several steps on preliminary prototypes: these steps are resumed below.

- First of all, we achieved the final version of the VHDL code of the FPGA, assembled inside the SFEC. We optimized it, determining the fastest reading frequency of work without loosing in efficiency.
- Then we realized a set-up in the Bologna laboratories in order to test all the prototypes. Using an FPGA, we acquired the signals of different SFECs simultaneously.
- Afterwards we optimized the passive components connecting the output of the photomultipliers to the inputs to the AICPPP chips for a correct matching of the dynamic range.
- Subsequently we characterized thirty chips for dynodes. We measured the pedestals value, the temporization for the sample and finally we calibrated all the channels of every chip. Among these thirty chips we chose the best ones (having low power consumption and dissipation, and lowest cross-talk) to be installed on the TOF detector.

- We measured the dynamical range of the SFEC up to 900 pC in order to define the charge measurement range.
- Next, we made thermal tests on the SFEC boards. Changing the temperature of the board between -20 and +70 °C, the SFECs did not show significant changes on their intrinsic characteristics and on calibration constants.
- Eventually, we assembled the flight version of the SFEC boards on the lower TOF detector.

Now, we are preparing the thermal-vacuum and the vibration tests for the space qualification of the Lower-TOF and of the SFECs, as parts of the apparatus.

In the future, we will repeat on the CMBs all the tests and the characterization made for the SFEC boards. Then, we will choose the best CMB prototypes in order to assemble them on the flight models of the front-end SFET2 and SFEA2 boards.

At the same time, we will develop the interface on the Scintillator Data Reduction board (SDR2) for the acquisition of all the data from the front-end boards (SFEC, SFET2 and SFEA2).

Appendix A

The Master code

Master.VHD is the VHDL code on the SDR board, that generates the *clock* for the charge measurement block (*Prime-ln*) for the acquisition and the digitalization of 32 or 10 inputs channels. Each channel is connected to an anode or dynode of a TOF photomultiplier.

```
-- MASTER.VHD
    library ieee;
    use ieee.std_logic_1164.all;
    use ieee.std_logic_arith.all;
    use ieee.std_logic_unsigned.all;

entity master is
port (
    reset    : in  std_logic;       -- TTL active low
    clk50    : in  std_logic;       -- clk 50 MHz
    trigger  : in  std_logic;       -- TTL active high
    setch    : in  std_logic;       -- TTL high to read 32 channels,
                                    -- low to read 10 ch
    prime_ln : out std_logic        -- Clock for the Charge Measurement Block
  );
end master;

architecture bhv of master is
  signal PL1, PLCEN, clk_80  : std_logic;
  signal state               : std_logic_vector (2 downto 0);
```

```
  signal sample, via, two-us : std_logic;
  signal n_clk               : std_logic_vector (10 downto 0);
  signal tst, stop           : std_logic;
  signal start, ft           : std_logic;
  signal retard              : std_logic_vector (10 downto 0);
  signal retard2us           : std_logic_vector (10 downto 0);

  component counter is port (
    reset   : in  std_logic;          -- TTL active low
    clk     : in  std_logic;          -- Clock
    enable  : in  std_logic;          -- TTL active high
    count   : in  std_logic_vector (10 downto 0);
    end     : out std_logic           -- TTL high if counter value = count
    );
  end component counter;

  component divider is port (
    reset   : in  std_logic;
    clk_in  : in  std_logic;
    clk_out : out std_logic);           -- Clock_out frequency is
                                        -- half than clock_in frequency
  end component divider;

begin

-- Clk_80 has a semi-period of 80 nsec
  DV1 : divider
    port map (
      reset   => reset,
      clk_in  => clk50,
      clk_out => clk_80
      );

-- Sample of the AICPPP chip after 1.7 us after the Fast Trigger
  cont1 : counter
    port map(
      reset     => reset,
```

```
      clk       => clk_80,
      enable    => ft,
      count     => retard,
      end       => sample
      );

-- Starts the digitalization of the first channel after 2 us when
the signal is stable (This procedure is necessary only for the first
channels)
  cont2 : counter
    port map(
      reset     => reset,
      clk       => clk_80,
      enable    => start,
      count     => retard2us,
      end       => two-us
      );

-- Counts the number of clock: n_clk can be enough to read 32 or 10
channels
  cont3 : counter
    port map(
      reset     => reset,
      clk       => clk_80,
      enable    => via,
      count     => n_clk,
      end       => stop
      );

-- State machine
  center: process (clk_80, reset) is
    variable cont : integer range 10 downto 0;
  begin
    if (reset = '0') then
      PL1       <= '0';
      via       <= '0';
      tst       <= '0';
```

```
  state     <= "111";
  ft        <= '0';
  start     <= '0';
  cont      := 0;
  n_clk     <= "00000000000";
  retard    <= "00000010001";       -- 1.7 us after the fast trigger
  retard2us <= "00000010111";       -- 2us after ch1 starts the
                                    -- digitalization
elsif rising_edge(clk_80) then
  if (trigger = '1' and tst = '0' ) then
    state   <= "000";
  else
    case state is
      when "000"  =>
        PL1         <= '1';
        via         <= '0';
        state       <= "001";
        ft          <= '1';     -- Starts the counter for the sample
        tst         <= '1';     -- Flag
      when "001"  =>
        PL1         <= '0';
        if cont = 4 then
          cont      := 0;
          state     <= "010";
        else
          cont      := cont+1;
          state     <= "000";
        end if;
      when "010"  =>
        if sample = '1' then
          ft        <= '0';
          state     <= "011";
        else
          state     <= "010";
        end if;
      when "011"  =>
        PL1         <= '1';
```

```
      state       <= "100";
    when "100"  =>
      PL1         <= '0';
      if cont = 3 then
        state     <= "101";
        start     <= '1';
        cont      := 0;
      else
        cont      := cont + 1;
        state     <= "011";
      end if;
    when "101"  =>
      if two-us = '1' then
        state     <= "110";
        start     <= '0';
        if setch = '1' then           -- 32 channels
          n_clk   <= "10001111011";
        else
          n_clk   <= "00101100011";   -- 10 channels
        end if;
      else
        PL1       <= '0';
        state     <= "101";
      end if;
    when "110"  =>
      if stop = '1' then
        via       <= '0';
        n_clk     <= "00000000000";
        state     <= "111";
      else
        state     <= "110";
        via       <= '1';
      end if;
    when others =>
                  null;
  end case;
end if;
```

```
    end if;
  end process center;

-- PLCEN is the CMB clock, it has the value of PL1 at the beginning
of an event to give the reset and the sample and hold. Then it has
the value of PLCEN that is a constant clock, for the acquisition and
the digitalization of all the channels
  selector : process (clk_80, reset)
  begin
    if (reset = '0') then
      PLCEN         <= '0';
    elsif (clk_80 'event and clk_80 = '1') then
      if via = '1' then
        PLCEN       <= not PLCEN;
      else
        PLCEN       <= PL1;
      end if;
    end if;
  end process selector;

  prime_ln          <= PLCEN;

end bhv;
```

Appendix B

The Charge Measurement Block code

CMB.VHD is the VHDL code in the FPGA Actel A08 lodged on the Charge Measurement Block inside the TOF front-end boards SFEC, SFET2 and SFEA2.

```
-- CMB.vhd
    library ieee;
    use ieee.std_logic_1164.all;
    use ieee.std_logic_arith.all;
    use ieee.std_logic_unsigned.all;

entity CMB is
  port (
    prime_line_1: in  std_logic;  -- Input CMB clock macro cell
    prime_line  : in  std_logic;  --
    Res_Pwron   : in  std_logic;  -- Signal from the Reset-Power On circuit
    time_out    : in  std_logic;  -- Signal from the time-out circuit
    dat_adc_1   : in  std_logic;  -- DATA from ADC1
    dat_adc_2   : in  std_logic;  -- DATA from ADC2
    time_out_in : out std_logic;  -- Input to the time-out circuit
    res_AICPPP_1 : out std_logic;  -- Reset AICPPP chip1
    res_AICPPP_2 : out std_logic;  -- Reset AICPPP chip2
    cs_adc_1    : out std_logic;  -- Chip select ADC1
    cs_adc_2    : out std_logic;  -- Chip select ADC2
```

```
    clk_adc_1   : out std_logic;  -- Clock to the ADC1
    clk_adc_2   : out std_logic;  -- Clock to the ADC2
    clk_AICPPP_1 : out std_logic;  -- Clock to the AICPPP chip1
    clk_AICPPP_2 : out std_logic;  -- Clock to the AICPPP chip2
    dat_1_out   : out std_logic;  -- Output DATA 1
    stb_1_out   : out std_logic;  -- Output STROBE 1
    dat_2_out   : out std_logic;  -- Output DATA 2
    stb_2_out   : out std_logic); -- Output STROBE 2
end CMB;

architecture bhv of CMB is
  signal state                          : std_logic_vector (4 downto 0);
  signal ch                             : std_logic_vector (3 downto 0);
  signal res_AICPPP, clk_AICPPP, res_AICPPP1, clk_AICPPP1   : std_logic;
  signal clk1, clk2, res_AICPPP2, clk_AICPPP2               : std_logic;
  signal flagres, mask1, mask2, dstb_cntrl_1, dstb_cntrl_2  : std_logic;
  signal reset, en, clk_sped                                : std_logic;
  signal clk_adc, cs, dtst                                  : std_logic;
  signal dat_buff_1, dat_buff_2                             : std_logic;
  signal stb_buff_1, stb_buff_2                             : std_logic;

begin

  clk_adc       <=  not (clk1 xor clk2);
  clk_adc_1     <=  clk_adc;
  clk_adc_2     <=  clk_adc;
  time_out_in   <=  prime_line and flagres;
  reset         <=  Res_Pwron and (not time_out);
  res_AICPPP_1  <=  res_AICPPP;
  res_AICPPP_2  <=  res_AICPPP;
  cs_adc_1      <=  cs;
  cs_adc_2      <=  cs;
  clk_AICPPP_1  <=  clk_AICPPP;
  clk_AICPPP_2  <=  clk_AICPPP;
  dat_1_out     <=  dat_buff_1;
  stb_1_out     <=  stb_buff_1;
  dat_2_out     <=  dat_buff_2;
```

```
  stb_2_out     <=  stb_buff_2;
  dstb_cntrl_1  <=  (dat_adc_1) xor (dat_buff_1);
  dstb_cntrl_2  <=  (dat_adc_2) xor (dat_buff_2);

ffc1: process (reset, prime_line_1)
    begin
        case reset is
        when '0'  =>
            flagres      <= '0';
            clk1         <= '1';
            clk2         <= '1';
            res_AICPPP   <= '0';
            clk_AICPPP   <= '0';
            cs           <= '1';
            dtst         <= '1';
            dat_buff_1   <= '0';
            stb_buff_1   <= '0';
            dat_buff_2   <= '0';
            stb_buff_2   <= '0';
            state        <= "00000";
            en           <= '1';
            ch           <= "0000";

       when '1'  =>
            if  rising_edge(prime_line_1) then
                flagres       <='1';
                if  ((en = '1') and not(stato="10101")) then
                    state       <= state + '1';
                elsif ((en = '1') and (stato="10101")) then
                    state       <= "00100";
                end if;
                if (cs = '0') then
                    clk1        <= not clk1;
                end if;
                if (state = "01000") then
                    dtst        <= '0';
                elsif (state = "10100") then
```

```
        dtst        <= '1';
    end if;
    if (state = "00011" or state ="00101") then
        clk_AICPPP  <= '1';
    else
        clk_AICPPP  <= '0';
    end if;
    if (state = "00001") then
        res_AICPPP  <= '1';
    else
        res_AICPPP  <= '0';
    end if;
    if ((state = "10101") and not(ch = "1010")) then
        ch          <= ch + 1;
    elsif ((state = "10101") and (ch = "1010")) then
        en          <= '0';
    end if;
    if ((dstb_cntrl_1= '1') and (dtst='0')) then
        dat_buff_1  <= dat_adc_1;
    elsif ((dstb_cntrl_1='0') and (dtst='0')) then
        dat_buff_1  <= dat_adc_1;
        stb_buff_1  <= not (stb_buff_1);
    end if;
    if ((dstb_cntrl_2='1') and (dtst='0')) then
        dat_buff_2  <= dat_adc_2;
    elsif ((dstb_cntrl_2='0') and (dtst='0')) then
        dat_buff_2  <= dat_adc_2;
        stb_buff_2  <= not(stb_buff_2);
    end if;
end if;

if (falling_edge (prime_line_1)) then
    if (state = "00100") then
        cs          <= '0';
    elsif (state = "10100") then
        cs          <=  '1';
    end if;
```

```
                if (cs = '0') then
                    clk2        <= not clk2;
                end if;
            end if;
    end case;
  end process;
end bhv;
```

Appendix C

ACRONYMS

ACR	Anomalous Cosmic Rays
ADC	Analog to Digital Converter
CAMAC	Computer Automated Measurement And Control
CDM	Cold Dark Matter
COTS	Commercial Of The Shelf
CR	Cosmic Ray(s)
CS	Chip Select
DAC	Digital to Analog Converter
DAQ	Data AcQuisition
DRM	Diffusive Reacceleration Model
FE	Front-End (electronics)
FIP	First Ionization Potential
FPGA	Field Programmable Gate Array;
GRB	Gamma-Ray Burst
GUI	Graphical User Interface
HV	High Voltage
ISM	Inter-Stellar Medium
ISS	International Space Station
LEP	Large Electron-Positron collider
LIS	Local Interstellar Spectrum
LPS	Lightest Supersymmetric particles
LV	Low Voltage
LVDS	Low Voltage Differential Signaling
MC	Monte Carlo
MIP	Minimum Ionizing Particle
NIM	Nuclear Instrument Module
PCB	Printed Circuit Board
PMT	PhotoMultiplier Tube
SAA	South Atlantic Anomaly
SEE	Single Event Effect
SEL	Single Event Latchup
SEU	Single Event Upset
SN	Supernova
TDC	Time to Digital Converter

C.1 AMS ACRONYMS

AMS	Alpha Magnetic Spectrometer
CMB	Charge Measurement Block
CP	Charged Particle digital signal
FE	Front-End (electronics)
FIP	First Ionization Potential
FT	Fast Trigger
LT	Low Threshold
RICH	Ring Imaging CHerenkov
SDR	Scintillator Data Reduction board
SFEA	Scintillator Front-End Anticoincidence board
SFEC	Scintillator Front-End Charge board
SFET	Scintillator Front-End Time board
SHT	Super-High Threshold
TOF	Time Of Flight
TRD	Transition Radiation Detector
TV	Thermal-Vacuum
TVT	Thermal-Vacuum Test

Bibliography

[1] I. V. Moskalenko. Propagation of Cosmic-Ray and Diffuse Galactic Gamma-Rays. *Frascati Physics series*, pages 1–11, 2004.

[2] H. J. Völk. Gamma-ray astronomy of cosmic rays. In *International Cosmic Ray Conference*, pages I3+, 2001.

[3] J. R. Hörandel. On the knee in the energy spectrum of cosmic rays. *APS Meeting Abstracts*, April 2002.

[4] Groom D.E. *et al.* Review of particle physics. *The European Physical Journal*, C15, 200.

[5] J. A. Bellido, R. W. Clay, B. R. Dawson, and M. Johnston-Hollitt. Southern hemisphere observations of a 10^{18} eV cosmic ray source near the direction of the Galactic Centre. *Astroparticle Physics*, 15:167–175, April 2001.

[6] N. Hayashida, M. Nagano, D. Nishikawa, H. Ohoka, N. Sakaki, M. Sasaki, M. Takeda, M. Teshima, R. Torii, T. Yamamoto, S. Yoshida, K. Honda, N. Kawasumi, I. Tsushima, N. Inoue, E. Kusano, K. Shinozaki, N. Souma, K. Kadota, F. Kakimoto, K. Kamata, S. Kawaguchi, Y. Kawasaki, H. Kitamura, Y. Matsubara, K. Murakami, Y. Uchihori, and H. Yoshii. The anisotropy of cosmic ray arrival directions around 10ˆ18 eV. *Astroparticle Physics*, 10:303–311, May 1999.

[7] Malcolm S. Longair. *High Energy Astrophysics*, volume 1,2. 2 edition, 1992, 1994.

[8] K.-H. Kampert, T. Antoni, W. D. Apel, F. Badea, K. Bekk, A. Bercuci, H. Blümer, E. Bollmann, and Bozdog. The physics of the knee in the cosmic ray spectrum. In *International Cosmic Ray Conference*, pages I240+, 2001.

[9] E. G. Berezhko. Particle acceleration in supernova remnants. In *International Cosmic Ray Conference*, pages I226+, 2001.

[10] Hagiwara K. *et al.* Review of Particle Physics. *Physical Review D*, 66: 010001+, 2002. URL `http://pdg.lbl.gov`.

[11] J. J. Engelmann, P. Ferrando, A. Soutoul, P. Goret, and E. Juliusson. Charge composition and energy spectra of cosmic-ray nuclei for elements from Be to NI - Results from HEAO-3-C2. *A&A*, 233:96–111, July 1990.

[12] N. E. Yanasak, M. E. Wiedenbeck, R. A. Mewaldt, A. J. Davis, A. C. Cummings, J. S. George, R. A. Leske, E. C. Stone, E. R. Christian, T. T. von Rosenvinge, W. R. Binns, P. L. Hink, and M. H. Israel. Measurement of the Secondary Radionuclides ^{10}Be,^{26}Al,^{36}Cl,^{54}Mn,$and^{14}C$ and Implications for the Galactic Cosmic-Ray Age. *ApJ*, 563:768–792, December 2001. doi: 10.1086/323842.

[13] A. Lukasiak. Voyager Measurements of the Charge and Isotopic Composition of Cosmic Ray Li, Be and B Nuclei and Implications for Their Production in the Galaxy. In *International Cosmic Ray Conference*, pages 41–+, 1999.

[14] J. J. Connell. Ulysses High Energy Telescope Measurements of the Isotopic Abundances of Galactic Cosmic Rays for Elements between C and Fe with Estimates of the Source Composition. In *International Cosmic Ray Conference*, pages 1751–+, 2001.

[15] F. Donato, D. Maurin, and R. Taillet. beta -radioactive cosmic rays in a diffusion model: Test for a local bubble? *A&A*, 381:539–559, January 2002. doi: 10.1051/0004-6361:20011447.

[16] I. V. Moskalenko, A. W. Strong, S. G. Mashnik, and J. F. Ormes. Challenging Cosmic-Ray Propagation with Antiprotons: Evidence for a "Fresh" Nuclei Component? *ApJ*, 586:1050–1066, April 2003. doi: 10.1086/367697.

[17] F. Paresce. On the distribution of interstellar matter around the sun. *AJ*, 89: 1022–1037, July 1984. doi: 10.1086/113598.

[18] D. M. Sfeir, R. Lallement, F. Crifo, and B. Y. Welsh. Mapping the contours of the Local bubble: preliminary results. *A&A*, 346:785–797, June 1999.

[19] S. Redfield and J. L. Linsky. The Structure of the Local Interstellar Medium. I. High-Resolution Observations of Fe II, Mg II, and Ca II toward Stars within 100 Parsecs. *ApJs*, 139:439–465, April 2002. doi: 10.1086/338650.

[20] H. Kimura, I. Mann, and E. K. Jessberger. Elemental Abundances and Mass Densities of Dust and Gas in the Local Interstellar Cloud. *ApJ*, 582:846–858, January 2003. doi: 10.1086/344691.

[21] H. Kimura, I. Mann, and E. K. Jessberger. Composition, Structure, and Size Distribution of Dust in the Local Interstellar Cloud. *ApJ*, 583:314–321, January 2003. doi: 10.1086/345102.

[22] Casadei D. *Direct measurement of galactic cosmic ray fluxes with the orbital detector AMS-02*. PhD thesis, Universitá degli Studi di Bologna, 2003.

[23] D. Maurin, R. Taillet, and F. Donato. New results on source and diffusion spectral features of Galactic cosmic rays: I B/C ratio. *A&A*, 394:1039–1056, November 2002. doi: 10.1051/0004-6361:20021176.

[24] R. Taillet and D. Maurin. Spatial origin of Galactic cosmic rays in diffusion models. I. Standard sources in the Galactic disk. *A&A*, 402:971–983, May 2003. doi: 10.1051/0004-6361:20030318.

[25] D. Casadei and V. Bindi. The Origin of Cosmic Ray Electrons and Positrons. *ApJ*, 612:262–267, September 2004. doi: 10.1086/422514.

[26] D. Müller. Cosmic-ray electrons and positrons. *Advances in Space Research*, 27:659–668, 2001.

[27] I. V. Moskalenko and A. W. Strong. Production and Propagation of Cosmic-Ray Positrons and Electrons. *ApJ*, 493:694–+, January 1998. doi: 10.1086/305152.

[28] Bonvicini *et al. Nucl. Instrum. Methods A*, 461:262, 2001.

[29] Boezio *et al. Nucl. Instrum. Methods A*, 471:184, 2001.

[30] Battiston R. *Frascati Physics Series*, 24:261.

[31] Sanuki T. *Int. J. Mod. Phys. A*, 17:1635, 2002.

[32] M. Sapinski. Cosmic-ray astrophysics with ams-02. In *29th International Cosmic Ray Conference*, page 2, 2005.

[33] AMS Collaboration Alcaraz J. *et al. Phys. Lett. B*, 484:10, 2000.

[34] AMS Collaboration Alcaraz J. *et al. Phys. Lett. B*, 490:27, 2000.

[35] AMS Collaboration Alcaraz J. *et al. Phys. Lett. B*, 472:215, 2000.

[36] AMS Collaboration Alcaraz J. *et al. Phys. Lett. B*, 494:193, 2000.

[37] AMS Collaboration Alcaraz J. *et al. Phys. Lett. B*, 461:387, 1999.

[38] AMS Collaboration Alcaraz J. *et al. Phys. Rep.*, 366:331, 2002.

[39] R. MacMahon. The Alpha Magnetic Spectrometer Superconducting Magnet. In *29th International Cosmic Ray Conference*, 2005.

[40] P. Zuccon. The AMS Tracker Performance. In *29th International Cosmic Ray Conference*, 2005.

[41] J. Olzem. Construction of the AMS-02 Transition Radiation Detector for the International Space Station. In *29th International Cosmic Ray Conference*, 2005.

[42] V. Bindi. Performance of the AMS-02 Time of Flight. In *29th International Cosmic Ray Conference*, 2005.

[43] Aguliar Benitez M. *et al.* The Ring Image Cherenkov detector (RICH) of the AMS experiment. In *29th International Cosmic Ray Conference*, 2005.

[44] J. Pochon. Astroparticle Physics with AMS-02. In *29th International Cosmic Ray Conference*, 2005.

[45] Ajima Y. *et al. Nucl. Instrum. Methods A*, 443:71, 2000.

[46] Gaisser T.K. *et al. Proc. 27th ICRC*, page 1643, 2001.

[47] Muller D. *et al. ApJ*, 374:356, 1991.

[48] Engelmann J.J. *et al. A&A*, 148:12, 1985.

[49] Maeno T. *et al. Ap. Phys.*, 16:121, 2001.

[50] M.Aguilar et al. (AMS Collaboration). Phys.Rep. 366, 2002.

[51] Tavani. *Int. J. Mod. Phys. A*, 17:1799, 2002.

[52] Battiston R. *et al. Astropart. Phys.*, 13:51, 2000.

[53] Bertucci B. *et al. Proc. 27th ICRC*, page 2777, 2001.

[54] Lamanna G. *et al. Nucl. Phys. B*, 113 Proc. Suppl.:177, 2002.

[55] Morselli A. *Int. J. Mod. Phys. A*, 17:1829, 2002.

[56] J. Ellis, R. A. Flores, K. Freese, S. Ritz, D. Seckel, and J. Silk. Cosmic ray constraints on the annihilations of relic particles in the galactic halo. *Physics Letters B*, 214:403–412, November 1988. doi: 10.1016/0370-2693(88)91385-8.

[57] M. S. Turner and F. Wilczek. Relic gravitational waves and extended inflation. *Physical Review Letters*, 65:3080–3083, December 1990.

[58] John R. Ellis. Particles and cosmology: Learning from cosmic rays. 1999.

[59] Steigmann G. *Ann. Rev. Astron. Astroph.*, 14:339, 1976.

[60] Peebles P.J.E. *Principles of Physical Cosmology*. 1993.

[61] AMS Collaboration. *Phys. Lett. B*, 461:339, 1999.

[62] W.R. Leo. *Techniques for Nuclear and Particle Physics Experiments*. 1987.

[63] Amati L. *et al.* Performances and space qualification tests of the ams time of flight. In *IEEE proceedings*, 2004.

[64] Casadei D. *et al.* The ams-02 time of flight system. *Nuclear Physics B (Proc. Suppl.)*, 113:133–138, 2002.

[65] Bindi V. *et al.* Performance of ams-02 time of flight. In *29th International Cosmic Ray Conference, Pune*, pages 101–106, 2005.

[66] G. Castellini F. Cindolo A. Contin G. Laurenti G. Levi A. Montanari F. Palmonari L. Patuelli C. Sbarra L. Brocco, D. Casadei and A. Zichichi. Behavior in strong magnetic field of the photomultipliers for the tof system of the ams-02 space experiment. *proceedings of the 27th ICRC*, 2001.

[67] Amati L. *et al.* The tof counters of the ams-02 experiment: space qualification tests and beam test results. In *Siena*, 2004.

[68] R. Martelli L. Quadrani C.Sbarra Giovacchini F., G. Levi. *Fine Mesh Thermovacuum Tests*. AMS-BO Internal Note, 2005.

[69] Baret B. *et al.* In-beam tests of the ams rich prototype with 20 a gev/c secondary ions. *Nucl. Instrum. Methods A*, 525:126–131, 2004.

[70] Casadei D. *et al.* S-crate physical connections. AMS Internal Note, 2005.

[71] Casadei D. *et al.* The ams-02 scintillator front-end electronics. AMS Internal Note, 2005.

[72] Gallin-Martel L. *et al.* The read out electronics of the ams prototype rich detector. AMS Internal Note, 2002.

[73] Gallin-Martel L. *et al.* A 16 channel analog integrated circuit for pmt pulses processing. AMS Internal Note, 2002.

[74] Gallin-Martel L. Eraud L. A test bench for the front end chip of the ams rich. AMS Internal Note, 2001.

[75] *AD7476/AD7477/AD7478 datasheet*. Analog Devices, 2004.

[76] *SX-A Family FPGAs datasheet*. Actel Corporation, 2001.

[77] Blasko S. Study of single event effects in electronic component. AMS Internal Note, 2001.

[78] Blasko S. Study of single event effects in electronic component. part ii. AMS Internal Note, 2002.

[79] Berges P. Study of single event effects in electronic component. part iii. AMS Internal Note, 2002.

[80] A. Kounine and V. Koutsenko. Ams-2 daq software organization, xdr and jinx nodes. AMS Internal Note, 2005.